Nano Research

Open Access

Review Article

2D material-engineered single-atom redox nanozymes: From rational design to biomedical and environmental applications

Yuyang Hao[1,§], Zedong Zhang[3,§], Runze Li[3,§], Qi Zhen[4,§], Zhiyi Sun[5], Chen Liang[1], Xiangqing Wang[1], Ruyu Zhao[1], Qidi Zhong[1] ✉, Yuexin Guo[1,3] ✉, and Liangdan Sun[2,6,7] ✉

[1] *School of Pharmacy, North China University of Science and Technology, Tangshan 063210, China*
[2] *North China University of Science and Technology, Tangshan 063000, China*
[3] *Department of Chemistry, Tsinghua University, Beijing 100084, China*
[4] *North China University of Science and Technology Affiliated Hospital, Tangshan 063000, China*
[5] *Energy & Catalysis Center, School of Materials Science and Engineering, Beijing Institute of Technology, Beijing 100081, China*
[6] *Department of Dermatology, the First Affiliated Hospital of Anhui Medical University, Hefei 230032, China*
[7] *Key Laboratory of Dermatology (Anhui Medical University), Ministry of Education, Hefei 230032, China*
§ *Yuyang Hao, Zedong Zhang, Runze Li, and Qi Zhen contributed equally to this work.*

Cite this article: *Nano Research*, **2026**, *19*, 94908816. https://doi.org/10.26599/NR.2026.94908816

ABSTRACT: Due to their unique physical and chemical properties, two-dimensional (2D) materials are ideal carriers for single-atom catalysts. Compared with traditional one- and three-dimensional support materials, these materials not only maximize active site exposure and improve atomic utilization efficiency, but also facilitate functional modification. Their excellent cellular uptake makes them highly suitable for biomedical applications. This article summarizes recent progress in the preparation of single-atom nanozymes (SAzyme) on 2D materials. It highlights these materials' unique advantages, innovative designs, and mimicking of natural enzymes' catalytic performance. It also details the materials' specific applications and practical effects in cancer treatment, antibacterial treatment, wound healing, drug delivery, biosensing, and wastewater treatment. The potential for future clinical translation and industrial application is discussed. This review provides a theoretical basis and technical pathways for the design and application of high-performance SAzyme, thereby promoting their practical applications in the fields of biomedicine and environmental remediation.



KEYWORDS: two-dimensional (2D) material, single-atom catalyst, single-atom nanozymes (SAzyme), oxidoreductase, biomedical applications

1 Introduction

Artist, chemist, and chef, what is the relationship among them? As shown in Fig. 2, the 2D materials prepared by the chemist have many similarities with the multi-layered cakes made by the chef. The hierarchical fabrication logic of 2D material-supported single-atom redox nanozymes (SAzymes) can be intuitively illustrated by the preparation of multi-layered cakes, which embodies the core principles of layered engineering, sequential assembly, interfacial bonding, and atomic-site anchoring in materials rational design. Analogous to the precise layer-by-layer stacking and timed component incorporation in cake-making, the synthesis of 2D material carriers follows strict structural regulation and sequential fabrication strategies. Specifically, the addition of raisins during the synchronous cake-baking process corresponds to the *in-situ* growth strategythe core interlayer bonding approach for 2D material-supported single-atom assembly, which realizes the synchronous construction of 2D layered supports and single-atom anchoring via bottom-up fabrication. In contrast, the post-synthesis decoration of

Received: March 17, 2026; **Revised:** April 14, 2026
Accepted: May 7, 2026

✉Address correspondence to Qidi Zhong, qidizhong@ncst.edu.cn; Yuexin Guo, yuexinguo@126.com; Liangdan Sun, liangds@ncst.edu.cn

cherries on the cake top is equivalent to the post-synthetic defect anchoring strategy, a typical defect bonding method that immobilizes single atoms on pre-fabricated 2D materials through top-down exfoliation and defect engineering. This analogy is not merely a morphological comparison, but a visual interpretation of the critical factors in SAzyme fabrication: the layered structure provides spatial confinement for single-atom dispersion, the sequential assembly mode determines the coordination environment of active sites, and the interfacial bonding effect strengthens the metal-support interaction (MSI). Just as a chef optimizes interlayer bonding and component distribution to guarantee cake quality, chemists regulate the layered structure, interlayer interaction, and atomic-site anchoring of 2D materials to maximize active-site exposure and redox catalytic activity of SAzymes, laying the structural foundation for their high-performance applications in biomedicine and environmental remediation.

SAzyme is a new generation of artificial mimetic enzymes developed based on the concept of single-atom catalysts. It disperses metal atoms in a single-atom form on the carrier material to form nanoscale enzymes with clear active sites and precise coordination environments [1]. There is no interaction between these atoms [2, 3]. The active site is generally composed of a single metal atom and other atoms adjacent to the surface of the support or the functional species [4]. In the first place, as the most basic functional material, the size of the single-atom greatly influences its catalytic performance. With the decrease of the single-atom size, the number of single atoms on the supporting surface increases, which enlarges the relative surface area, provides more active sites, and improves the catalytic efficiency [5]. On the contrary, the increase in size can lead to changes in the density of the electron cloud, which can affect the conductivity and catalytic activity of the material [6]. In addition, due to the influence of thermodynamic properties [7], smaller particles may exhibit different thermal stability, which is an important consideration for the design of efficient SAzymes [8]. Lastly, there is the influence of photophysical and photochemical properties [9] with the change of particle size. Smaller particles may exhibit more intense light absorption and higher photocatalytic activity [10].

In 2007, Gao et al. first reported that Fe nanoparticles had intrinsic peroxidase (POD)-like activity. This discovery initiated the research on enzyme-mimicking nanomaterials. Since then, dozens of enzyme-mimicking nanomaterials covering transition metals, precious metals, and carbon-based structures have been discovered [11]. In 2013, such systems were officially named "nanozymes". They integrate the stability and tunability of chemical catalysts with the substrate specificity of biological catalysts, and possess the unique properties of nanomaterials such as magnetism, light responsiveness, and thermal/electrical conductivity, laying the foundation for the integration of nanotechnology and biomedicine [12]. Traditional nanozymes have limitations such as low density and quality of active sites (i.e., catalysis is limited to the surface atomic layer, and catalytic efficiency is lower than that of natural enzymes), and difficulties in identifying active sites and poor substrate selectivity due to the heterogeneity of nanoscale structures [13, 14]. However, single-atom materials provide new ideas for solving these problems by maximizing atomic utilization and precisely regulating electronic configuration to enhance activity and selectivity, and have the unique properties of nanomaterials such as magnetism, light responsiveness, and thermal/electrical conductivity. This has driven a transformation in catalytic science [15]. SAzyme effectively overcomes the limitations of traditional nanozymes through nearly 100% metal atomic utilization, stable atomic sites, and the ability to regulate their electronic configuration to enhance activity and selectivity through strong metal-bridge interactions, as well as clear active centers [16, 17]. SAzyme combines the single-atom catalytic mechanism with nanotechnology engineering, achieving enzyme function biomimicry by stably loading isolated metal atoms on inorganic carriers such as metal-organic frameworks (MOFs), carbon materials, and metal oxides [18]. Its typical synthesis techniques include atomic layer deposition, high-temperature pyrolysis, and wet coordination self-assembly. These techniques can precisely control the spatial distribution and electronic structure of active sites at the nanoscale, thereby improving reaction selectivity and atomic utilization [19]. Unlike simulated enzymes, the catalytic performance of SAzyme is more dependent on the carrier structure and interface electronic effects, possessing a wider range of functions and physical stability, and is suitable for complex physiological environments [20]. Although the technical barriers in the preparation process are high, with the progress of scalable nanofabrication processes in recent years, SAzyme has demonstrated the potential for cost-effective large-scale synthesis, laying the foundation for the promotion of its practical application [20].

With the continuous development of the medical-related fields, the requirements for the catalytic performance of biological enzymes have further developed [21]. However, the catalytic performance of current catalysts is limited and cannot meet the demands of various fields. Therefore, many studies on nanozymes loaded with single-atom on 2D materials have been emerging one after another [22]. The reason for using 2D materials to load single atoms is that, since their discovery, these 2D materials have brought researchers unexpected excellent characteristics. Since the mechanical exfoliation of graphene in 2004, 2D materials have received increasing attention in research (Fig. 1). 2D materials have many advantages. First and foremost, the thickness of 2D materials is controllable, and there are many methods to prepare 2D materials [23–26]. Through these different preparation methods, the thickness can be precisely controlled, usually ranging from a few nanometers to several tens of nanometers [27]. The extremely thin thickness and large lateral dimensions of two-dimensional materials enable them to exhibit various interesting properties. For instance, they have a high specific surface area [28], tunable optical properties [29], excellent mechanical properties and thermal conductivity [30], etc. These properties make 2D materials have wide applications. Apart from this, 2D materials have special electronic structures, including adjustable band gaps, unique Fermi surfaces, and band structures [31]. These unique characteristics prompt us to study other 2D materials [32]. Nowadays, the family of 2D materials covers many categories, including but not limited to graphene and its derivatives, transition metal dichalcogenide compounds (TMDs) [33], metals, metal oxides [34], metal hydroxides [35], metal nitrates [36], and MOF [37–41]. 2D materials are regarded as one of the most important materials in the fields of physics, chemistry, materials science, and electronics. It is not difficult to observe that both single-atom catalysts and 2D materials have their own unique "glowing points" in terms of their respective characteristics. They are like two "puzzle pieces" with different advantages. When we attempt to combine the two, that is, to load the single-atom catalysts onto the 2D materials, we can expect that the advantages of the two will interact and complement each other. This will lead

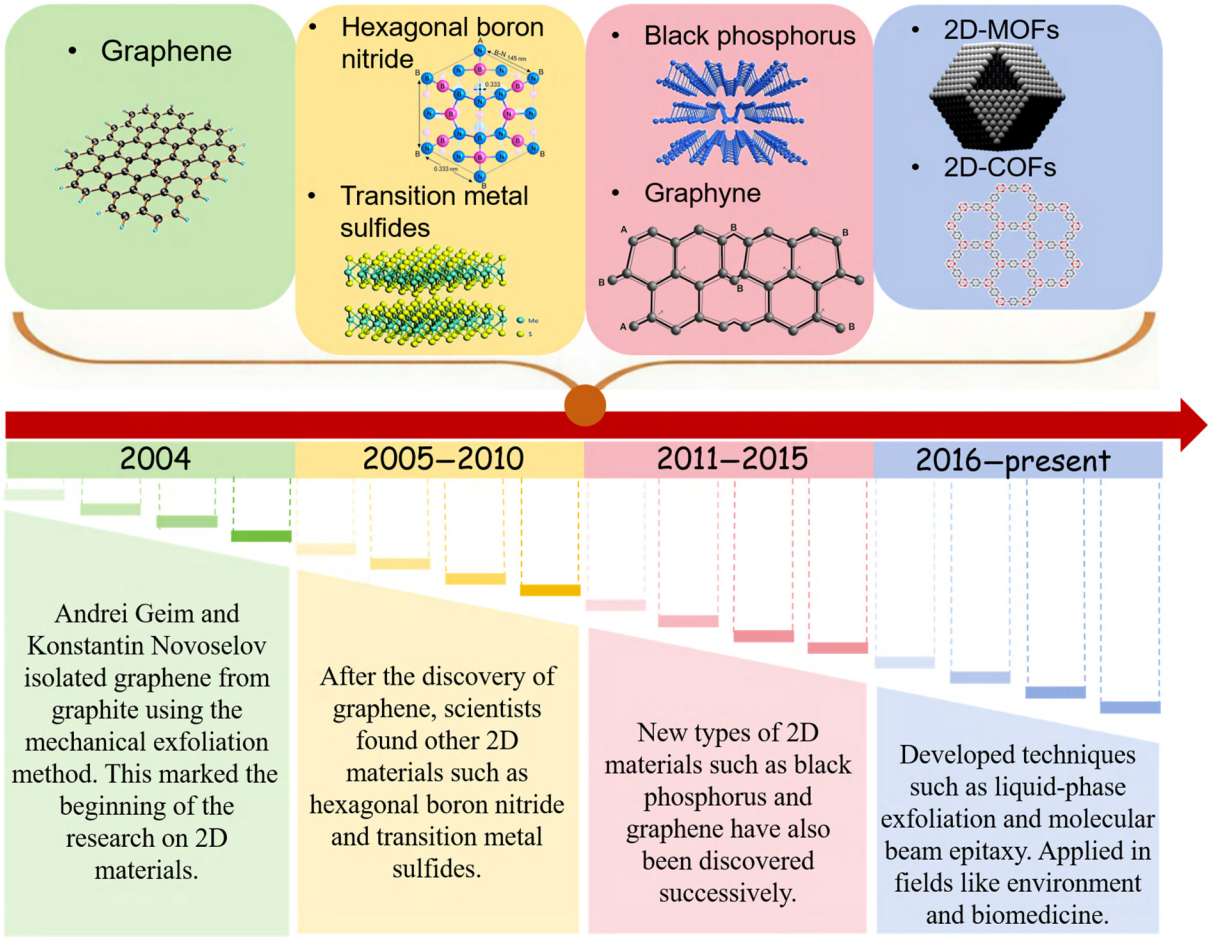


Figure 1 The development history of 2D materials [44–46].

to more outstanding redox activity and open up new prospects with greater potential for catalytic applications [42, 43].

There are five ways for 2D materials to combine with single atoms (Fig. 2). Catalysts that are loaded with single-atom and possess enzyme activity can be referred to as SAzyme.

Redox nanozyme refers to a type of nano-material that possesses catalytic activity similar to that of redox nanozymes. It can simulate the functions of natural redox nanozyme at the nanoscale and catalyze the conversion of substrates through oxidation or reduction reactions. In 2019, researchers reviewed the characteristics and advantages of 2D materials combined with single atoms, and then summarized the methods for preparing SACs@2D and analyzed the advantages and disadvantages of various strategies [50]. In 2021, the glucose oxidase-like activity of Au NPs was studied [51]. Through the dehydrogenation mechanism, electrons were directly transferred to O_2 to generate H_2O_2, without the need for reactive oxygen species (ROS) intermediates, which was consistent with the natural enzyme pathway [52]. Moreover, precious metals such as Pt and Pd can catalyze the reduction of coenzymes (flavin adenine dinucleotide (FAD), cytochrome *c* (Cyt *c*)), expanding to the detection of nitro compounds and proposing the new concept of "coenzyme simulation". In addition, Fe-N-C type redox nanozymes were synthesized [53]. By introducing a second nitrogen precursor (cyanamide), they increased the enzyme activity by 55%. At a neutral pH value, its K_m = 0.012 mM, which was close to the value of the natural enzyme. In 2025, it was discovered that the redox activity of amorphous CoO_x was significantly higher than that of peroxidase [54]. Under acidic conditions, H_2O_2 would cause CoO_x to decompose into inactive Co^{2+}, thereby inhibiting the pathway of peroxidase. The high surface defects of the amorphous structure promote the activation of O_2 to generate superoxide radicals ($\cdot O_2^-$). The team developed a "closed-type" glucose detection system. It utilizes the degradation effect of hydrogen peroxide on cobalt oxide. The detection limit is as low as 0.09 μM, and it has strong anti-interference capabilities. Li et al. synthesized B-doped Zn single-atom enzymes [55]. The Zn-N-B bonds cause the *d*-band center to shift upward, thereby enhancing the O_2 adsorption. Its oxidoreductase reached 9.26 U/mg. Combined with the clustered regularly interspaced short palindromic repeats (CRISPR)/Cas13a system, the signal was amplified through the terminal deoxynucleotidyl transferase (TdT) amplification reaction. RNA detection at a level of 20 aM was achieved, and the differentiation status of cancer cells was successfully distinguished. This significantly expands the application scope of nanozymes and holds great potential for future development. Recently, Ni_1-CdS/WO_3 redox heterojunction was reported for efficient photocatalytic urea synthesis from N_2 and CO_2, with single-atom Ni and 2D heterostructure improving carrier separation and utilization to achieve a high urea yield rate [56].

However, there are still many bottlenecks. In the first instance, there is a lack of stability [6]. Metal atoms tend to aggregate in high-temperature or reducing environments, and the interaction between metal and carrier needs to be strengthened [2, 57]. Next, it

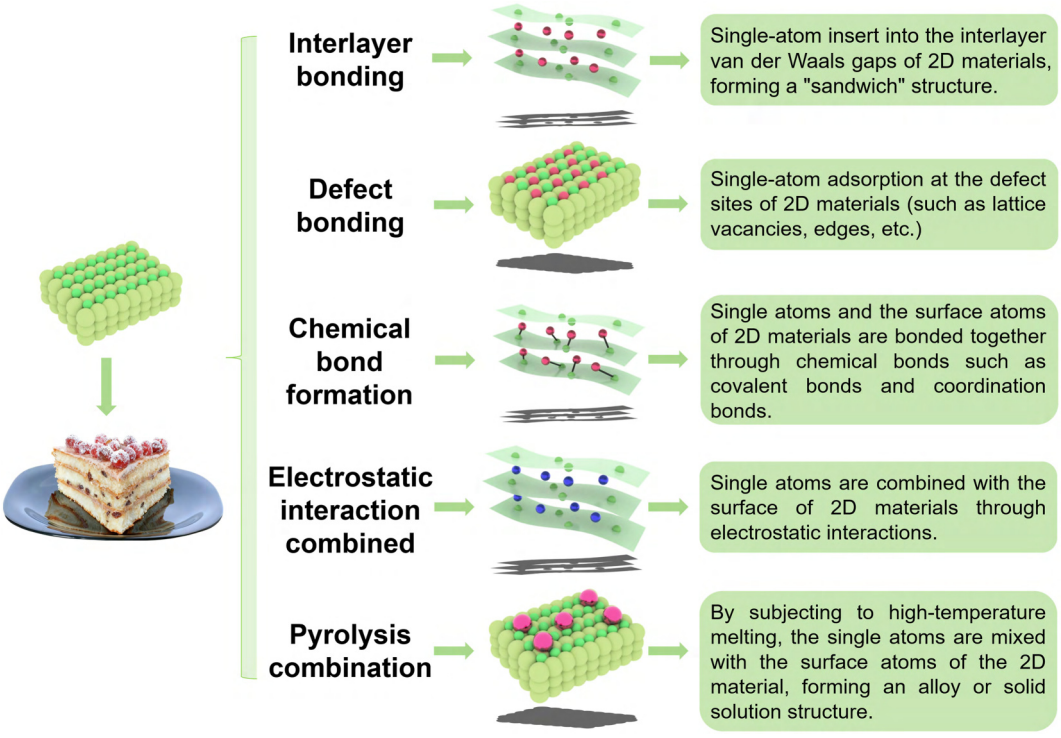


Figure 2 The combination methods of 2D materials with single-atom [47–49].

cannot be produced on a large scale [8]. At present, the controlled preparation of solid acid catalysts with high loadings (over 2 wt%) still relies on complex processes. The industrial production process has high energy consumption. The yield of the gas migration strategy is less than 50% [58]. There are also limitations in the mechanism understanding [59]. The coordination evolution of active sites during dynamic reactions lacks *in situ* characterization methods [60]. The multi-atom cooperative mechanism has not been universalized [60–62]. At last, the application scenarios are limited [63]. This enzyme-like catalytic system has relatively poor anti-interference ability for complex biological samples (such as serum) [64].

Based on the above analysis, it is necessary to summarize the applications of SAzyme in the redox activity (Fig. 3). Therefore, this article first reviews the types and preparation methods of 2D materials, and then introduces the application of SAzyme in the activities of oxidase (OXD), peroxidase (POD), catalase (CAT), superoxide dismutase (SOD), and glutathione peroxidase (GPx). Then, it summarizes the common applications of SAzyme in the biomedical field, including cancer treatment, antibacterial and wound healing, drug loading and delivery, and biosensing. Eventually, its application in wastewater treatment is also introduced. This review is expected to provide more insights into the controllable preparation of SAzyme with redox activity, the optimization of catalytic mechanisms, and the practical application strategies in the biomedical and wastewater treatment fields.

The mechanistic synergy between 2D materials and single atoms endows SAzymes with superior redox catalytic activity, which is fulfilled by the coupled effects of three distinctive physicochemical properties of 2D materials. First is the high surface-to-volume ratio, which exerts a spatial confinement effect to maximize the dispersion of isolated single-atom sites, eliminate metal aggregation, amplify active-site exposure density, elevate atomic utilization efficiency to nearly 100%, and accelerate substrate/product mass transfer. Second is the tunable electronic structure, which modulates the *d*-band center of single-atom metal centers via strengthened MSI, optimizes the adsorption--desorption energy of reaction intermediates (O_2, H_2O_2, $\cdot O_2^-$), accelerates interfacial electron transfer, and reshapes redox reaction pathways to boost the catalytic kinetics of OXD, POD, CAT, SOD, and GPx. Third is the abundant surface coordination sites, which provide a stable anchoring microenvironment for single atoms through M-N_x/M-O_x/M-S_x coordination engineering, lock the atomic-level active centers, tailor the local electronic state and coordination number of metal sites, and enhance the structural stability of SAzymes in complex physiological and environmental media. This tripartite synergy directly determines the ROS generation/scavenging efficiency, substrate selectivity, and catalytic robustness of SAzymes, which constitutes the fundamental mechanistic basis for their high efficacy in biomedicine and wastewater decontamination [65].

2 Classification and preparation of 2D materials with redox activity

2D materials with redox activity can be classified based on their structural and functional properties. This material has many excellent properties, and its preparation process is the key to whether it can effectively load single-atom and achieve better redox activity. Therefore, it is necessary to explore its preparation methods. In general, the preparation method can be divided into two steps: top-down and bottom-up. The top-down peeling methods include liquid phase stripping [66, 67], ion intercalation/stripping [68, 69], and physical stripping [70]. The bottom-up methods include chemical vapor deposition, physical vapor deposition, hydrothermal, and atomic layer deposition.

2.1 Classification of 2D materials with redox activity

Benefiting from their inherent layered nanostructures, large specific

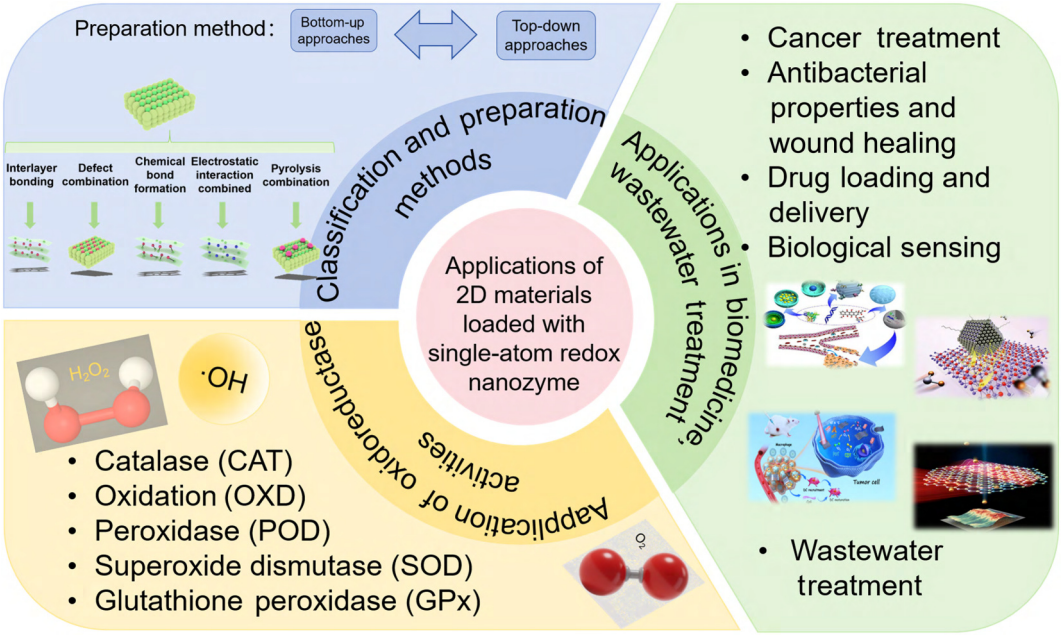


Figure 3 Applications of 2D materials loaded with single-atom redox nanozyme.

surface areas, tunable electronic structures, and abundant anchoring sites, two-dimensional (2D) materials are ideal supports for constructing high-performance single-atom redox nanozymes. 2D materials have shown great potential in catalysis, energy conversion, and other fields [71]. These 2D matrices can stabilize isolated metal atoms, modulate the electronic configuration of active sites, and boost redox catalytic kinetics at the atomic level. According to material composition and structural characteristics, 2D redox-active supports for single-atom loading are classified into the following categories:

The first category is two-dimensional metal-organic frameworks (2D MOFs). 2D MOFs feature ultrathin thickness, ultrahigh specific surface area, uniform pore structures, and designable coordination environments. Their abundant unsaturated metal sites and functional ligands endow them with intrinsic redox activity, providing abundant defect sites for anchoring single-atom metal centers and maximizing atomic utilization efficiency [72]. According to the differences in enzyme activity, MOF nanozymes mainly include OXD, POD, CAT, SOD, and GPx, etc. [73, 74]. In tumor treatment, based on MOF-based magnetic nanozymes (PZFH), Chen et al. demonstrated multi-enzyme cascade activity under light and magnetic effects, which could induce enhanced tumor ferroptosis effects, opening up new avenues for tumor treatment [75].

The second category is 2D carbon-based materials. This category includes graphene, graphene oxide (GO), graphdiyne, graphitic carbon nitride (g-C_3N_4), and doped carbon nanosheets [76]. Owing to their excellent electrical conductivity, chemical stability, and tunable surface functional groups, 2D carbon-based materials can regulate the *d*-band center of single-atom sites via heteroatom doping (e.g., N, S, P, B), thereby significantly enhancing the catalytic performance of oxidoreductase-like nanozymes [77]. Zhang et al. discovered that GO nanosheets can efficiently catalyze the formation of oxidized 3,3',5,5'-tetramethylbenzidine (TMB), thereby triggering color changes [78]. In the field of biosensing, this property can be utilized for visual detection of specific substances. The research on new carbon-based nanocomposites mainly focuses on integrating the structural characteristics of fullerenes, carbon nanotubes, and graphene oxide [79]. By non-covalent modification and *in-situ* composite techniques, materials with anti-wear and friction-reducing properties are prepared. This has expanded the application of carbon-based nanomaterials in the field of tribology.

The third category is 2D transition metal chalcogenides/oxides/nitrides. Represented by MoS_2, WS_2, MnO_2, Fe_3O_4, and CoO_x, these 2D materials possess tunable band structures and abundant surface defects. Their intrinsic redox activity and strong MSI facilitate the dispersion and electronic modulation of single-atom catalysts. Taking Fe_3O_4 nanoparticles as an example [80], they can catalyze TMB, DAB, and o-phenylenediamine (OPD), making them present blue, brown, and orange colors, respectively [81]. In the field of environmental governance, transition metal oxide nanoparticles can be applied in catalytic degradation of organic pollutants, showing fascinating application potential. The fifth category is single-atom nanomaterials [80, 82, 83]. For example, Fe-N/C nanozyme, with its unique electronic structure and chemical composition, plays a key role in catalytic reactions [84]. The $RuNi_{SAA}$-$Ti_3C_2T_x$ catalysts studied by Guan et al. also exhibit excellent performance [85].

There are also two-dimensional MXenes and two-dimensional covalent organic frameworks (2D covalent organic frameworks (COFs)), etc. As an emerging star among 2D layered materials, MXenes possess high metallic conductivity, abundant surface terminations (–O, –OH, –F), and excellent structural stability [86]. They provide confined spaces for single-atom loading and accelerate electron transfer in redox reactions. 2D COFs exhibit periodic porous structures, precise functional group decoration, and high crystallinity [87]. Their conjugated backbones and tunable coordination sites enable the stable anchoring of single atoms and the precise regulation of redox catalytic pathways.

The extremely high specific surface area of 2D materials provides abundant attachment sites for individual atoms. This enables them to be uniformly dispersed and avoid aggregation. Thus, it maximizes the utilization rate of atoms. Its unique electronic structure and tunable physical and chemical properties can be

optimized to become catalytically active sites by adjusting the coordination environment of individual atoms. This thereby enhances catalytic efficiency. As a single atom is the smallest catalytically active unit, it has a clear active center and can precisely control the catalytic reaction pathway. When combined with 2D materials, the two work together to form SAzyme with excellent catalytic performance, good stability, and diverse functions. They have demonstrated potential for applications beyond traditional materials in fields such as biomedicine and wastewater treatment. With further research and development, they are expected to become efficient, stable, and low-cost catalysts to replace natural enzymes.

2.2 Methods for the preparation of 2D materials with redox activity

The structural properties of 2D supports (thickness, defects, heteroatom doping, interlayer spacing) are tailored to stabilize single-atom dispersion and optimize metal-support interaction. Top-down and bottom-up strategies are employed to fabricate well-structured 2D supports, which serve as the foundational platform for subsequent single-atom loading. The rational integration of 2D support preparation and single-atom anchoring directly determines the formation of catalytically active single-atom redox nanozymes (SAzyme). Therefore, the correlation among 2D support preparation, single-atom loading, and catalytic performance of single-atom nanozymes is critical for constructing high-performance single-atom redox nanozymes.

2.2.1 Top-down approach

The top-down approach is a fabrication strategy that involves layer-by-layer removal of materials by physical or chemical methods to obtain 2D materials. This method is widely used for the synthesis of ultrathin 2D materials. For example, in 2018, Pei et al. synthesized graphene oxide films using electrochemical (EC) (Fig. 4(a)) [88]. At room temperature, graphene oxide was synthesized from commercial flexible graphite paper (FGP). Commercial flexible graphite paper has a similar structure to graphite with high tensile strength (4–5 MPa), excellent conductivity, and flexibility. Its thickness is usually from microns to millimeters, width up to meters, and length up to kilometers [88]. The top-down method is commonly used for some thin sheet materials in the presence of weak van der Waals forces, such as in 2021, Liu et al. first obtained monolayer 2D Zn-MOF nanosheets by a simple top-down strategy based on 3D layered Zn-MOF crystals [89]. It involves two steps: step one, the van der Waals interaction between layers is weakened by protonation of Zn-MOF under acidic conditions; step two, the weakened van der Waals interactions are further disrupted by electrostatic interactions using negatively charged band molecules, such as Congo red (CR) or methyl orange (MO) [89]. On account of the weak van der Waals force interaction between the layers, it is easy to peel the 3D structure of the material into a 2D structure.

Supercritical carbon dioxide (SC-CO_2) technology has shown its unique advantages in the preparation of 2D materials. Xu et al. have been dedicated to using the green solvent regulation technology of supercritical CO_2 to prepare functional nanomaterials suitable for energy conversion and storage [90]. They innovatively proposed using CO_2 to encapsulate the hydrogen bond of THF-HOAc. In the supercritical CO_2 system, they achieved the reconfiguration of the secondary structure units of metal-organic framework materials (Cu-BTC, BTC: 1,3,5-phenyltricarboxylic acid). Cu-BTC forms face-centered cubic crystals containing an intersecting 3D framework of three distinct guest-accessible pores, which are linked together along the body diagonal direction. Its pore structure is composed of main channels. The cross-section of the main channel is a square, with a diameter of approximately 9.0 Å. There is also a tetrahedral-shaped side pocket with a diameter of approximately 5.0 Å. This side pocket is connected to the main channel through a triangular window with a diameter of approximately 3.5 Å (Structure I). The secondary structure unit (SSU) of 3D Cu-BTC is a propeller-like copper (II) dimer structure (PW unit). In this structure, each Cu

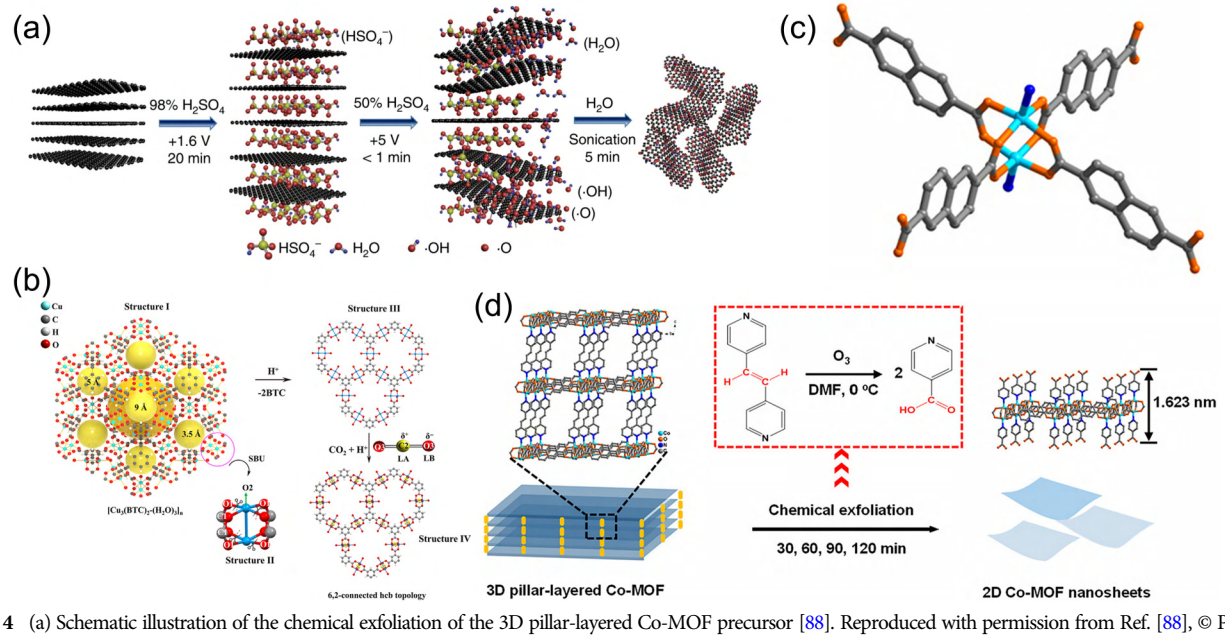


Figure 4 (a) Schematic illustration of the chemical exfoliation of the 3D pillar-layered Co-MOF precursor [88]. Reproduced with permission from Ref. [88], © Pei, S. et al. 2018. (b) Schematic illustration of the chemical exfoliation of the 3D pillar-layered Co-MOF precursor [90]. Reproduced with permission from Ref. [90], © Zhou, Y. et al. 2018. (c) Coordinated structure of the Co-MOF with H_2NDC as layer ligands [92]. (d) Schematic illustration of the chemical exfoliation of the 3D pillar-layered Co-MOF precursor [92]. Reproduced with permission from Ref. [92], © Institute of Process Engineering of CAS 2024.

atom is coordinated by four O atoms and one Cu atom in an octahedral manner (Structure II) [91]. The remaining free coordination sites are occupied by one water molecule, indicating a possible Lewis acid active site. It is characterized by the dissociation of the localized BTC ligand on the Cu(II) dimer and the subsequent coordination of the capping CO_2 by controlling the conditions of the supercritical CO_2. A series of experiments and theoretical results indicate that owing to the unique solvation effect of SC CO_2, it not only helps to transport molecules, but also can achieve the reconfiguration of solvent molecule clusters within the pore-restricted space of copper-Bertin-benzothiophene (Cu-BTC) pores. That is, the selective dissociation of the BTC ligand and the subsequent closed coordination of CO_2. Finally, a transformation from a three-dimensional structure to a 2D structure is completed (Fig. 4(b)).

Zhen et al. developed a strategy to selectively break the covalent bonds of columnar ligands in 3D lamellar MOF using ozone oxidation to fabricate 2D MOF monolayer nanosheets "top-down" [92]. By adjusting the oxidation time, the thickness of the nanosheets can be controlled, and the surface of the nanosheets has a functionalized -COOH group (Fig. 4(c)). This method provides an efficient and versatile approach for the preparation of a monolayer MOF from a 3D layer-columnar MOF. In the first instance, a MOF precursor material with a 3D columnar layer structure was synthesized. Afterwards, the vinyl group in the columnar ligand 1,2-bis(4-pyridyl)ethylene was selectively cleaved through an ozone oxidation reaction. Combined with temperature control, ultrasonic assistance, and reaction time optimization, 2D MOF nanosheets were finally prepared (Fig. 4(d)). To prepare 2D cobalt metal-organic framework nanosheets, a 48-h hydrothermal reaction was conducted in deionized water at 180 °C using cobalt metal salt, pillar ligand, and layer ligand. The resulting cobalt metal-organic framework with a 3D pillar-layered structure was used as the precursor. This conclusion was drawn based on previous research reports [93]. In its structure, the 2D bilayer is constructed by the connections of the layer ligand 2,6-naphthalenedicarboxylic acid (H_2NDC) and Co(II) ions. Further layer-by-layer assembly linked by the pillar ligand *trans*-1,2-bis(4-pyridyl)ethylene (bipyen) results in the final 3D pillar-layered Co-MOF framework.

Zhang et al. developed a green and efficient preparation method, using ultrasonic-assisted liquid-phase exfoliation and sustainable alcohol-based solvents to prepare MoS_2 nanosheets. Comprehensive characterization results confirmed that the ethanol-mediated exfoliation process could generate complete 2H phase nanosheets [94]. Jawaid et al. carried out the process of peeling the granular microcrystals of V-VII group layered TMD by using mild redox chemical reactions in a static desktop experimental environment. During this process, the anionic polyoxometalate substances generated at the edge positions would adsorb onto the surface of TMD, thereby generating a Coulomb repulsive force. This repulsive force could cause the interlayer separation without the need for a shear force [95].

These top-down exfoliation strategies tailor 2D supports with abundant defects and anchoring sites, laying the foundation for single-atom loading and redox nanozyme activity endowment, while the constructed 2D material-supported single-atom systems also exhibit targeted applicability in biomedical and environmental remediation fields. For biomedical applications, Li et al. converted sulfur-poisoned Pd_xS_y nanoparticles into single-atom Pd on 2D N-doped carbon supports via thermal atomization; this single-ample Pd catalyst exhibited intrinsic peroxidase-like redox activity, enabling efficient colorimetric biosensing of hydrogen peroxide (H_2O_2) in biological samples and showing potential for early disease diagnosis [96]. For wastewater treatment, Wu et al. developed a thermal printing strategy to disassemble Fe_3O_4 nanoparticles into single-atom Fe at 2D SiO_2/carbon heterojunctions, endowing the catalyst with excellent oxidoreductase-like activity for CO_2 reduction and organic pollutant degradation. This system can effectively remove refractory carbon pollutants in industrial wastewater and realize carbon resource recycling [97]. Additionally, Luo et al. adopted cathodic corrosion to disintegrate Pt/Pd nanoparticles into single atoms anchored on 2D N-doped carbon supports, which displayed remarkable oxygen reduction reaction (ORR) activity; this single-atom system can be applied to degrade oxygen-containing organic pollutants in water and purify heavy metal-ion-contaminated wastewater [98, 99]. Tilley et al. transformed Pt islands into isolated single-atom Pt on 2D Ru nanosheets via thermal treatment, showing outstanding oxidoreductase-like activity for the methanol oxidation reaction (MOR); this system is particularly suitable for treating methanol-containing industrial wastewater and mitigating water eutrophication caused by methanol pollution [100].

2.2.2 *Bottom-up approach*

The bottom-up approach is also a commonly used method for preparing 2D materials. It mainly relies on specific chemical reactions. Starting from the microscopic molecules, atoms, or ions, they are combined through chemical bonding methods to form larger cluster structures. Then, these structures are further assembled to synthesize nanoscale structures based on these cluster structures.

Wang et al. employed a bottom-up surfactant-assisted method [43]. By coordinating the pre-synthesized Zn monomers with the porphyrin precursor (Zn-TCPP) and the $Cu_2(COO)_4$ metal nodes, they successfully assembled ultrathin 2D metal-organic framework nanozymes (SZN-MOFs) (Fig. 5(a)). This method fully utilizes the high specific surface area (372 m^2/g) and tunable pore structure of 2D metal-organic framework materials. It achieves a high-density loading of Zn monomers (4.6 wt%). Moreover, it constructs an active center with a clear Zn-N_4 coordination structure, similar to that of a peroxidase. SZN-MOFs, with their atomically dispersed zinc sites and ultrathin thickness of only 2.5 nm, significantly reduce the substrate diffusion resistance. Their POD-like activity (specific activity 6.34 U/mg) is superior to traditional porphyrin ligands and bulk MOF materials [101]. Experiments and density functional theory (DFT) calculations have confirmed that this material can effectively catalyze the conversion of H_2O_2 to ·OH [102]. The mechanism is achieved by oxidizing and destroying the extracellular polymeric substances (EPS) in the biological membranes and bacterial cell membranes (Fig. 5(b)). At a lower H_2O_2 concentration (100 μM), it can cause the survival rate of bacterial cell membranes to be less than 10% *in vitro*. Moreover, it significantly promotes the healing of wound infections *in vivo*. This provides a new strategy for designing nanozymes with redox activity based on 2D materials.

Zhang et al. synthesized 2D graphene dyne (SGDY) nanosheets doped with sulfur through a bottom-up one-pot hydrothermal method (Fig. 5(d)) [103]. These materials possess both piezoelectric properties and POD-like activity. The incorporation of sulfur introduces defects and disrupts the central symmetry of the

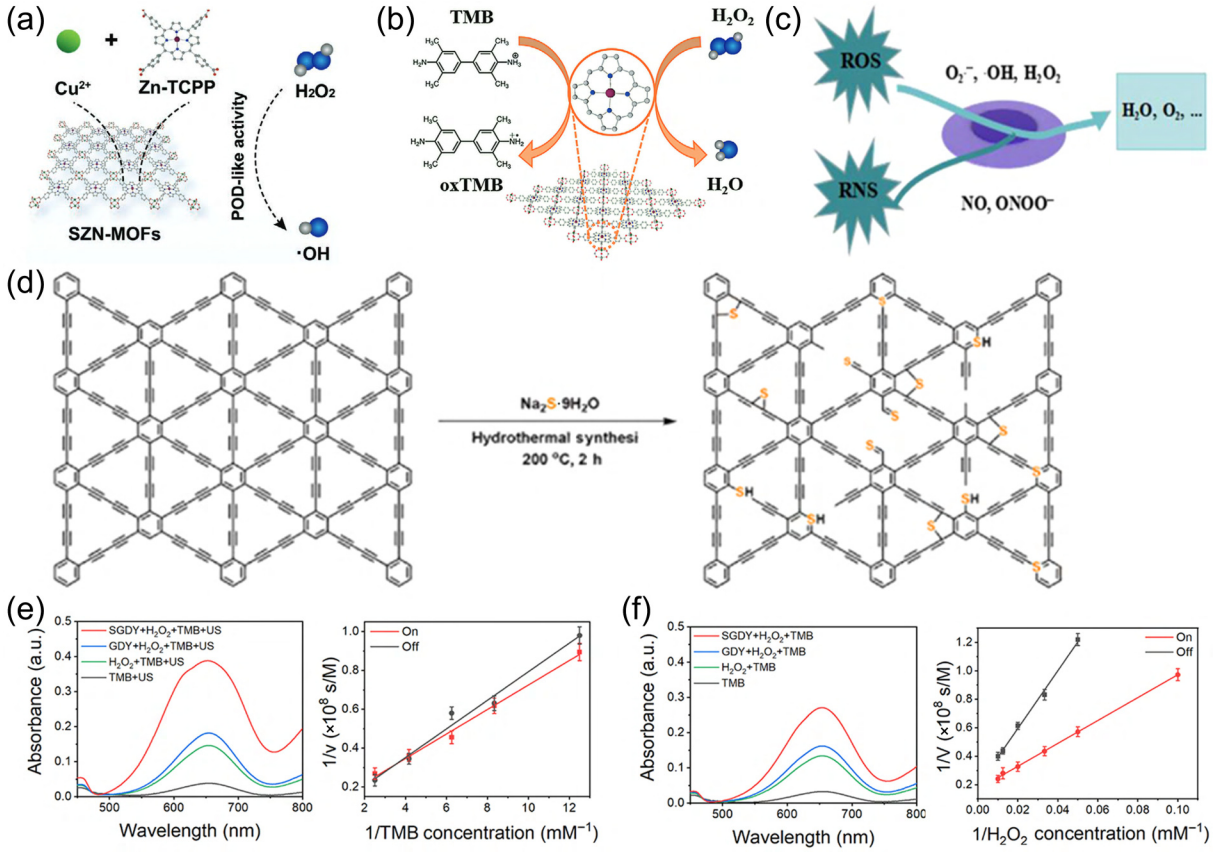


Figure 5 (a) Synthesized SZN-MOFs with POD-like activity can catalyze the generation of ·OH from H_2O_2 [43]. (b) Schematic diagram of the catalytic mechanism of the POD-like activity of SZN-MOF [43]. Reproduced with permission from Ref. [43], © Wiley-VCH GmbH 2022. (c) Schematic illustration of Bi_2Se_3 nanodiscs for IBD therapy by scavenging RONS [104]. Reproduced with permission from Ref. [104], © Acta Materialia Inc. Published by Elsevier Ltd. All rights reserved 2023. (d) The synthetic route of SGDY [103]. (e) Comparison of different conditions with and without ultrasound [103]. (f) Comparison of the kinetic rate constant of H_2O_2 and TMB with and without ultrasound [103]. Reproduced with permission from Ref. [103], © Elsevier Ltd. All rights reserved 2022.

graphene chains. This not only reduces the band gap (from 1.37 to 1.22 eV), increases the density of active sites, but also endows the material with piezoelectric response capabilities. Under ultrasonic irradiation, the built-in electric field generated by the piezoelectric effect causes the separation of charges. This accelerates the decomposition of H_2O_2, thereby generating reactive oxygen species (such as ·OH and $\cdot O_2^-$). As a result, the catalytic performance similar to that of enzymes is significantly enhanced (Figs. 5(e) and 5(f)). The experiments have shown that SGYD exhibits excellent performance in dye degradation (with a degradation rate of 98.1% for rhodamine B), antibiotic degradation, and bacterial disinfection (with clearance rates of > 99.99% for both Gram-positive and Gram-negative bacteria). Moreover, its practical application potential has been verified through a laboratory-scale continuous wastewater treatment device. DFT calculations indicate that the sulfur-doped sites act as the catalytically active centers. They reduce the energy barrier of the reaction. Moreover, the piezoelectric effect further enhances the efficiency of charge transfer.

Wu et al. proposed a wet chemical method based on soft templates [105]. By adjusting the dosage of the template agent MES, they were able to synthesize 2D MnO_2 nanosheets with dual enzymatic activities of OXD and POD in a controllable manner (Fig. 6(a)). The study found that when the MES concentration was 0.1 M, ultra-thin 2D materials with a lateral size of approximately 300 nm and a thickness of approximately 5 nm could be prepared (Figs. 6(b) and 6(c)). Their surface was negatively charged (ζ potential −30.30 mV), and they had excellent dispersibility. The dual enzyme activity test indicated that the 2D MnO_2 nanosheets could efficiently catalyze the oxidation of substrates such as TMB, OPD, and 2,2'-azino-bis(3-ethylbenzothiazoline-6-sulfonic acid) (ABTS) in the presence of O_2 or H_2O_2 (Fig. 6(d)). Their OXD ability originated from the ultrathin structure, high surface area, and strong electron transfer ability. Based on its specific adsorption property for single-stranded DNA (ssDNA), which binds to the surface of the nanosheets through hydrogen bonds and π-π stacking, thereby masking the active sites and inhibiting the catalytic activity. A labeled homogeneous electrochemical sensor for microRNA detection was constructed. Using let-7a as the model analyte. When the target molecule hybridizes with the probe strand to form double-stranded DNA (dsDNA), this dsDNA will detach from the surface of the nanosheet and regain its catalytic activity. The methylene blue (MB) is oxidized. The current change of MB is monitored by differential pulse voltammetry (DPV) to achieve detection. This sensor had a linear detection range of 0.4–140 nM for let-7a, a detection limit as low as 0.25 nM, and exhibited merit selectivity and biocompatibility.

Wu et al. employed a bottom-up method to prepare 2D copper-anchored carbon nitride (Cu-g-C_3N_4) nanosheets [106]. This material possesses both glucose oxidase and peroxidase activities and can generate ROS through a cascade reaction to kill bacteria. The specific process is as follows: in the initial step, carbon nitride (g-C_3N_4) nanosheets are prepared through thermal polymerization

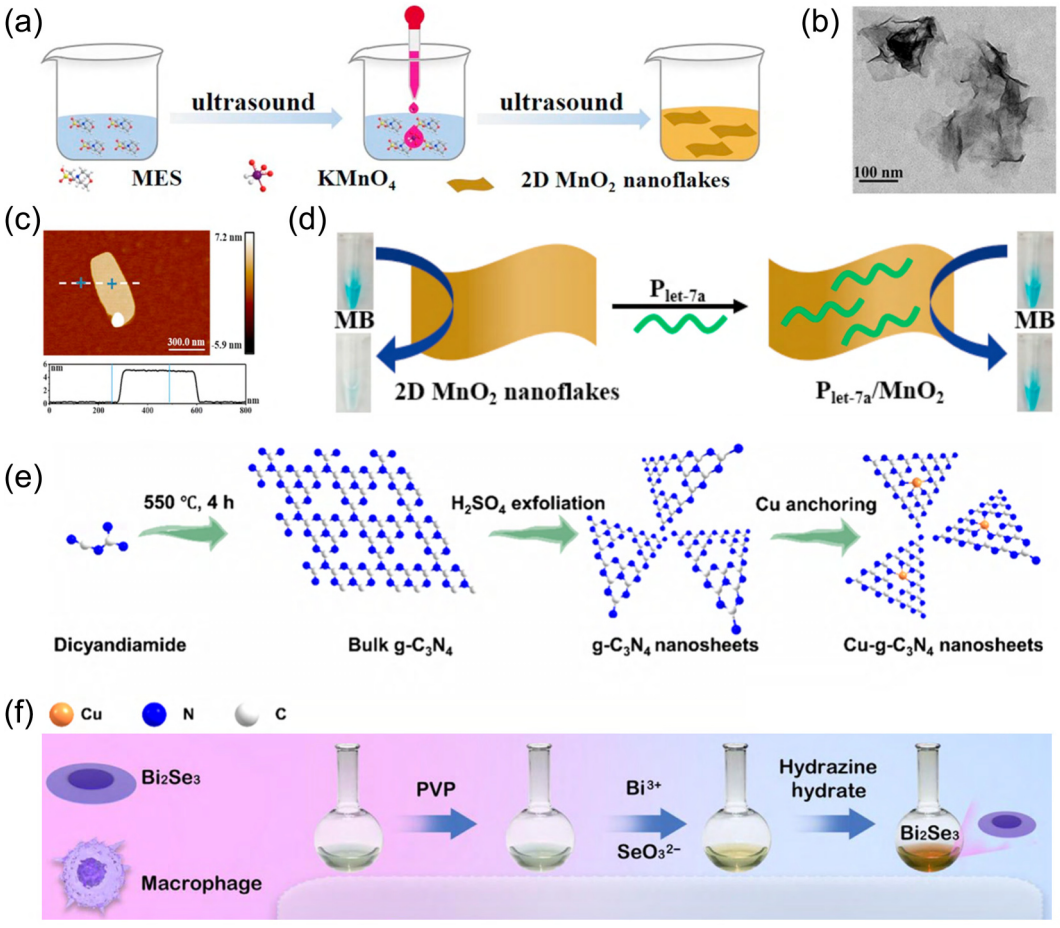


Figure 6 (a) Scheme illustration of the fabrication of 2D MnO_2 nanoflakes [105]. (b) TEM images of the MnO_2 nanomaterials by using 0.1 dosages of MES [105]. (c) AFM image of 2D MnO_2 nanoflakes [105]. (d) Effect of Plet-7a on the catalytic activity of 2D MnO_2 nanoflakes toward MB [105]. Reproduced with permission from Ref. [105], © Elsevier B.V. All rights reserved 2020. (e) Synthesis of single-atom Cu-g-C_3N_4/PCL Nanofibers [106]. Reproduced with permission from Ref. [106], © Wu, F. et al. Published by American Chemical Society 2025. (f) A Schematic illustration of the preparation of Bi_2Se_3 nanodiscs [104]. Reproduced with permission from Ref. [104], © Acta Materialia Inc. Published by Elsevier Ltd. All rights reserved 2023.

and sulfuric acid exfoliation. Beyond that, copper atoms are anchored on the g-C_3N_4 defect sites at high temperature, forming a Cu-N_4 coordination structure (Fig. 6(e)). The experimental results show that Cu-g-C_3N_4 can oxidize glucose into H_2O_2 under light conditions. Subsequently, the POD activity catalyzes the generation of ·OH from H_2O_2. This process has a significant bactericidal effect on Gram-positive/Gram-negative multidrug-resistant bacteria and biofilms. The polylactic acid (PCL) was used for electrospinning to fabricate a nanofiber dressing (Cu-g-C_3N_4/PCL). This material can promote wound healing in a mouse infectious wound model. Moreover, it has excellent biocompatibility.

Zhang et al. successfully prepared multifunctional 2D Bi_2Se_3 nanorings by modifying with polyvinylpyrrolidone (PVP) and using the bottom-up method (Fig. 6(f)) [104]. These nanorings possess redox activity. They are capable of eliminating various reactive oxygen and nitrogen species (RONS), such as ·OH, $\cdot O_2^-$, NO, and H_2O_2. As a result, they can increase the survival rate of cells after H_2O_2 stimulation. In the DSS-induced acute colitis prevention and delay model, the Bi_2Se_3 nanorings reduced colonic damage, weight loss, elevated spleen index, and increased levels of pro-inflammatory cytokines by eliminating RONS (Fig. 5(c)). The 16S rDNA amplicon sequencing results show that it can regulate the intestinal microbial community, increase the proportion of *Firmicutes* and *Bacteroidetes*, inhibit the *Proteobacteria*, restore intestinal balance, and has excellent biocompatibility. There are no obvious adverse reactions.

Duan et al. proposed that during the growth stage of two-dimensional crystals, by *in-situ* regulating the gaseous reaction substances, it is possible to cultivate vertically heterostructured MoS_2-$MoSe_2$ and WS_2-WSe_2 with controllable compositions [107]. Zhao et al. grew a graphene/MoS_2 heterojunction on copper foil through plasma-enhanced CVD, which resulted in a tighter interface bonding and improved electron transport efficiency [108]. In summary, the bottom-up approach has many advantages, such as precise and controllable structure, high atomic utilization rate, multi-functional integration, and biocompatibility [109].

The bottom-up assembly strategy synchronously constructs 2D supports and anchors single atoms with precise coordination environments, directly endowing the composite with redox nanozyme activity and broad application prospects in biomedical and environmental governance. For biomedical applications, Zhao et al. realized photoinduced dispersion of Au_{11} nanoclusters into single-atom Au on 2D GO nanosheets, which exhibited typical reductase-like activity for enantioselective hydrogenation; this single-atom Au nanozyme can be used for chiral drug synthesis and precise catalytic treatment of tumor cells, with high selectivity and

biocompatibility [110]. For wastewater treatment, Lu et al. proposed a N-doping-assisted atomic trapping method to synthesize ultrahigh-density single-atom catalysts on 2D N-doped carbon matrices, showing excellent oxidase-like activity for oxygen evolution reaction (OER); this system can efficiently degrade persistent organic pollutants (e.g., antibiotics, dyes) in water and enhance the efficiency of advanced oxidation processes in wastewater treatment [111]. Wang et al. achieved reversible transformation of PdO_x clusters into single-atom Pd on 2D CeO_2 supports via thermal activation, presenting outstanding oxidase-like activity for methane oxidation; this single-atom Pd nanozyme is effective in removing methane pollutants in groundwater and mitigating the environmental hazard of methane emission from aquaculture systems [112].

In summary, top-down and bottom-up strategies represent the core technical routes for the preparation of 2D material-supported single-atom redox nanozymes. The rational integration of 2D support fabrication and single-atom loading directly determines the redox catalytic performance and application suitability of the final system. The complete pathway from 2D support preparation to single-atom anchoring and further to the generation of redox nanozyme activity not only underpins the construction of high-performance single-atom catalysts but also enables their precise translation from laboratory-scale synthesis to biomedical applications and wastewater treatment, laying a solid foundation for the development of next-generation 2D material-supported single-atom redox nanozymes.

2.2.3 Comparison of top-down and bottom-up strategies for 2D material preparation

Table 1 systematically compares the advantages and application scopes of the two main preparation routes of two-dimensional carriers-the top-down and bottom-up methods. The top-down process has mild reaction conditions and can completely retain the intrinsic structure of the layer precursors. The material surface can easily form a large number of defect sites that can be used for single-atom anchoring. However, this method is difficult to precisely control the thickness of the nanosheets and has high difficulty in large-scale preparation, and is only suitable for basic research in a small-scale laboratory setting. In contrast, the bottom-up synthesis can precisely control the thickness, elemental composition, and metal coordination environment of the material at the atomic level. The single-atom is uniformly dispersed and the metal-carrier interaction is stronger, allowing for the simultaneous construction of the two-dimensional substrate and the anchoring of single-atom sites. The drawback is that the synthesis conditions are strict, the process is complex, and the energy consumption is high. It is more suitable for the targeted preparation of high-performance single-atom redox nanoenzymes with precise structural control.

3 Applications of 2D single-atom nanozymes in redox activities

To test whether the nanozymes made of 2D materials loaded with single atoms are active, it is necessary to conduct redox activity tests [113]. The main redox nanozymes involve OXD, POD, CAT, SOD, and GPx activity tests [114]. Table 2 shows comparison of the catalytic substrates, reaction conditions, and detection methods for SOD, OXD, CAT, POD, and GPx.

2D supports regulate redox activity at the atomic level mainly by adjusting the charge transfer, *d*-band center, and M-N_x coordination environment of single-atom sites. Combined with DFT calculations and *in situ* characterization, the regulation mechanism can be summarized as follows [118]: (1) Electron transfer between 2D supports and single atoms optimizes the adsorption energy of reaction intermediates; (2) coordination engineering (N, O, S doping) changes the reaction pathway of OXD, POD, CAT, SOD, and GPx; (3) ROS generation selectivity and catalytic kinetics are determined by atomic-level electronic structure modulation. Such regulation directly controls enzyme activity, substrate selectivity, and catalytic efficiency.

3.1 OXD mimic enzyme

The core function of OXD is to catalyze the oxidation reaction of substrates. It achieves this by activating molecular oxygen to generate ROS, such as $\cdot O_2^-$ or ·OH. It also catalyzes the oxidation of chromogenic substrates (such as TMB, ABTS) to cause color changes [17, 119]. The OXD operates through an oxygen-dependent catalytic mechanism [120]. Its activity is highly dependent on the dissolved oxygen concentration. The catalytic process follows the "adsorption-activation-electron transfer" pathway, and the reaction rate is related to the substrate affinity (K_m) and the maximum reaction rate (V_{max}) [17, 121]. The optimal catalytic activity is usually observed within a pH range of 3.6–6.5 (neutral to slightly acidic) and at temperatures of 30–40 °C. High temperatures or extreme pH values lead to the inactivation of the active sites [119]. The electronic structure of the metal center is regulated by the coordination environment (such as N coordination number, axial Cl coordination), thereby optimizing the oxygen adsorption energy (E_{ads}) and the efficiency of radical generation [17, 119, 122, 123]. Similar to the strategy of introducing phosphorus doping to construct a Cu-N_3P_1 coordination structure, which modulates the electronic metal-support interaction and constructs an active center with a clear Zn-N_4 coordination and enhances catalytic efficiency [124].

Li et al. optimized the OXD-like activity of single-atom Co catalysts (such as the generation of ·OH) by regulating the nitrogen coordination environment of the catalyst [17]. The characteristic of single atoms is dispersion, which can maximize the utilization rate of metal atoms and clearly define the active sites. Combined with

Table 1 Comparative evaluation of top-down and bottom-up preparation strategies

Preparation strategy	Core merits	Inherent limitations	Applicable scenarios
Top-down approaches	Mild synthesis conditions; simple operation; well-retained intrinsic structure of bulk precursors; abundant surface defects for single-atom anchoring	Uncontrollable sheet thickness; low yield; difficult to scale up	Laboratory-scale fundamental research; exfoliation of layered bulk precursors (graphite, MOFs, TMDs)
Bottom-up approaches	Precise atomic-level control of thickness/composition/coordination; high uniformity of single-atom dispersion; strengthened MSI; synchronous construction of 2D supports and single-atom anchoring	Harsh reaction conditions; complex process; high energy consumption	Preparation of high-performance SAzymes with precise structural requirements; scalable synthesis of uniform 2D supports

Table 2 Comparison of the catalytic substrates, reaction conditions, and detection methods for SOD, OXD, CAT, POD, and GPx[a]

Redox nanozyme	Substrate	Reaction conditions	Testing method	Ref.
OXD	O_2, (TMB, ABTS, OPD)	Requires O_2 and optimal pH range of 3.6 to 6.5 (slightly acidic)	1. TMB colorimetric method (absorbance at 652 nm); 2. ESR detection of free radicals (DMPO captures $\cdot O_2^-$/·OH)	[115]
POD	H_2O_2, (TMB, ABTS, OPD)	Acidic conditions with a pH value ranging from 4 to 5	TMB colorimetric method (absorbance at 652 nm)	[115, 116]
CAT	H_2O_2	The pH is neutral to alkaline.	1. Dissolved oxygen detection method; 2. Absorbance of H_2O_2 decreases at 240 nm; 3. Phthalic acid fluorescence method (420 nm)	[117]
SOD	Superoxide anion ($\cdot O_2^-$)	The pH is neutral and requires the participation of metal cofactors.	1. Xanthine/xanthine oxidase system + hydroethidine fluorescence method (610 nm); 2. NBT colorimetric method (absorbance at 560 nm)	[117]
GPx	H_2O_2, organic peroxide, GSH	Requires GSH cofactor and a neutral pH	1. Detection of GSH consumption using the DTNB method; 2. Detection of reduced peroxides using fluorescent probes	[117]

[a]DMPO, 5,5-dimethyl-1-pyrroline N-oxide; DTNB, 5,5'-dithiobis(2-nitrobenzoic acid).

nitrogen coordination regulation, by changing the number of N coordination, the adsorption of oxygen and the ability to clear free radicals are optimized. Taking the oxidation of TMB as a typical catalytic reaction, the OXD-like activity of Co-N_x(C)-SAzyme was studied. Co-N_x(C)-SAzyme exhibited the activity of catalyzing the model reaction and produced a strong blue reaction solution (oxTMB), with its characteristic absorption peak located at 652 nm. By oxidizing two other typical oxidase substrates, ABTS and OPD, the OXD-like activity was further confirmed (Figs. 7(a) and 7(b)). Since non-fluorescent coumarin (COU) molecules can react with ·OH to form 7-hydroxy coumarin (7 HC) with distinct fluorescence characteristic peaks (at 456 nm), this team quantitatively analyzed the concentration of 7 HC (or ·OH) generated by conx(C) in the presence of COU by measuring the luminescence intensity of the standardized compound 7 HC at different concentrations in an acetic acid buffer solution (pH = 3.6) (Fig. 7(c)). It is mainly applied in antioxidant therapy: used to remove excessive $\cdot O_2^-$ in the body and treat oxidative stress-related diseases (such as inflammatory diseases, organ damage).

Zhang et al. employed a high-temperature pyrolysis strategy to synthesize 2D defect carbon nanosheets loaded with monometallic Co catalyst (2D Co-CN(H)) [125]. In the first place, the cobalt precursor (Co(acac)) was embedded into the ZIF-8 framework through the host-guest strategy to prepare the Co-ZIF-8 composite material; furthermore, it was mixed with g-C_3N_4 and subjected to high-temperature pyrolysis in an argon atmosphere. During this process, the corrosive gas produced by the decomposition of g-C_3N_4 could etch the carbon substrate, forming a 2D structure rich in defects. The researchers selected three typical chromogenic substrates, TMB, ABTS, and OPD, to test the oxidase activity of 2D Co-CN(H) (Fig. 7(d)). The results showed that only a clear blue product was observed in the TMB system, with a characteristic absorption peak at 652 nm, indicating that this material has a high substrate specificity for TMB (Fig. 7(e)). Then, an oxygen-dependent verification was conducted, with experiments carried out in N_2 and O_2 atmospheres. It was found that the catalytic activity significantly decreased when in the N_2 atmosphere, while in the O_2 atmosphere, the activity significantly increased (Fig. 7(f)). This phenomenon confirmed that the OXD activity of this material depends on O_2, and its catalytic process involves ROS, such as $\cdot O_2^-$ and $^1O_2$ generation.

3.2 POD mimic enzyme

In the presence of H_2O_2, POD will catalyze the oxidation reaction of the substrate (such as TMB, ABTS, OPD, etc., which are color-developing substrates), thereby generating products with specific colors [126]. By detecting the absorbance of these products at a specific wavelength, the activity of POD can be quantitatively analyzed [127]. Specifically, the strength of the absorbance is proportional to the amount of product generated, and the amount of product generated is closely related to the enzyme's activity [128].

Sun et al. chose ABTS, OPD, and TMB as chromogenic substrates to verify the POD-like activity of Mo-SAN in the H_2O_2-containing system [128]. Results showed that these substrates were oxidized to produce colored products, and TMB was selected as the chromogenic marker due to its oxidation product's high molar absorptivity. Comparing the absorbance of different systems, the Mo-SAN/H_2O_2/TMB system had a characteristic peak at 652 nm, demonstrating Mo-SAN's significant POD-like activity (Fig. 7(g)). The Sun team explored the application of POD activity in Mo-SAN. For visual detection of choline, as choline is converted to H_2O_2 by choline oxidase (ChOx), and Mo-SAN can catalyze H_2O_2's oxidation reaction to form TMB for color manifestation, enabling quantitative analysis of choline. The detection platform has a linear detection range of 0.5–35 μM for choline and a low detection limit of 0.12 μM (Fig. 7(h)). In human serum sample testing, the recovery rate was 96.4%–102.2%, and the RSD was less than 5%. A visual detection platform based on paper-based test strips and smartphones was built for portable and real-time choline detection. Regarding the generation of ROS in tumor cells, Mo-SAN could catalyze the generation of ·OH from endogenous H_2O_2 in tumor cells like HeLa cells, inducing cell death. Using the fluorescent probe 2',7'-Dichlorodihydrofluorescein diacetate (DCFH-DA) for labeling, the green fluorescence signal in cells increased with Mo-SAN concentration, confirming its ability to produce reactive oxygen species in the tumor microenvironment (Fig. 7(i)).

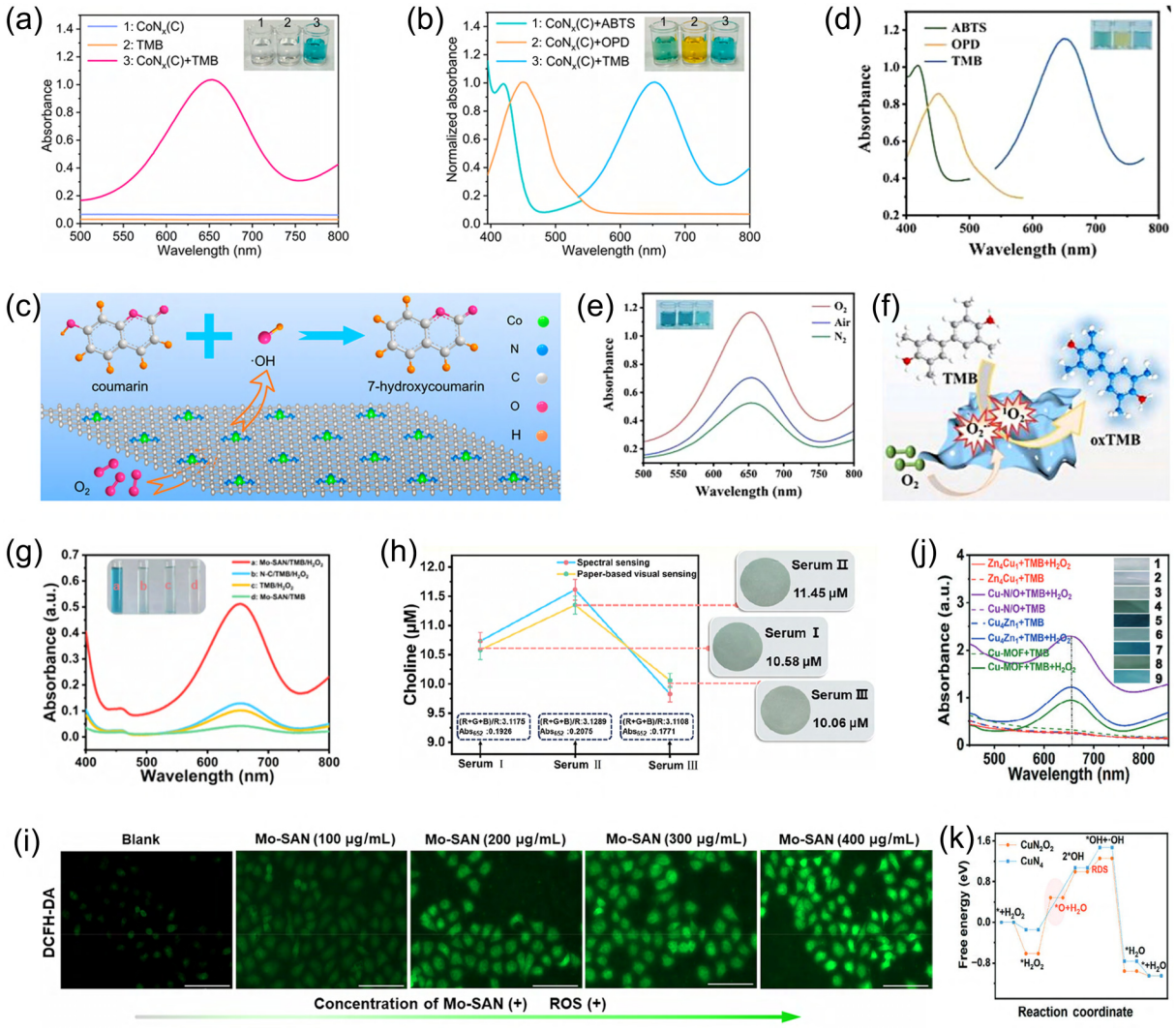


Figure 7 (a) Comparison of UV–vis absorption spectra of different reaction systems [17]. (b) UV–vis absorption spectra of the oxidation of ABTS, OPD, and TMB catalyzed by Co-N_x(C)-Sazyme [17]. (c) The nonfluorescent coumarin (COU) reacts with ·OH to form highly fluorescent 7 HC [17]. Reproduced with permission from Ref. [17], © American Chemical Society 2023. (d) UV–vis spectra of 2D Co-CN(H) catalyzed oxidation of ABTS, OPD, and TMB [125]. (e) UV–vis absorption spectra under different atmospheres [125]. (f) The mechanism diagram of 2D Co-CN(H) of OXD-like activities [125]. Reproduced with permission from Ref. [125], © Zhang, X. et al. Published by Tsinghua University Press 2025. (g) POD-like activity of Mo-SAN [128]. (h) Application of two sensing platforms in the detection of choline in serum samples [128]. (i) Different concentrations of Mo-SAN mediate the formation of ·OH in HeLa cells [128]. Reproduced with permission from Ref. [128], © American Chemical Society 2023. (j) UV–vis absorption spectra of TMB catalytic oxidation. Insets 1–9 show blank, Zn_4Cu_1+TMB, Zn_4Cu_1+TMB+H_2O_2, Cu-N/O+TMB, Cu-N/O+TMB+H_2O_2, Cu_4Zn_1+TMB, Cu_4Zn_1+TMB+H_2O_2, Cu-MOF+TMB, Cu-MOF+TMB+H_2O_2, respectively [129]. (k) Free energy diagram of Cu-N/O catalytic process [129]. Reproduced with permission from Ref. [129], ©Wiley-VCH GmbH 2025.

Moreover, the team's research on the catalytic mechanism and material design provides a technical and theoretical basis for highly active SAzyme. Through the cascade anchoring one-pot pyrolysis method, the loading amount of metal atoms is increased, and the coordination environment is optimized, offering important references for nanozyme development.

Wu et al. regulated the structure of copper mononuclear nanozyme (Cu-N/O) through a cascade competition strategy and systematically studied its peroxidase POD-like activity [129]. Using Zn_4Cu_1 as the precursor, through a cascade competition reaction mediated by the buffer substance polydopamine (PDA), the non-active Zn sites were removed by non-thermal etching in one step, and the coordination environment of Cu was adjusted from Cu-N_4 to Cu-N_2O_2, resulting in the preparation of Cu-N/O mononuclear nanozyme with a high copper loading (5.57 wt%) and a small size (60.74 nm). Compared with Zn_4Cu_1, Cu_4Zn_1 and Cu-MOF, Cu-N/O exhibited stronger adsorption capacity for H_2O_2 (adsorption energy 0.62 vs. 0.14 eV for Cu-N_4), better catalytic kinetic parameters (k_{cat}/K_m of 1.92×10^3 $M^{-1}\cdot s^{-1}$ (TMB as the substrate) and 8.6×10^2 $M^{-1}\cdot s^{-1}$ (H_2O_2 as the substrate)), and could enhance catalytic efficiency by generating ·OH and $\cdot O_2^-$ (Figs. 7(j) and 7(k)). Cu-N/O maintained high POD-like activity under long-term storage, temperature/pH changes, ultrasonic/sonication, etc. (relative activity > 95%), and was successfully applied in lateral flow immunoassay (LFIA), achieving ultra-sensitive catalytic mode detection of *Escherichia coli* O157:H7 (limit of detection 6 CFU/mL).

3.3 CAT mimic enzyme

CAT is a crucial antioxidant enzyme widely present in living

organisms. It catalyzes the decomposition of H_2O_2 into H_2O and O_2, directly eliminating toxic substances produced by cellular metabolism and preventing oxidative damage caused by the accumulation of H_2O_2. In the liver, the high activity of CAT can quickly process the H_2O_2 produced by metabolism, protecting the cell membrane and DNA from damage. As one of the core enzymes in the biological defense system, CAT blocks the free radical chain reaction by eliminating H_2O_2, preventing the formation of more toxic reactive oxygen species such as ·OH, thereby protecting biological macromolecules such as lipids, proteins, and nucleic acids. In immune cells (such as macrophages and neutrophils), CAT decomposes H_2O_2 produced during the killing of pathogens to protect the immune cells themselves from oxidative damage and maintain the normal function of the immune system.

Xu et al. used a one-step ultrasonic method to load copper oxide nanoparticles (CuO NPs) onto the surface of polyoxometalates (POMs) [130]. They successfully synthesized CuO NPs-POM composite materials with four oxidoreductase-like mimicking activities (including CAT) (Fig. 8(a)). Through characterization methods such as transmission electron microscopy (TEM), X-ray diffraction (XRD), and X-ray photoelectron spectroscopy (XPS), it was confirmed that CuO NPs were uniformly distributed on the surface of POMs, forming a flower-like cluster structure with a diameter of approximately 200–300 nm. Moreover, there were redox-active sites such as Mo^{5+}/Mo^{6+} and Cu^{2+}/Cu^{+} in the material.

When studying the catalytic activity of CAT, the research team discovered that the CuO NP-POM composite material could catalyze the decomposition of H_2O_2 into O_2 and H_2O in a phosphate buffer solution (PBS, with a pH value of 6.4). In the experiment, CuO NP-POM (100 μg/mL) was mixed with H_2O_2 (3 mM), and the reaction was conducted at 40 °C for 5 min. The catalytic activity was verified by monitoring the decrease in the intensity of the characteristic absorption peak of H_2O_2 at 240 nm (Fig. 8(b)). Additionally, bubbles were observed in the reaction system, which directly proved the generation of O_2. This is because at a wavelength of 240 nm, the absorbance of H_2O_2 gradually decreases as the reaction time increases. Moreover, the greater the amount of CuO NP-POM added, the more significant the decrease in absorbance becomes. This indicates that CuO nanoparticles-POM can reduce the concentration of H_2O_2 in the system by decomposing H_2O_2. Moreover, after the reaction system is incubated at 40°C, visible

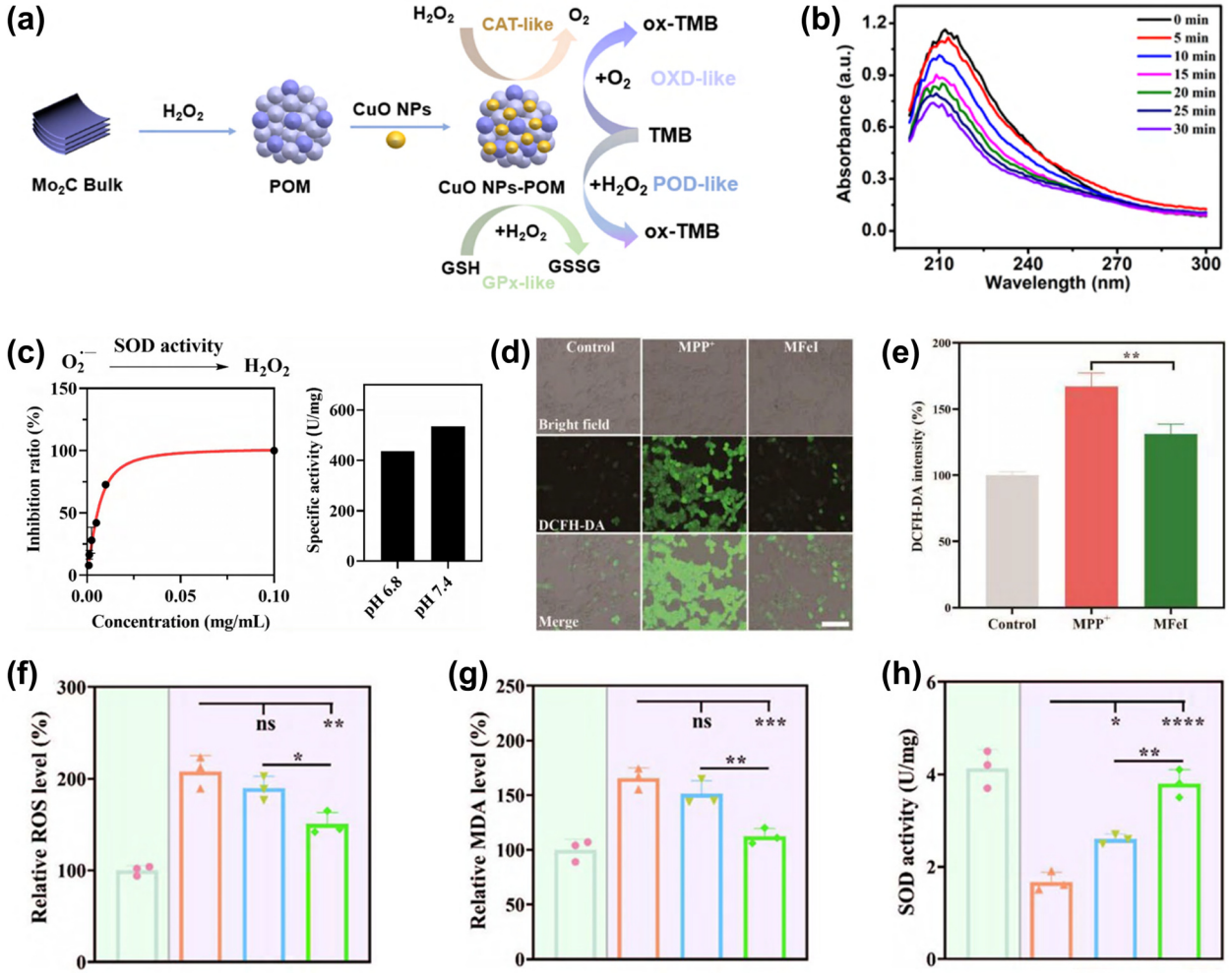


Figure 8 (a) Synthesis of CuO NP-POM and schematic diagram of CAT enzyme mimetic activity [130]. (b) UV absorbance of H_2O_2 at 240 nm with the addition of CuO NP-POM at 240 nm at different times [130]. Reproduced with permission from Ref. [130], © American Chemical Society 2021. (c) The SOD-like activities of Fe-ISAzyme (left) and the specific SOD-like activity of Fe-ISAzyme under different pH (right) [133]. (d) Intracellular ROS levels detected with ROS fluorescent probe DCFH-DA and (e) the corresponding quantitative result, $n = 3$. Scale bar: 50 μm [133]. Based on the levels of (f) ROS, (g) malondialdehyde (MDA), and (h) SOD, the oxidative levels and antioxidant capacity in the SNpc of Parkinson's disease mice were measured [133]. Reproduced with permission from Ref. [133], © Liu, Y. et al. 2024.

bubbles will appear. This further confirms that H_2O_2 is catalytically decomposed into O_2. This is consistent with the typical characteristics of the CAT catalytic decomposition of H_2O_2. The CAT-like activity of CuO NP-POM can be utilized in biomedical scenarios such as alleviating the hypoxic environment of tumors. Furthermore, when constructing the detection platform, this activity can work in synergy with other similar enzyme functions (such as over POD-like activity). And it can indirectly detect the target analyte (such as ascorbic acid) by adjusting the concentration of H_2O_2.

3.4 SOD mimic enzyme

SOD is an important antioxidant enzyme in living organisms. SOD has several functions. It can eliminate $\cdot O_2^-$. It catalyzes the disproportionation reaction of $\cdot O_2^-$, generating O_2 and H_2O_2, thereby reducing the damage caused by free radicals to cells [131]. It can also maintain the redox balance. It plays a core role in the antioxidant defense system and protects biological molecules (such as DNA, proteins, and lipids) from oxidative stress damage. It participates in disease regulation. It is closely related to the occurrence and development of various diseases such as inflammation, aging, and cancer. Abnormal activities of SOD can reflect the oxidative stress state of the body.

The classic testing method usually assesses the SOD activity by measuring the ability to remove $\cdot O_2^-$. For example, using the nitroblue tetrazolium (NBT) photoreduction method, under light conditions, riboflavin photodegradation produces $\cdot O_2^-$, which can reduce NBT to blue methemoglobin at 560 nm with a characteristic absorbance. If the sample has SOD activity, it can remove $\cdot O_2^-$, inhibiting the reduction of NBT, resulting in a decrease in absorbance. The absorbance change can be used to calculate the SOD's clearance rate of $\cdot O_2^-$, thereby evaluating the enzyme activity [132].

Liu et al. synthesized Fe-based SAzyme (Fe-ISAzyme) and tested its SOD-like activity in phosphate buffer solutions (pH 6.8 and 7.4) [133]. The SOD activity of Fe-ISAzyme was strong and mainly exhibited SOD/CAT-like activity under neutral conditions, without OXD/POD activity, avoiding the generation of additional ROS. The researchers detected the changes in SOD activity of Fe-ISAzyme under different pH conditions (pH 6.8 and 7.4). They find that Fe-ISAzyme maintained stable SOD activity within the physiological-related pH range (7.4), suitable for the *in vivo* environment (Fig. 8(c)). They also used electron spin resonance spectroscopy (ESR) technology to generate $\cdot O_2^-$ through the xanthine-xanthine oxidase (X-XOD) system and detect the scavenging effect of Fe-ISAzyme on them. The results showed that Fe-ISAzyme could significantly reduce the generation of $\cdot O_2^-$, proving its efficient SOD mimicking activity. Fe-ISAzyme was encapsulated in liposomes containing triphenylphosphine (TPP), and a mitochondrial-targeted nanozyme (MFeI) was constructed. The MFeI was verified in SH-SY5Y cells for its mitochondrial enrichment ability and SOD activity in clearing ROS. The results showed that MFeI targeted the mitochondria through TPP, using SOD activity specificity to clear ROS from mitochondrial sources, protecting neurons from oxidative damage.

Based on the above research results, the team summarized the applications of Fe-ISAzyme. Firstly, there is the *in vitro* neuroprotective effect. In the MPP^+-induced Parkinson's disease cell model, MFeI reduced intracellular ROS levels through SOD activity, inhibiting neuronal apoptosis (Figs. 8(d) and 8(e)). Secondly, there is the *in vivo* treatment of Parkinson's disease. Through microneedles (MN) *in situ* delivery of MFeI to the mouse brain, the SOD activity on improving neuroinflammation and pathological symptoms was evaluated in the MPTP-induced PD model. MFeI MNs targeted the substantia nigra pars compacta (SNpc) and striatum (ST) through SOD activity to clear ROS, reducing α-synuclein accumulation, restoring tyrosine hydroxylase (TH+) neuron numbers, and improving the motor dysfunction of mice (Figs. 8(f)–8(h)). Thirdly, there is the penetration of the blood-brain barrier and targeted enrichment. MFeI MNs bypassed the blood-brain barrier and directly delivered Fe-ISAzyme with SOD activity to the brain lesion sites, significantly improving the drug's enrichment efficiency in SNpc and ST compared to intravenous injection. Fourthly, there is the synergistic effect of the antioxidant and anti-inflammatory. SOD activity reduces ROS levels, inhibits microglia polarization towards the pro-inflammatory M1 phenotype, and promotes its transformation into the anti-inflammatory M2 phenotype, alleviating the neuroinflammatory microenvironment.

3.5 GPx mimic enzyme

The core function of GPx is to provide antioxidant protection [134]. GPx catalyzes the reduction of H_2O_2, organic peroxides (such as lipid H_2O_2) [135], peroxynitrite [136], and consumes glutathione (GSH) and generates glutathione disulfide (GSSG). Thereby eliminates ROS within the cells and prevents oxidative damage. Among them, Xu et al. stated that GPx4 can specifically reduce membrane-bound phospholipid H_2O_2, inhibiting lipid peroxidation and ferroptosis (Figs. 9(a) and 9(b)) [137]. The core of GPx activity testing is based on the catalytic redox or conjugate reactions involving GSH, quantified by monitoring substrate consumption or product formation. The determination of GPx activity is typically carried out using the coupled NADPH oxidation method: when GPx catalyzes the reduction of H_2O_2 or tert-butyl hydroperoxide (t-BHP), it consumes GSH, while GSSG can be re-reduced to GSH by glutathione reductase (GSSG-Red) using NADPH [138]. The oxidation rate of NADPH at 340 nm is monitored by spectrophotometry to indirectly reflect the activity of GPx.

Domenico Lapenna et al. investigated the relationship between aging and GPx activity [139]. They found that the levels of GSH in tissues of the elderly (such as arteries, lenses, and livers) were significantly reduced. At the same time, the activity of GPx also decreased, thereby leading to enhanced oxidative stress and weakened detoxification ability. The Nrf2 signaling pathway related to aging is inhibited. This inhibition leads to the suppression of the expression of GCL (glutamate cysteine ligase, which is a rate-limiting enzyme in the glutathione synthesis process), thereby affecting the synthesis of glutathione and the production of glutathione enzymes (Fig. 9(c)). The Domenico Lapenna team also took various measures to intervene in the regulation of glutathione enzyme activity. One was supplementing N-acetylcysteine (NAC) and glycine. By providing GSH precursors (cysteine and glycine), it significantly increased the GSH levels in red blood cells and tissues of elderly individuals, enhanced GPx activity, and reduced oxidative damage (such as 4-HNE, a lipid peroxide product). Another was selenium supplementation. As a cofactor of GPx, selenium can enhance the activity of GPx1-4, improve mitochondrial function, and extend the lifespan of model organisms (such as fruit flies and mice). The third was polyphenolic compounds (such as resveratrol and curcumin). Activating the Nrf2 signaling, inducing the

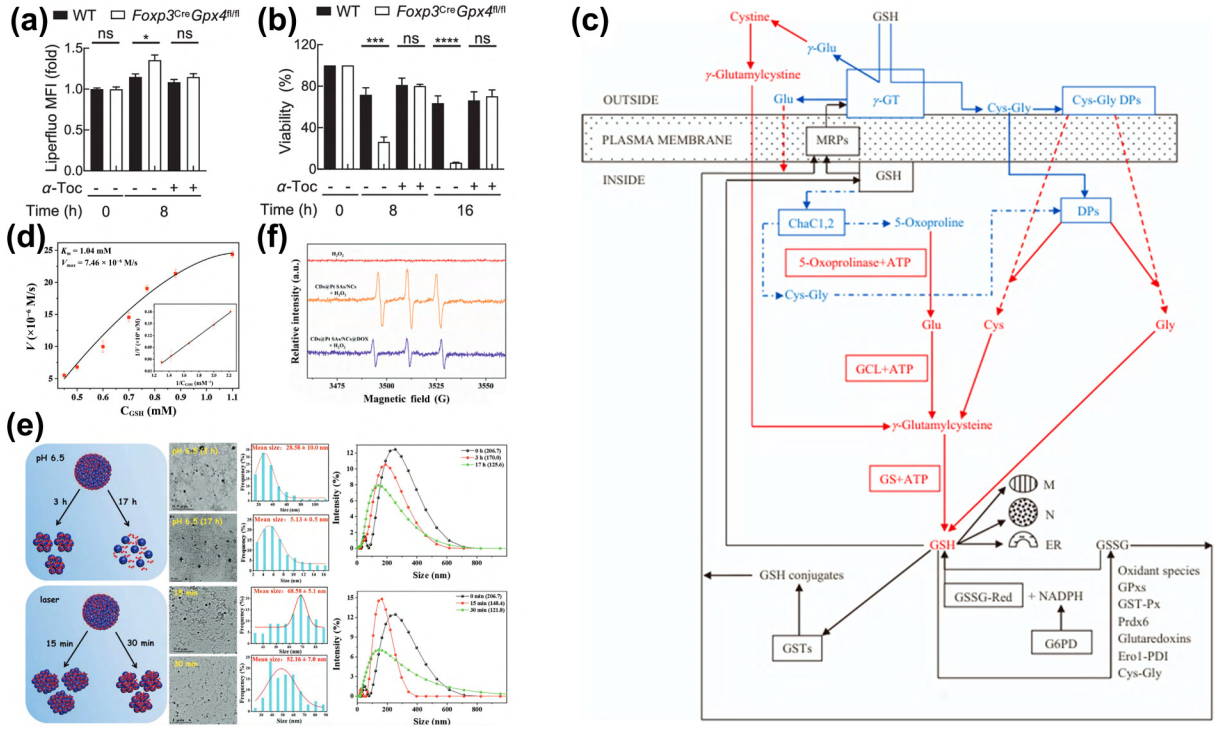


Figure 9 (a) Fold changes of Liperfluo MFI in WT and Foxp3^{Cre}Gpx4$^{fl/fl}$ Treg cells treated with or without 10 μM α-Toc in the presence of α-CD3-CD28 and IL-2 for the indicated time points (n = 5 each group) [137]. (b) Relative viability of WT and Foxp3^{Cre}Gpx4$^{fl/fl}$ Treg cells treated with or without 10 μM α-Toc in the presence of α-CD3-CD28 and IL-2 for the indicated time points (n = 3 each group) [137]. Reproduced with permission from Ref. [137], © Xu, C. et al. 2021. (c) The core pathways of GSH synthesis and degradation, the antioxidant function of the GPx enzyme and GSH, and the regeneration of GSH and redox balance [139]. Reproduced with permission from Ref. [139], © Elsevier B.V. All rights reserved 2023. (d) Michaelis-Menten curve for CDs@Pt SAs/NCs and GSH. Inset: double-reciprocal Lineweaver-Burk plots of CDs@Pt SAs/NCs and GSH [140]. (e) The changes of TEM, particle size, and hydrodynamic diameter of CDs@Pt SAs/NCs@DOX under different treatment conditions [140]. (f) ESR spectra of 2,2,6,6-tetramethylpiperidine (TEMP)/$^1O_2$ adducts in different solutions [140]. Reproduced with permission from Ref. [140], © Zhang, L. et al. Advanced Science published by Wiley-VCH GmbH 2023.

expression of GCL and glutathione enzymes, and enhancing antioxidant capacity.

Zhang et al. constructed a drug-induced Pt mononuclear nanozyme assembly, CDs@Pt SAs/NCs@DOX [140]. This assembly exhibits significant glutathione oxidase (GSHOx)-like activity. It can efficiently consume GSH with a low Michaelis constant (K_m = 1.04 mM) and a high maximum reaction rate (V_{max} = 7.46 × 10^{-6} M/s) (Fig. 9(d)). It avoids depletion of singlet oxygen ($^1O_2$). The GSHOx activity was verified by fluorescence spectroscopy, ultraviolet-visible absorption spectroscopy, and X-ray photoelectron spectroscopy. The results showed that GSH was converted to GSSG and Pt^{2+} was reduced to Pt^{0+}. Meanwhile, this assembly can disassemble and release drugs under the tumor microenvironment or laser control. It also has the function of low-temperature photothermal therapy (PTT), which can effectively regulate the cellular redox homeostasis and achieve high tumor growth inhibition. The disassembly behavior was confirmed by dynamic light scattering and transmission electron microscopy, showing the changes in particle size under different treatment conditions (Fig. 9(e)). The synergistic effect of POD activity (producing $^1O_2$) and GSHOx activity (depleting GSH) is the core mechanism of "regulating cellular redox homeostasis" (Fig. 9(f)). The key parameters of the enzyme activity kinetics curve were obtained by fitting the Michaelis-Menten equation, and the relationship between its activity and the generation of ROS was verified by electron spin resonance spectroscopy.

These studies confirmed that GPx eliminates ROS within cells, which can prevent oxidative damage.

4 Applications in biomedicine and wastewater treatment

As a catalyst, single-atom biocatalysts supported by 2D materials have attracted significant attention in the field of biomedicine [50]. Previous single-atom catalysts dispersed metal atoms independently on carriers with a high surface area. The metal content in most of these single-atom catalysts was very low [141]. But compared with the SAzyme in this paper, this does not guarantee sufficient overall activity, thus limiting the application of single-atom catalysts greatly. The excellent catalytic performance of SAzyme has greatly expanded its application scope in the field of biomedicine. In addition, it has also been applied in wastewater treatment.

4.1 Biomedicine

SAzyme has many excellent properties, which make it suitable for many applications in biomedicine [142]. First of all, SAzyme has a high specific surface area and a unique nanosheet structure, which enables it to fully contact biomolecules and improve the loading capacity and response speed. Compared with traditional drug delivery platforms, SAzyme has a stronger loading capacity and enables efficient drug delivery. Moreover, the ultra-thin 2D structure enables it to show rapid response to external stimuli such as near-infrared laser irradiation and pH changes [143], which facilitates the spatiotemporal controlled release of drugs. Furthermore, SAzyme has excellent biocompatibility. They can be achieved through embedding or peeling into sheet-like forms. As carriers for biological macromolecules or certain drugs, they possess

excellent controlled-release properties. They can enable targeted treatment of diseases while reducing the toxic side effects of drugs and enhancing the bioavailability of the drugs [143–146]. For example, VA single-element nanomaterials have certain advantages in biomedical applications, which are expected to be degraded and metabolized *in vivo* [145]. Through covalent or non-covalent functionalization modification, the stability of SAzyme *in vivo* can be adjusted to further improve its biocompatibility. In addition, the high conductivity, excellent thermal, optical, and mechanical properties of SAzyme provide a variety of possibilities for their applications in the biomedical field. For example, SAzyme of the group VA, such as black phosphorus, has a tunable layer-dependent band gap [145] and can manipulate strong interactions with electromagnetic waves in the ultraviolet to near-infrared wavelength range, making them excellent materials for applications such as biosensing, bioimaging, and optical therapy. SAzyme, such as carbon-based 2D materials, silicate clays, transition metal dihalides, and transition metal oxides, provide enhanced physical, chemical, and biological functions because of their uniform shape, high surface area/volume ratio, and surface charge. Four important applications in the biomedical field described above are detailed below (Fig. 10).

4.1.1 *Cancer treatment*

At present, there are various methods for cancer treatment, each with its advantages and disadvantages [121, 140, 147–150]. For instance, cancer immunotherapy is a method that activates the immune system to identify and eliminate cancer cells. Its anti-tumor effect is long-lasting, and compared to other treatment strategies, it has a lower risk of metastasis and recurrence [151, 152]. Although immunotherapy has been widely used in tumor treatment, it still faces some challenges, such as immune suppression, difficulty in immune infiltration, and limited treatment options [153]. Therefore, it is necessary to introduce SAzyme into cancer treatment. SAzyme has many unique advantages, including high specific surface area, biocompatibility, chemical surface modification, targeting ability, tumor accumulation, and unique physical and chemical interactions [154–156]. They are expected to overcome these limitations and enhance the therapeutic effect by delivering immunotherapeutic drugs, regulating the tumor immune microenvironment, and combining with other treatment methods [157–160].

The mechanism of Fe-based SSNs in cancer treatment is to utilize chemical kinetic therapy. It utilizes endogenous H_2O_2 within the tumor and generates ·OH through Fenton-like reactions to induce cellular oxidative damage. For example, porphyrinic metal-organic framework supported single-atom iron nanoreactors (PSAF NCs), with ZIF-8 as the carrier. The Fe-N_4 SACs, after intravenous injection, are enriched in the tumor through the enhanced permeability and retention effect (EPR), catalyze the generation of ·OH, and simultaneously induce lipid peroxidation to trigger ferroptosis. The tumor suppression rate in mice reached 85% (Figs. 11(a) and 11(b)) [161]. Fe-based SSNs have a high atomic utilization rate and catalytic efficiency. The single-atom dispersed state maximizes the exposure of active sites, and compared with traditional nanoparticles, the catalytic efficiency is improved by approximately 10–100 times [162]. For instance, PSAF NCs achieve efficient Fenton reactions through the Fe-N_4 active center, catalyzing the generation of ·OH in the acidic tumor microenvironment, inducing tumor cell apoptosis [122]. Moreover, due to its natural enzyme-like activity, the Fe-N_x coordination structure is highly similar to heme enzymes (such as catalase), and can simulate various enzyme activities (such as POD, OXD), achieving precise regulation of ROS (Figs. 11(c) and 11(d)) [161]. Fe-based SSNs also have tumor microenvironment responsiveness [163]. The tumor microenvironment (pH 6.0–6.5) can activate the Fenton-like reaction of Fe-based SSNs, avoiding damage to normal tissues [164]. For example, DOX@Fe SANPs release DOX and

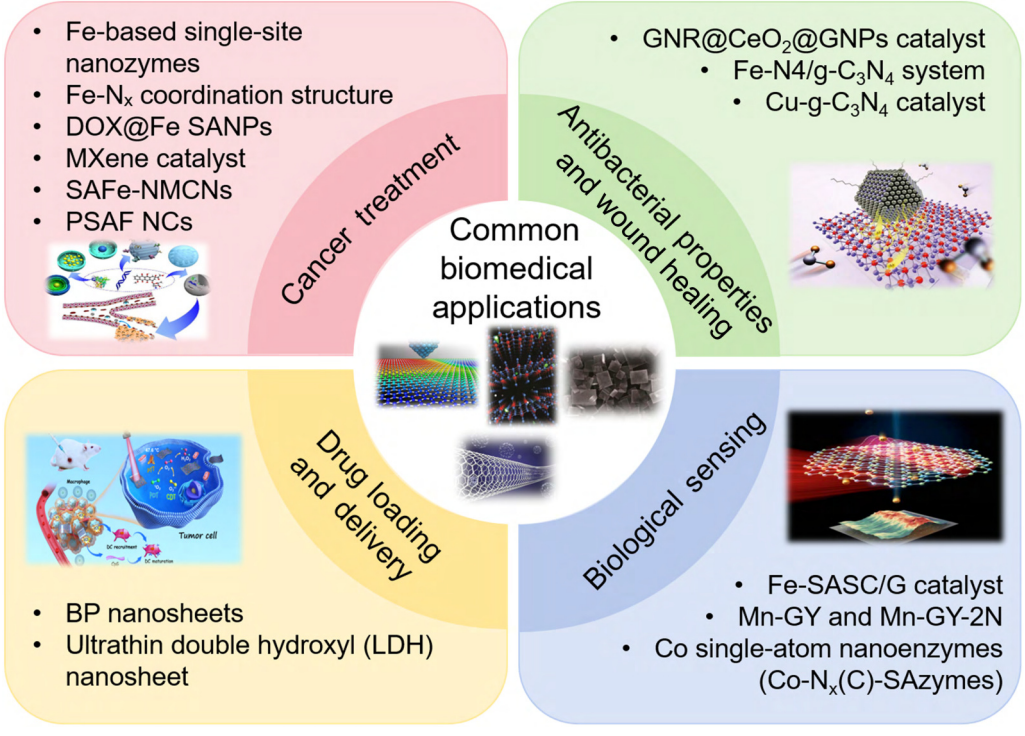


Figure 10 The common applications of the redox activity of SAzyme.

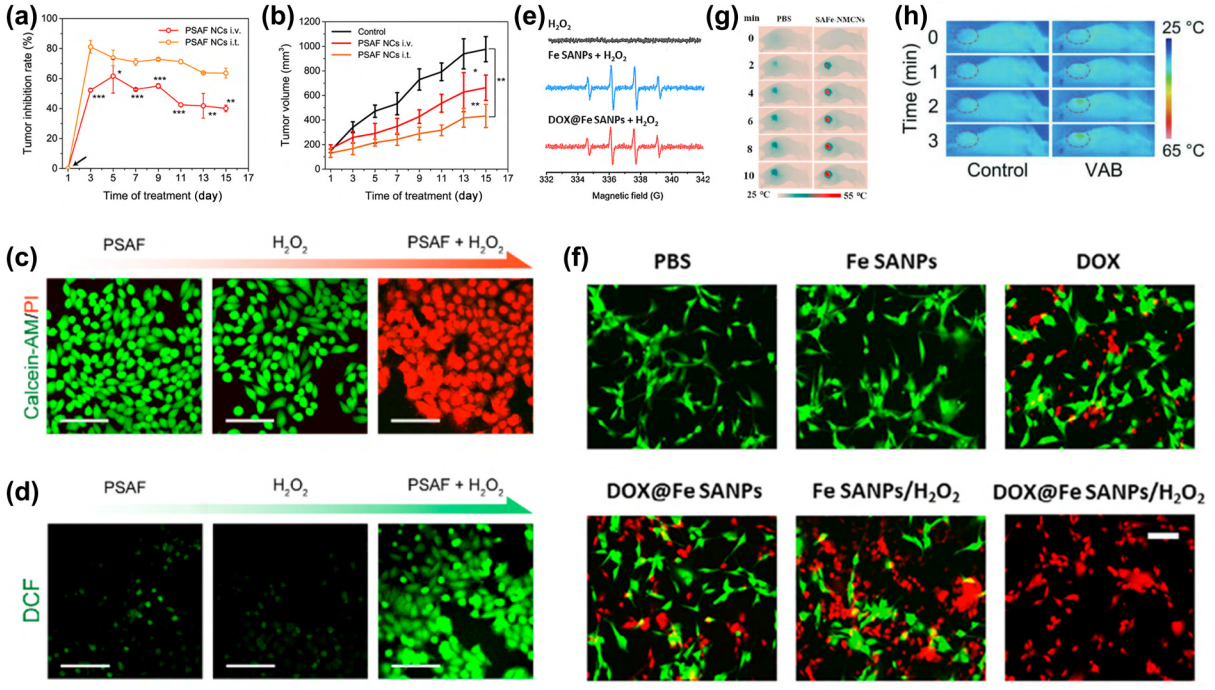


Figure 11 (a) Relative tumor inhibition rates of tumors treated with PSAF NCs intravenously and intratumorally in contrast to the control group [161]. (b) *In vivo* 4T1 tumor proliferation curves of mice treated with or without (saline instead, control group) i.v. and i.t. administrations of PSAF NCs (20 mg/kg) [161]. Confocal microscopic images for cells treated with PSAF NCs, H_2O_2 and their combination prior to (c) Calcein-AM/PI cell-staining or (d) DCFH-DA cell-staining, respectively [161]. Reproduced with permission from Ref. [161], © American Chemical Society 2019. (e) ESR spectra of ·OH trapped by DMPO in the presence of SOD [165]. (f) Live-dead cell staining of HepG2 cells after different treatments (scale bar: 100 μm) [165]. Reproduced with permission from Ref. [165], © The Korean Society of Industrial and Engineering Chemistry. Published by Elsevier B.V. All rights reserved 2022. (g) Time-resolved IR thermal images of tumor-bearing mice under 1064 nm laser irradiation for 10 min after injection with PBS and SAFe-NMCNs nanozyme [166]. Reproduced with permission from Ref. [166], © Elsevier Ltd. All rights reserved 2021. (h) *In vivo* thermal images of 4T1 tumor-bearing mice under 808 nm laser irradiation (0.6 W/cm², 3 min) at 8 h post-administration of VAB [167]. Reproduced with permission from Ref. [167], © Wiley-VCH GmbH 2023.

catalyze the generation of ·OH under acidic conditions, synergistically killing tumor cells (Figs. 11(e) and 11(f)) [165]. The above advantages of Fe-based SSNs play a significant role in cancer treatment. On this basis, Fe-based SSNs can also be combined with other treatment methods, such as photothermal/photodynamic therapy, and have the potential for multi-functional combined treatment. For example, SAFe-NMCNs exhibit both PTT and chemodynamic therapy (CDT) effects under 1064 nm laser irradiation, with a tumor inhibition rate of over 90% (Fig. 11(g)) [166].

The vanadium-based MXene catalyst VAB studied by Zhao et al. also has many advantages and applications in tumor treatment [167]. This catalyst can synergistically disrupt the tumor redox homeostasis through multiple mechanisms. The mixed valence state of V_4C_3 in VAB (V^{3+}/V^{4+}) has POD-like activity, which can catalyze the generation of ·OH from H_2O_2. At the same time, the high-valent vanadium (V^{4+}) oxidizes GSH to GSSG, achieving a dual effect of enhancing the oxidative stress of tumor cells. The released atorvastatin (ATO) acts as a mitochondrial respiratory inhibitor, blocking the electron transport chain complex III, reducing oxygen consumption and ATP synthesis, further weakening the antioxidant capacity of tumor cells. Similarly, the vanadium-based MXene catalyst VAB can also be combined with other treatment methods [168], such as combined treatment with PTT, which can achieve excellent results (Fig. 11(h)). The photothermal effect of VAB directly induces tumor cell necrosis, and the heat-enhanced catalytic reaction generates a large amount of ROS, synergistically killing tumor cells.

Atomic-level regulation of 2D-supported single atoms enables selective ·OH generation, ROS burst, and GSH depletion in the tumor microenvironment [169]. The optimized electronic structure and coordination environment enhance Fenton-like activity and biocompatibility, making such nanozymes ideal for chemodynamic therapy, photothermal therapy, and synergistic cancer treatment.

Collectively, the synergistic effect of 2D materials and single atoms underpins the superior tumor therapeutic efficacy. The high surface-to-volume ratio enriches Fe-N_4/Cu-N_4 active sites to amplify Fenton/Fenton-like reactions; tunable MSI optimizes ROS (·OH) burst and GSH depletion kinetics; coordination-stabilized single atoms maintain catalytic activity in the acidic tumor microenvironment, enabling targeted chemodynamic/photothermal synergistic therapy with a high tumor inhibition rate. Their core strengths lie in maximized atomic utilization, favorable active-site exposure, and tumor-targeted catalytic specificity. Key remaining challenges include long-term *in vivo* biosafety, controllable metal atom leaching, and scalable synthesis for clinical translation.

4.1.2 *Antibacterial properties and wound healing*

The SAzyme exhibits biological-like enzymatic activities, and is determined by its excellent performance in antibacterial and wound healing [148, 170–175]. Some catalysts have multiple biological enzymatic activities and can better kill bacteria [176]. For example, the single-atom Cu-anchored carbon nitride (Cu-g-C_3N_4) catalyst developed by Wu et al. has dual enzymatic activities [106]. It has glucose OXD-like activity, which catalyzes glucose oxidation in the

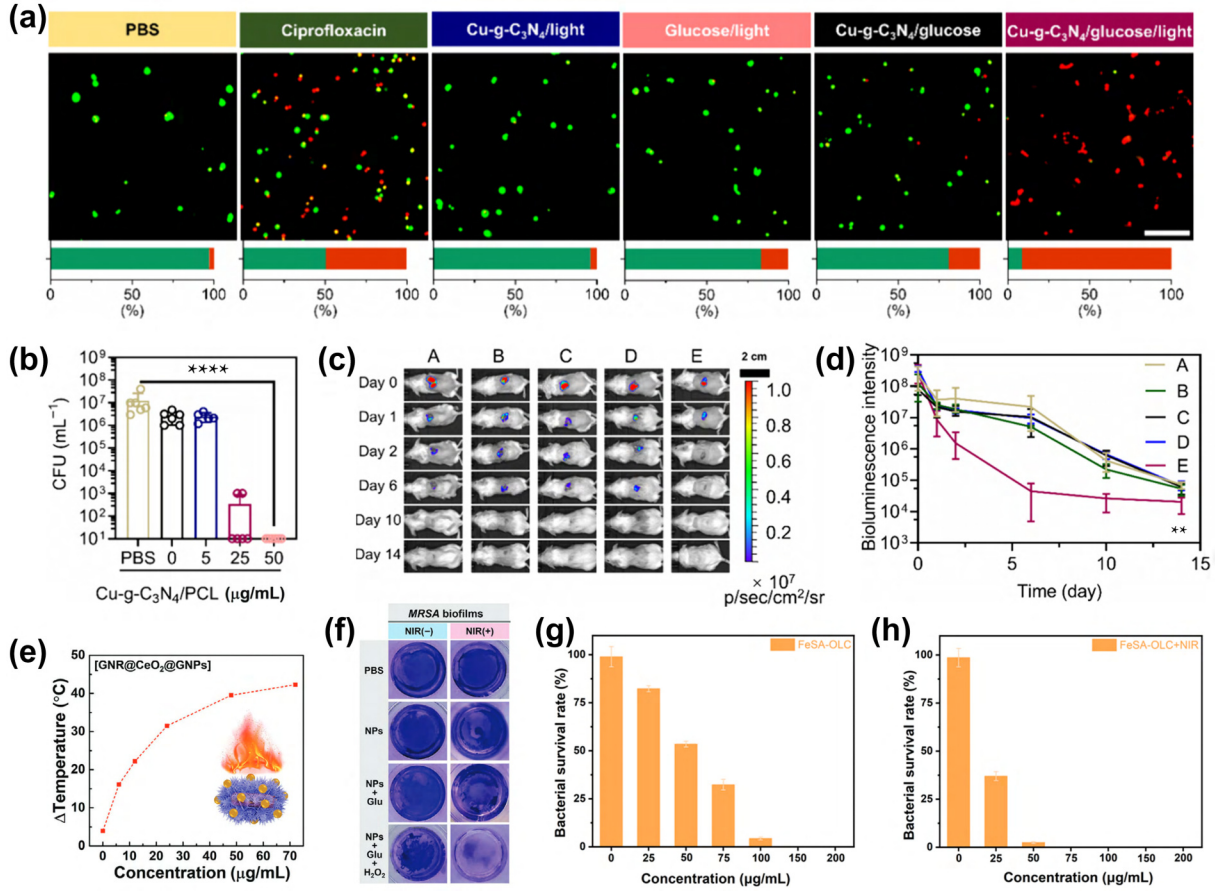


Figure 12 (a) CLSM images and quantification of live/dead staining after 20 min exposure to PBS, ciprofloxacin (12.5 μg/mL), and Cu-g-C_3N_4 nanosheets of planktonic S [106]. (b) Killing efficacy of Cu-g-C_3N_4/PCL nanofibers with different concentrations of Cu-g-C_3N_4 in the nanofibers in the presence of glucose and light irradiation [106]. (c) Bioluminescence images of mice with different treatments on days 0, 1, 2, 6, 10, and 14 [106]. (d) Bioluminescence intensity obtained from panel (c) [106]. Reproduced with permission from Ref. [106], © Wu, F. et al. Published by American Chemical Society 2025. (e) Concentration-dependent photothermal effect of GNR@CeO_2@GNPs under 808 nm irradiation at 1.0 W/cm² [177]. (f) Crystal violet staining assay of MRSA biofilms after different treatments [177]. Reproduced with permission from Ref. [177], © Wiley-VCH GmbH 2024. Bacterial survival rate of *E. coli* treated with (g) FeSA-OLC, and (h) FeSA-OLC + NIR [178]. Reproduced with permission from Ref. [178], © Published by Elsevier Inc. 2024.

presence of light and O_2, generating gluconic acid and H_2O_2. It also has POD-like activity, using the *in situ*-generated H_2O_2 to further catalyze the production of ·OH. Cu-g-C_3N_4 adsorbs bacteria through surface defects, localizing ROS, enhancing the bactericidal effect, and having a bacterial targeting effect. It is effective against both Gram-positive bacteria (such as *Staphylococcus aureus*) and Gram-negative bacteria (such as *Escherichia coli*) (Figs. 12(a) and 12(b)). It also has the unique advantages of SAzyme. Based on these characteristics, Cu-g-C_3N_4 can effectively treat infected wounds. In a mouse model, the Cu-g-C_3N_4/PCL dressing in the infected wound can accelerate healing, and the bacterial bioluminescence signal disappears after 2 days (Figs. 12(c) and 12(d)). Also, the GNR@CeO_2@GNPs catalyst studied by Wang et al. also has good antibacterial performance. It has GOx-like activity to consume glucose [177]. Under 808 nm laser irradiation, GNR@CeO_2@GNPs is activated by glucose, first showing GOx-like activity, oxidizing glucose to gluconic acid and H_2O_2, reducing the local blood sugar concentration and destroying the high sugar environment for bacterial survival (Fig. 12(e)). Moreover, it has POD-like activity to generate ROS, using the generated H_2O_2 as a substrate, and through the POD-like activity of CeO_2, decomposing it to produce a large amount of ROS (such as ·OH), efficiently destroying the bacterial cell membrane and biological macromolecules (Fig. 12(f)).

Fe-based single-atom catalysts (Fe-SACs) catalyze the generation of ·OH from endogenous H_2O_2 through a type of Fenton-like reaction. Thereby, it can disrupt the integrity of bacterial biofilms and cell membranes and exert antibacterial effects. For instance, the Fe-N_4/g-C_3N_4 system developed by Feng et al., which uses graphite-like nitrogen-doped carbon as a carrier to load atomically dispersed Fe single-atom, exhibits a photothermal effect (ΔT = 45 °C) that synergistically enhances the catalytic activity when excited by near-infrared light (808 nm) [178]. This leads to ·OH generation rate of 0.35 μM/min. This material's bactericidal rate is > 99.5% (20 μg/mL, 15 min) against *Escherichia coli* and *Staphylococcus aureus*, and by down-regulating the expression of inflammatory factors IL-6 and TNF-α, it increases the closure rate of infected wounds by 70% (Figs. 12(g) and 12(h)). Its antibacterial performance is closely related to the Fe^{2+}/Fe^{3+} valence state cycling and the enhanced electron transfer efficiency through photothermal enhancement [179].

The atomic-level regulation promotes efficient O_2 activation and ROS production, which disrupts bacterial membranes efficiently. The strong metal-support interaction improves stability and biocompatibility, enabling excellent antibacterial and wound-healing performance [180].

The antibacterial and wound-healing mechanisms of these

nanozymes universally rely on ROS burst via redox enzyme cascade catalysis to disrupt bacterial membranes/biofilms, coupled with photothermal augmentation and reactive oxygen/nitrogen species (RONS) scavenging to relieve inflammation. 2D material-mediated spatial confinement maximizes ROS production via OXD/POD cascade catalysis. Electronic modulation of 2D materials strengthens bacterial adsorption and membrane disruption. Coordination-engineered single atoms ensure sustained catalytic activity. Therefore, they offer broad-spectrum bactericidal activity, low drug resistance induction, and integrated sterilization-repair functions. Current bottlenecks involve anti-interference capacity in complex infection microenvironments and the trade-off between biodegradability and catalytic stability of dressing matrices.

4.1.3 *Drug loading and delivery*

With the rapid development of multidisciplinary nanomedicine and nanobiology, various nanocarriers have been developed for drug delivery, disease diagnosis, and treatment [175]. Black phosphorus (BP) nanosheets are a type of non-metallic layered semiconductor. Thanks to their excellent biocompatibility [181–184], prominent biodegradability, near-infrared (NIR)-induced photothermal effect, and drug loading performance, BP nanosheets have effective photodynamic therapy (PDT) and PTT effects, and can be used for the treatment of various diseases. Therefore, Jin et al. designed a drug delivery system based on BP nanosheets, tested the loading and release characteristics of BP influenza virus nanosheets, and studied the antidepressant effect of BP nanosheets loaded with fluoxetine (Flu) [145]. After adsorption, the zeta potential of the nanosheets decreased from −35 to +15 mV (Fig. 13(a)), indicating that the influenza virus successfully adsorbed on the surface of BP nanosheets through electrostatic interaction, and the drug loading of BP-influenza virus nanosheets was higher than that of the free drug. Studies in human and mouse models have shown that depression is highly correlated with the decreased expression of brain-derived neurotrophic factor (BDNF) in the hippocampus, and this condition can be improved through antidepressant treatment. The measurement of BDNF expression in the mouse hippocampus (Fig. 13(b)) showed that chronic unpredictable mild stress (CUMS) significantly downregulated the expression of *BDNF* mRNA compared to the non-stress control group, and after two weeks of treatment with BP-influenza (BP-Flu-NIR), the *BDNF* expression in the hippocampus increased. The BDNF level in mice unaffected by CUMS reached the normal level. The use of normal saline alone was ineffective, while BP-Flu-NIR treatment was superior to using the non-fluorine drug alone. This indicates that BP nanosheets improve the biocompatibility of influenza (an antidepressant drug) and work in synergy with near-infrared PTT, improving the permeability of the blood-brain barrier and significantly shortening the treatment time for depression, which is a rapid and effective antidepressant strategy.

To fully utilize the potential of nanoparticle drug delivery, Zhang et al. constructed a 2D ultrathin layered double hydroxide (LDH) nanosheet, which has a very high drug loading capacity, excellent dispersion stability, and prolonged circulation time in the blood, and is used for the treatment of malignant tumors [143]. These nanosheets were synthesized through a biocompatible polymer-assisted bottom-up approach. In this approach, mixed metal ions were precipitated together with NaOH to form LDH seeds/cores. Then, POEGAb-PMAEP with an average of two phosphate groups per polymer chain was added to terminate nucleation and promote particle growth along the *ab* plane. After aging treatment, P-LDH nanosheets (Fig. 13(c)) were obtained. Finally, the anti-tumor drug doxorubicin (DOX) was loaded onto P-LDH nanosheets (P-LDH-DOX) through electrostatic interactions. Therefore, it has an ultrathin two-dimensional sheet-like structure, which can provide a large number of cargo anchoring sites for drug loading, thereby achieving an extremely high drug loading capacity of 734% (DOX/nanoparticle mass ratio). After loading DOX, there was a strong electrostatic interaction between doxorubicin and P-LDH (Fig. 13(d)). The *in vivo* therapeutic effect of P-LDH-DOX was further explored through a 4T1 breast cancer xenograft white mutant experimental mouse model. P-LDH-DOX treatment reduced the tumor volume by 76.8% ± 4.5% on the 12th day (Fig. 13(e)), which was significantly greater than LDH-DOX (56.4% ± 12.2%) and DOX (42.9% ± 15.1%). P-LDH-DOX and LDH-DOX significantly inhibited tumor growth. The results clearly

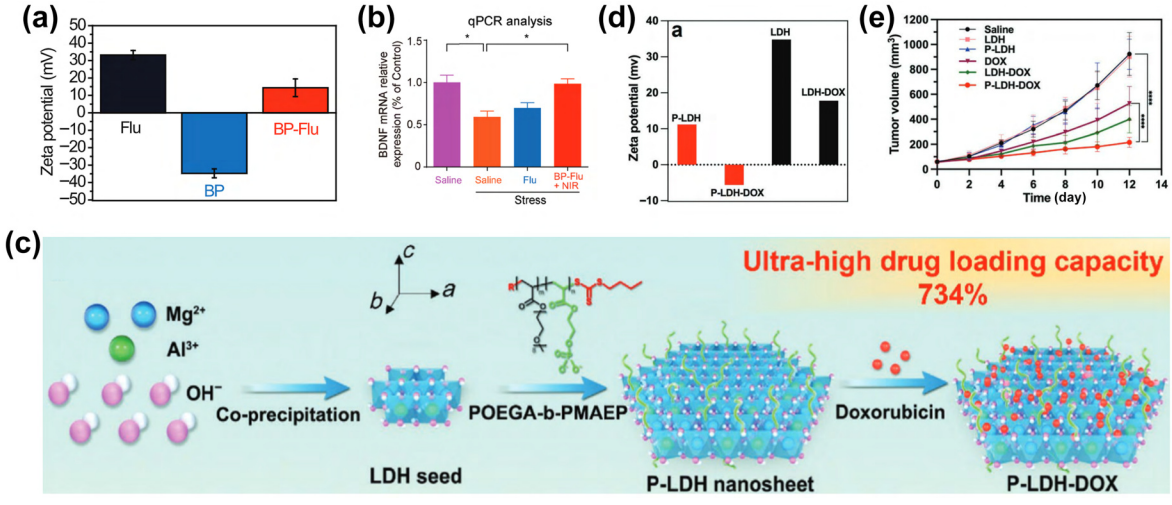


Figure 13 (a) Zeta potential analysis of Flu, BP nanosheets, and BP-Flu [145]. (b) Quantitative polymerase chain reaction (qPCR) analysis of *BDNF* mRNA expression levels in each group of mice [145]. Reproduced with permission from Ref. [145], © WILEY-VCH Verlag GmbH & Co. KGaA, Weinheim 2019. (c) Synthesis route of P-LDH-DOX [143]. (d) Evaluation of DOX loading capacity of LDH and P-LDH at different feed mass ratios [143]. (e) Efficacy analysis of saline, LDH, P-LDH, DOX, LDH-DOX, and P-LDH-DOX measured on tumor volume from day 0 to 12 [143]. Reproduced with permission from Ref. [143], © Zhang, H. et al. Small published by Wiley-VCH GmbH 2022.

demonstrated that doxorubicin delivered through P-LDH nanosheets has superior anti-tumor effects *in vivo*, even stronger than that of free doxorubicin or multi-layer LDH nanosheet-delivered doxorubicin.

The large surface area and tunable surface charge of 2D materials, regulated at the atomic level, enhance drug loading and stimuli-responsive release, realizing targeted delivery and reduced side effects [185].

2D single-atom nanozymes enable high-efficiency drug delivery through high specific surface area-enabled massive loading, atomic-level interface modulation for pH/light-triggered controlled release, and single-atom engineering-improved biocompatibility. Their prominent advantages include ultrahigh drug-loading capacity, targeted delivery to reduce off-target toxicity, and spatiotemporally controllable release. Unresolved issues concern uniform drug loading, *in vivo* circulation stability, and penetration across physiological barriers.

4.1.4 *Biological sensing*

The application of SAzyme in biosensors has made remarkable progress in recent years, especially in biomedicine and health monitoring [186, 187]. These materials are widely used in various sensors on account of their unique physicochemical properties, such as high sensitivity, large detection range, extremely long lifetime, and excellent biocompatibility [125].

In order to simultaneously detect multiple bisphenol substances, Xia et al. used graphyne (GY) and N-doped graphyne (GY-2N) as carriers, and through loading $Mn(acca)_3$ and thermal decomposition, prepared two manganese single-atom nanozymes, Mn-GY and Mn-GY-2N (Fig. 14(a)) [188]. By taking advantage of the differences in POD-like activities of Mn-GY, Mn-GY-2N, and GY-2N, a high-throughput colorimetric sensor array was constructed. When the bisphenol substances bind to the surfaces of the nanozymes, their catalytic activities are inhibited, and the degree of inhibition varies for different bisphenol substances, thereby generating characteristic response signals. The oxidation degree of TMB during the catalytic reaction was monitored by ultraviolet–visible spectroscopy, and the sensor array data were analyzed using machine learning algorithms to achieve the identification and quantitative detection of bisphenol substances. The results showed that the sensor array had good linear relationships for five bisphenol substances (bisphenol A (BPA), BPS, BPF, BPAF, diphenolic acid) in both low and high concentrations, with detection limits (LOD) of 0.443, 0.280, 0.277, 0.424, and 0.326 μM, and high sensitivity (Fig. 14(b)). By combining LDA and HCA algorithms, the sensor array can effectively distinguish different types of bisphenol substances, even in mixed samples, and accurately identify them. For example, the detection of binary and ternary bisphenol mixtures showed that different proportions of mixtures could be clearly clustered. This research can be practically applied in the detection of actual samples, such as canned fruit foods, and the sensor array

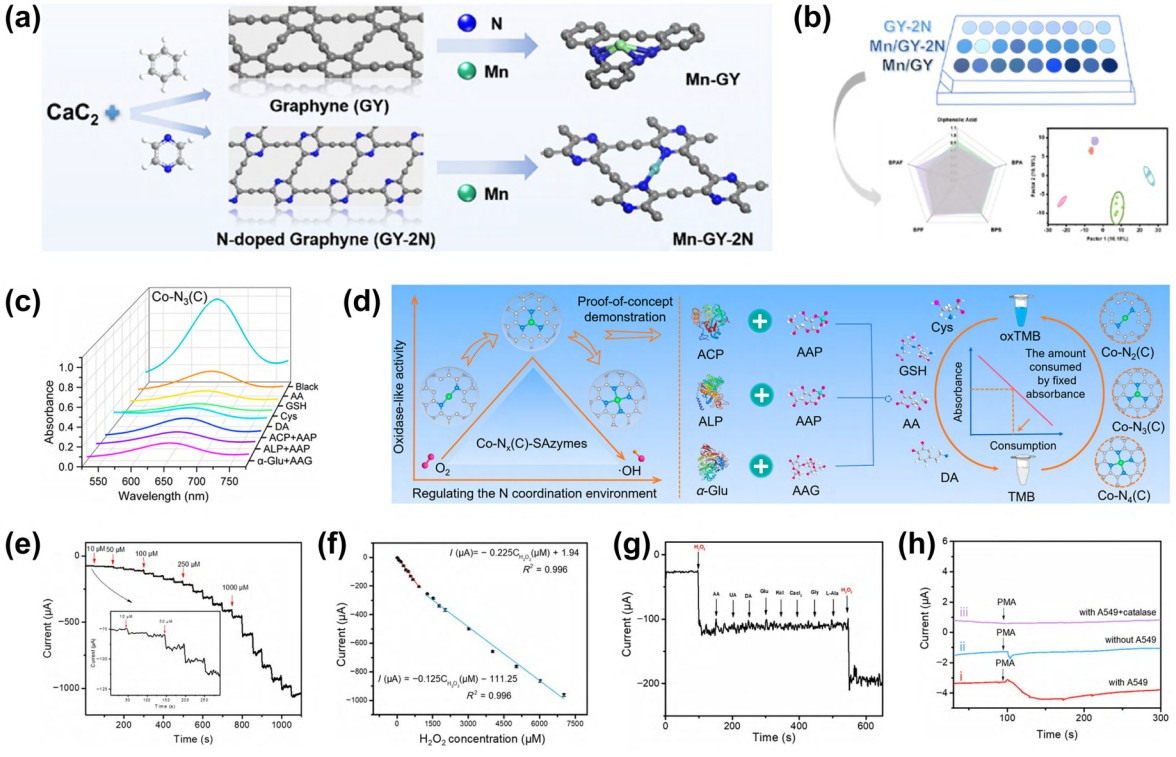


Figure 14 (a) Schematic diagram of the synthesis of bisphenol nanozymes [188]. (b) Schematic diagram of the high-throughput sensor array constructed with three types of nanozymes for detecting bisphenols [188]. Reproduced with permission from Ref. [188], © Elsevier B.V. All rights are reserved, including those for text and data mining, AI training, and similar technologies 2024. (c) Feasibility experiments on the consumption capacity of Co-N_3(C) for four reducing substances and three biological enzymes [17]. (d) Comparison of the oxidase-like activity of Co-N_x(C)-SAzyme by comparing the consumption capacity of Co-N_x(C) for four reducing substances, as well as three biological enzymes [17]. Reproduced with permission from Ref. [17], © American Chemical Society 2023. (e) Chronoamperometric responses to the continuous addition of H_2O_2 at an applied potential of −0.2 V vs. Ag/AgCl in PBS [189]. (f) Linear plots of the Fe-SASC/G sensor for H_2O_2 [189]. (g) Selective performance of the Fe-SASC/G biomimetic sensor [189]. (h) Amperometric responses of the Fe-SASC/G sensor with the addition of 5 μL of PMA (6.25 μg/mL) at −0.2 V in (i) PBS containing 1×10^6 A549 cells, (ii) PBS, and (iii) PBS containing 1×10^6 A549 cells and 450 U/mL catalases [189]. Reproduced with permission from Ref. [189], © American Chemical Society 2022.

successfully identified the bisphenol substances in them, demonstrating its practicality in food safety detection. It provides a new method for the rapid detection of bisphenol substances in food packaging, helps improve the level of food safety monitoring, and has potential application prospects in environmental and biological analysis fields.

Based on the OXD mimicking activity of Co SAzyme (Co-N_x(C)-SAzyme), Li et al. constructed a colorimetric sensing system for detecting reducing substances and biological enzymes [17]. By regulating the N coordination environment around the Co catalytic site (N coordination number x = 2, 3, 4), they optimized the OXD activity. Among them, Co-N_3(C) exhibited the best catalytic performance given its strong O_2 adsorption ability and high efficiency in generating ·OH. This system uses Co-N_3(C) to oxidize the colorless substrate TMB into the blue product oxTMB. When there are reducing substances (such as ascorbic acid (AA), GSH, etc.) or biological enzymes (such as alkaline phosphatase ALP, acid phosphatase ACP, etc.) in the system, oxTMB is reduced, resulting in a decrease in absorbance at 652 nm. The absorbance change at this wavelength is monitored to achieve quantitative analysis (Figs. 14(c) and 14(d)). The results show that Co-N_3(C) can achieve low-concentration detection of various substances (such as AA detection range 0.01–10 μM) through a standard curve, providing a new method for high-sensitivity biosensing.

Li et al. achieved the anchoring of single-atom Fe on 2D nitrogen-doped graphene (N-doped graphene) through two-step high-temperature pyrolysis and acid washing, forming the Fe-SASC/G catalyst [189]. The 2D graphene provides a large surface area and high conductivity, while nitrogen doping enhances the electronic regulation of Fe active sites. The spacing between adjacent Fe single atoms matches the O-O distance bond length in H_2O_2, promoting the bridging adsorption mode. The biosensing performance is excellent, with high sensitivity. The sensitivity for H_2O_2 detection reaches 3214.28 μA/(mM·cm^2), being the best among Fe-based catalysts at present (Figs. 14(e) and 14(f)). It can respond quickly, with a response time of 2.85 s. It shows almost no response to biological interferences such as AA and dopamine (DA), and has excellent selectivity (Fig. 14(g)). This team successfully used this catalyst to *in situ* monitor the release of H_2O_2 from A549 living cells stimulated by phorbol 12-myristate 13-acetate (PMA), with a detection limit as low as 0.02 μM (Fig. 14(h)).

Atomic-level modulation improves substrate selectivity and electron transfer rate, enabling high sensitivity, low detection limit, and strong anti-interference ability in biosensing [190].

In biosensing applications, these nanozymes achieve high-performance detection by precisely regulating redox catalytic kinetics at single-atom sites, accelerating electron transfer via 2D supports, and realizing signal amplification through substrate-specific recognition. They exhibit ultrahigh sensitivity, low detection limits, strong anti-interference, and rapid response. Persistent challenges include adaptability to complex biological matrices (serum, tissue fluid), batch-to-batch consistency, and stability for *in situ* real-time detection.

4.2 Wastewater treatment

Polluted water has always been a major environmental issue and has received much attention from people. Sewage treatment is an urgent need at present to ensure the ecological environment and the sustainable development of human society. Redox nanozyme has many important applications in sewage treatment, which have positive significance for improving the efficiency of sewage treatment, protecting the environment, and achieving sustainable development [191].

Sun et al. developed the SA-Mn-CN/PVDF membrane reactor, which has high degradation efficiency and can remove various organic micropollutants (OMPs) such as tetracycline hydrochloride (TCH) with a removal rate of over 92% within 1 min [192]. After continuous operation for 30 min, TCH can be completely removed (Fig. 15(a)). This is because of its POD-like activity. Its anti-pollution ability is also strong. The water contact angle decreased from 87° to 95° for pure PVDF membranes to 41° to 42°, increasing in flux. In the filtration experiments of bovine serum albumin (BSA) and humic acid (HA), the flux retention rate of the SA-Mn-CN/PVDF/peroxymonosulfate (PMS) system was more than 30% higher than that of pure PVDF membranes, attributed to catalytic oxidation and charge repulsion. The working pH range is wide (3–11), and is not interfered with by common anions (NO_3^-, Cl^-, SO_4^{2-}, HCO_3^-). In actual water bodies such as tap water, river water, and pharmaceutical wastewater, the OMPs removal rate is over 92%, showing merit in environmental adaptability (Fig. 15(b)). It can continuously treat wastewater. During a 72-h continuous operation, the TCH removal rate is stable at 99%, and the manganese release is less than 0.05 mg/L (below the EPA standard) (Fig. 15(c)). The removal rate of mixed pollutants (sulfamethoxazole, levofloxacin, etc.) is 92%–100% (Fig. 15(d)). The antibacterial performance is good. The SA-Mn-CN/PMS system has a killing rate of > 98.9% against *Escherichia coli* and methicillin-resistant *Staphylococcus aureus* (MRSA), and the membrane reactor can simultaneously achieve pollutant degradation and bacterial inactivation.

Zhong et al. proposed a strategy combining data-driven prediction and precise synthesis, aiming to achieve efficient wastewater purification by screening high-performance SACs and optimizing their structures [193]. First step, a data-driven screening was conducted, selecting high-activity sites (Fe-N_4) from 43 metal-N_4 structures through DFT calculations, and predicting their ability to catalyze the production of reactive oxygen species (such as singlet oxygen $^1O_2$). Afterwards, precise synthesis was carried out, using the hard template method (SiO_2 nanoparticles as the template) to control the synthesis of Fe-SACs, adjusting the metal loading (up to 3.83 wt%) and mesoporous structure to enhance the exposure of active sites and mass transfer efficiency, thereby improving the efficiency of wastewater purification. This catalyst maintained high efficiency in degrading within the pH range of 4–10, breaking through the pH limitation of traditional catalysts (Fig. 15(e)), and removing more than 90% of various antibiotics and phenolic pollutants (such as sulfamethoxazole (SMX), sulfamonomethoxine (SMM), sulfadimethoxine (SDM)) within 5 min, demonstrating strong universality (Fig. 15(f)). Even under the interference of 100 mM salts (such as NO_3^-, SO_4^{2-}) and 20 mg/L humic acid, the removal rate of SMX remains close to 100%, indicating strong anti-interference ability (Fig. 15(g)). After 10 cycles, the removal rate of SMX remains 100%, with Fe ion leaching < 9 μg/L, showing excellent stability (Fig. 15(h)).

Xu et al. prepared and studied Fe/N-biochar through a simple pyrolysis process [194]. Using sawdust, $FeCl_3·6H_2O$ and dicyandiamide as raw materials, and calcination at 800 °C in an N_2 atmosphere for 1 h, Fe/N-biochar was obtained. The co-doping of Fe and N in its structure significantly enhanced the adsorption activity. The maximum adsorption capacity for BPA reached

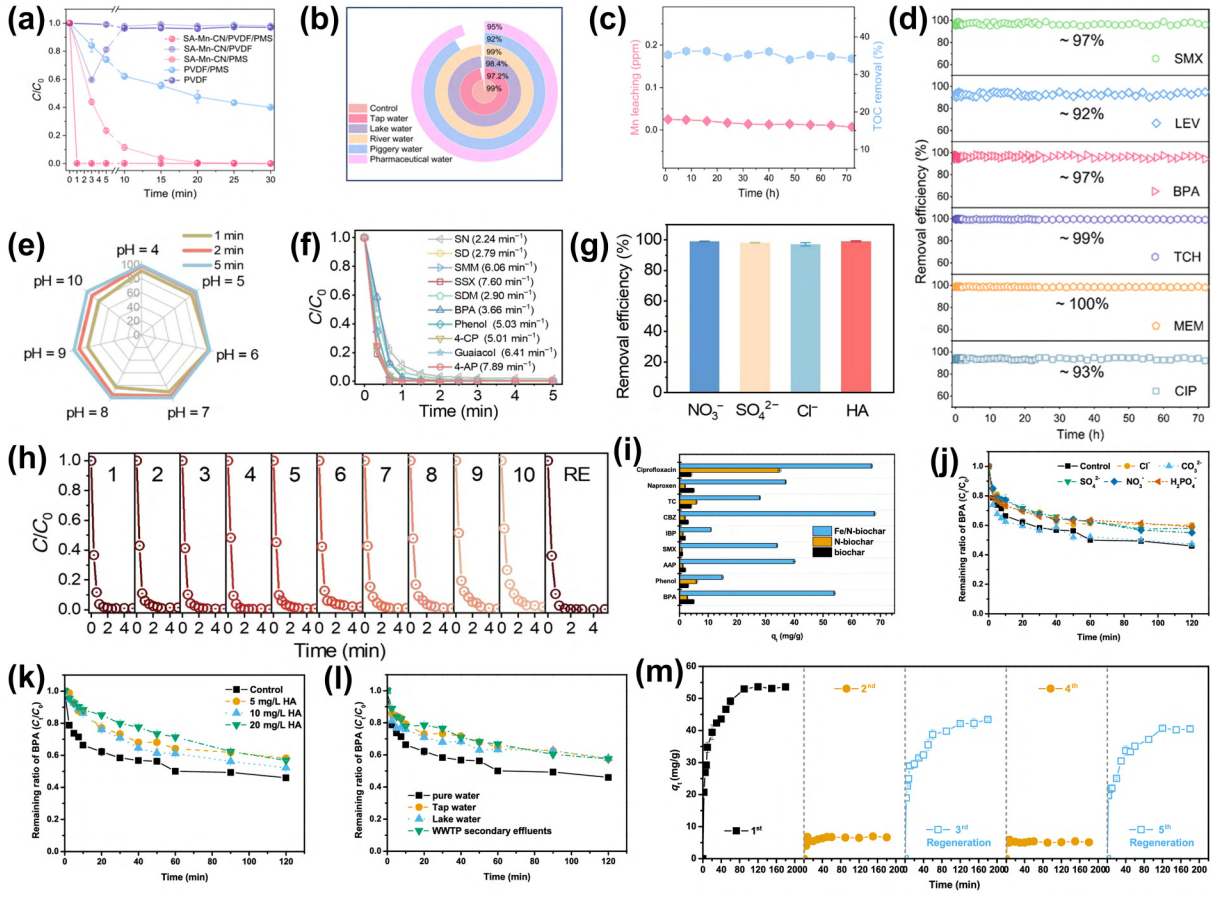


Figure 15 (a) TCH degradation in the various membrane systems [192]. (b) TCH removal in the various water matrices using the SA-Mn-CN/PVDF/PMS system [192]. (c) Mn leaching and TOC removal in the SA-Mn-CN/PVDF/PMS system [192]. (d) Treatment of the mixture pollutants in the SA-Mn-CN/PVDF/PMS system [192]. Reproduced with permission from Ref. [192], © Elsevier Ltd. All rights are reserved, including those for text and data mining, AI training, and similar technologies 2024. (e) Influence of pH on SMX degradation in the Fe-SAC-4/PMS system [193]. (f) Degradation profile of antibiotics and phenolic pollutants in the Fe-SAC-4/PMS system within 5 min [193]. (g) Removal efficiency of SMX by the Fe-SAC-4/PMS system with interference of 100 mM salts and 20 mg/L humic acid [193]. (h) Cyclic SMX degradation performance of Fe-SAC-4 [193]. Reproduced with permission from Ref. [193], © Zhong, K. -Q. et al. Angewandte Chemie International Edition published by Wiley-VCH GmbH 2023. (i) Adsorption capacities for different micropollutants onto Fe/N-biochar [194]. (j) Effects of co-occurring inorganic anions [194]. (k) Effects of concentration of humic acid [194]. (l) Effects of quality of the water matrix on the adsorptive removal of BPA by Fe/N-biochar [194]. (m) Regeneration and recyclability of Fe/N-biochar for BPA adsorption [194]. Reproduced with permission from Ref. [194], © Elsevier B.V. All rights reserved 2021.

54 mg/g, and it showed efficient adsorption capabilities for eight kinds of trace pollutants, such as phenol and sulfamethoxazole (Fig. 15(i)). Graphitized N and Fe-N_x are the main adsorption sites, and their content is positively correlated with the adsorption capacity. After adsorption, the relative content of both decreased significantly. It has strong anti-interference ability, and the pH (3.0–10.0), inorganic anions (Cl^-, CO_3^{2-}, etc.) and humic acid have little effect on adsorption (Figs. 15(j) and 15(k)). In tap water, lake water and secondary effluent of sewage, the BPA removal rate still reached 41%–42%, which has great practical application value (Fig. 15(l)). Simple thermal treatment can effectively regenerate, and after repeated use four times, the adsorption capacity remains above 80% of the initial value (Fig. 15(m)).

Atomic-level regulation enhances the redox activity and stability over a wide pH range [195]. The 2D structure accelerates mass transfer, enabling efficient degradation of antibiotics and organic pollutants in complex water environments.

5 Conclusions and prospects

This review focuses on the research regarding the application of 2D materials loaded with single-atom redox nanozyme. This review provides a systematic and comprehensive overview of the preparation processes, catalytic properties, diverse applications and corresponding underlying mechanisms of 2D material-engineered single-atom redox nanozymes. It clarifies how 2D materials regulate single-atom sites at the atomic level. The three modes of action (spatial confinement, electronic modulation and coordination engineering) determine the redox pathways, ROS behavior and substrate selectivity. This review tightly interlinks the relationships among mechanism, activity, and application. 2D materials, with their high specific surface area and tunable electronic structure [196], have become ideal carriers for single-atom loading. The materials can be prepared controllably through "top-down" (such as liquid exfoliation, ionic intercalation) and "bottom-up" (such as chemical vapor deposition, hydrothermal synthesis) approaches. The constructed SAzyme exhibits excellent redox activity, covering SOD, OXD, CAT, POD, and GPx, etc. In terms of application, these SAzyme demonstrate significant advantages in the biomedical field: by catalyzing the generation of ROS or eliminating free radicals, they can be used for chemical kinetic therapy of cancer, photothermal/photodynamic combined therapy; the application of SAzyme in antibacterial and wound healing fields mainly relies on

their simulation of natural enzyme catalytic activity, achieving efficient sterilization through mechanisms such as generating ROS and disrupting the bacterial microenvironment, and promoting tissue repair; in drug loading and delivery, the high specific surface area of SAzyme enables efficient drug loading (such as doxorubicin) and controlled release in response to tumor microenvironment (pH, near-infrared light); in the field of biosensing, based on the mechanism of redox inhibition or signal amplification, high-sensitivity detection platforms for small molecules (such as choline) and biological macromolecules (such as microRNA) have been constructed. Moreover, in wastewater treatment, materials such as SA-Mn-CN/PVDF membrane reactors efficiently catalyze the degradation of pollutants like antibiotics, demonstrating good environmental adaptability and cycle stability.

Despite remarkable progress, this field is still at the proof-of-concept stage. Future development requires breakthroughs in theoretical guidance, standardized evaluation, and translational research.

First, DFT should be further integrated to guide the rational design of SAzymes. DFT calculations can accurately predict the optimal active site configuration (e.g., M-N_4, M-N_2O_2), simulate the adsorption--desorption behavior of reaction intermediates, calculate the *d*-band center position and reaction energy barrier, and reveal the synergistic mechanism between 2D supports and single-atom sites. High-throughput DFT screening combined with machine learning can accelerate the discovery of high-activity SAzymes, replacing inefficient trial-and-error synthesis.

Second, unified experimental standards are urgently needed to evaluate catalytic activity under real-world conditions. Current tests mostly rely on ideal buffer systems; future evaluations should adopt complex physiological matrices (serum, interstitial fluid) or actual environmental matrices (river water, industrial wastewater). Standardized protocols should be established for pH, temperature, substrate concentration, catalytic kinetics (K_m, V_{max}), long-term stability, anti-interference ability, and metal ion leaching, to ensure reliable and comparable results across studies.

Third, clear step-by-step pathways are required to translate lab-scale achievements into clinical and industrial applications. For clinical translation, the steps include: (1) developing mild, scalable synthesis to produce SAzymes with uniform size and stable activity; (2) systematic biosafety assessment (acute/chronic toxicity, biodegradation, metabolic pathway, and metal leaching); (3) preclinical verification in large animal models; (4) clinical trial validation.

For industrial translation, key steps include: (1) low-cost mass production with low energy consumption and high metal utilization; (2) integration with engineering devices (membrane reactors, continuous-flow catalytic systems); (3) validation of long-term operation stability and cost-effectiveness; (4) compliance with environmental and health regulations.

With advances in atomic-level synthesis, theoretical simulation, and translational engineering, 2D material-supported single-atom redox nanozymes will gradually move from fundamental research to practical applications, providing new solutions for biomedical diagnosis/treatment and environmental remediation.

Data availability

Not applicable.

Acknowledgements

This work was supported by the Natural Science Foundation - Steel and Iron Foundation of Hebei Province of China (No. B2020209022), the Science and Technology Program of Hebei (No. 23372505D), the Hebei Natural Science Foundation (No. H2023209084), the Science and Technology Project of Hebei (No. 252W5202D), and the Central Government Guided Local Science and Technology Development Fund Projects (No. 264Z1407G).

Declaration of competing interest

All the contributing authors report no conflict of interest in this work.

Author contribution statement

Y. Y. H.: Software, writing – original draft, writing – review & editing, visualization. Z. D. Z.: Conceptualization. R. Z. L.: Writing – review & editing. Q. Z.: Writing – review & editing. Z. Y. S.: Writing – review & editing. C. L.: Writing – review & editing. X. Q. W.: Software. R. Y. Z.: Writing – review & editing. Q. D. Z.: Supervision. Y. X. G.: Supervision. L. D. S.: Supervision, funding acquisition. All the authors have approved the final manuscript.

Informed consent

Not applicable.

Ethics statement

Not applicable.

Use of AI statement

None.

References

[1] Wan, Y. J.; Li, R. Y.; Su, J. W.; Yi, W. L.; Li, Y. L.; Chu, H.; Shen, Z. H.; Gao, S.; Hai, X.; Zhong, R. Q. et al. Single-atom supported catalysts and beyond. *Adv. Mater.* **2025**, *37*, 2504518.

[2] Li, Z. S.; Li, B. L.; Li, Q. Y. Single-atom nano-islands (SANIs): A robust atomic-nano system for versatile heterogeneous catalysis applications. *Adv. Mater.* **2023**, *35*, 2211103.

[3] Ye, B. C.; Li, W. H.; Zhang, X.; Chen, J.; Gao, Y.; Wang, D. S.; Pan, H. G. Advancing heterogeneous organic synthesis with coordination chemistry-empowered single-atom catalysts. *Adv. Mater.* **2024**, *36*, 2402747.

[4] Yang, X. F.; Wang, A. Q.; Qiao, B. T.; Li, J.; Liu, J. Y.; Zhang, T. Single-atom catalysts: A new frontier in heterogeneous catalysis. *Acc. Chem. Res.* **2013**, *46*, 1740–1748.

[5] Abazari, A. M.; Safavi, S. M.; Rezazadeh, G.; Villanueva, L. G. Modelling the size effects on the mechanical properties of micro/nano structures. *Sensors* **2015**, *15*, 28543–28562.

[6] Gloag, L.; Somerville, S. V.; Gooding, J. J.; Tilley, R. D. Co-catalytic metal-support interactions in single-atom electrocatalysts. *Nat. Rev. Mater.* **2024**, *9*, 173–189.

[7] Qi, L. L.; Guan, J. Q. Orbital hybridizations in single-atom catalysts for electrocatalysis. *Sci. Bull.* **2025**, *70*, 1856–1871.

[8] Hai, X.; Xi, S. B.; Mitchell, S.; Harrath, K.; Xu, H. M.; Akl, D. F.; Kong, D. B.; Li, J.; Li, Z. J.; Sun, T. et al. Scalable two-step annealing method for preparing ultra-high-density single-atom catalyst libraries. *Nat. Nanotechnol.* **2022**, *17*, 174–181.

[9] Lin, H. W.; Luo, S. Q.; Zhang, H. B.; Ye, J. H. Toward solar-driven carbon recycling. *Joule* **2022**, *6*, 294–314.

[10] Bian, J. J.; Huang, L. M.; Li, Y. M. Effects of particle size and O-contamination of LiF on the phase purity and microwave dielectric properties of $BaLiF_3$ ceramic. *Ceram. Int.* **2024**, *50*, 51877–51880.

[11] Gao, L. Z.; Zhuang, J.; Nie, L.; Zhang, J. B.; Zhang, Y.; Gu, N.; Wang, T. H.; Feng, J.; Yang, D. L.; Perrett, S. et al. Intrinsic peroxidase-like activity of ferromagnetic nanoparticles. *Nat. Nanotechnol.* **2007**, *2*, 577–583.

[12] Wei, H.; Wang, E. K. Nanomaterials with enzyme-like characteristics (nanozymes): Next-generation artificial enzymes. *Chem. Soc. Rev.* **2013**, *42*, 6060–6093.

[13] Jiao, Y. F.; Shang, Y. X.; Li, N.; Ding, B. Q. DNA-based enzymatic systems and their applications. *iScience* **2022**, *25*, 104018.

[14] Ji, S. F.; Jiang, B.; Hao, H. G.; Chen, Y. J.; Dong, J. C.; Mao, Y.; Zhang, Z. D.; Gao, R.; Chen, W. X.; Zhang, R. F. et al. Matching the kinetics of natural enzymes with a single-atom iron nanozyme. *Nat. Catal.* **2021**, *4*, 407–417.

[15] Qiao, B. T.; Wang, A. Q.; Yang, X. F.; Allard, L. F.; Jiang, Z.; Cui, Y. T.; Liu, J. Y.; Li, J.; Zhang, T. Single-atom catalysis of CO oxidation using $Pt1/FeO_x$. *Nat. Chem.* **2011**, *3*, 634–641.

[16] Singh, B.; Gawande, M. B.; Kute, A. D.; Varma, R. S.; Fornasiero, P.; McNeice, P.; Jagadeesh, R. V.; Beller, M.; Zbořil, R. Single-atom (iron-based) catalysts: Synthesis and applications. *Chem. Rev.* **2021**, *121*, 13620–13697.

[17] Li, Z.; Liu, F. N.; Chen, C. X.; Jiang, Y. Y.; Ni, P. J.; Song, N. N.; Hu, Y.; Xi, S. B.; Liang, M. M.; Lu, Y. Z. Regulating the N coordination environment of Co single-atom nanozymes for highly efficient oxidase mimics. *Nano Lett.* **2023**, *23*, 1505–1513.

[18] Goel, H.; Rana, I.; Jain, K.; Ranjan, K. R.; Mishra, V. Atomically dispersed single-atom catalysts (SACs) and enzymes (SAzymes): Synthesis and application in Alzheimer's disease detection. *J. Mater. Chem. B* **2024**, *12*, 10466–10489.

[19] Zeng, Q. D.; Zhong, H. H.; Liao, J. H.; Huo, Q.; Miao, B. P.; Zeng, L.; Zhang, B.; Nie, G. H. Antioxidant activities of metal single-atom nanozymes in biomedicine. *Biomater. Sci.* **2024**, *12*, 5150–5163.

[20] Liang, H. Y.; Xian, Y. J.; Wang, X. J. Preparation and application of single-atom nanozymes in oncology: A review. *Front. Chem.* **2024**, *12*, 1442689.

[21] Han, W.; Wei, P. Y.; Xie, L. L.; Zhu, L. M.; He, B. S.; Cao, X. Y. Heteroatom modulation of nickel single-atom nanozymes for enhanced interfacial catalytic activity in sensitive electrochemical detection of herbicides. *Chem. Engi. J.* **2025**, *505*, 159557.

[22] He, W. Y.; Wu, J. H.; Liu, J. L.; Li, J. Single-atom nanozymes for catalytic therapy: Recent advances and challenges. *Adv. Funct. Mater.* **2024**, *34*, 2312116.

[23] Zhao, J. J.; Li, L.; Li, P. X.; Dai, L. Y.; Dong, J. W.; Zhou, L. Y.; Wang, Y. Z.; Zhang, P. H.; Ji, K. S.; Zhang, Y. K. et al. Realization of 2D metals at the ångström thickness limit. *Nature* **2025**, *639*, 354–359.

[24] Ji, D. L.; Lee, Y.; Nishina, Y.; Kamiya, K.; Daiyan, R.; Chu, D. W.; Wen, X. Y.; Yoshimura, M.; Kumar, P.; Andreeva, D. V. et al. Angstrom-confined electrochemical synthesis of sub-unit-cell non-van der waals 2D metal oxides. *Adv. Mater.* **2023**, *35*, 2301506.

[25] Zhao, H. W.; Zhu, Y. J.; Li, F. S.; Hao, R.; Wang, S. X.; Guo, L. A generalized strategy for the synthesis of large-size ultrathin two-dimensional metal oxide nanosheets. *Angew. Chem., Int. Ed.* **2017**, *56*, 8766–8770.

[26] Yue, M.; Zhang, K. N.; Zhao, M.; Wang, Y. N.; Li, D.; Liang, J. Y.; Zheng, B. Y.; Zou, C.; Ye, Y.; Wang, P. J. et al. 2D Cd metal contacts via low-temperature van der Waals epitaxy towards high-performance 2D transistors. *Nat. Commun.* **2025**, *16*, 4018.

[27] Zhao, L. P.; Wang, B. Q.; Wang, R. A critical review on new and efficient 2D materials for catalysis. *Adv. Mater. Interfaces* **2022**, *9*, 2200771.

[28] Sarmah, H. J.; Mohanta, D. Revisiting principles, practices and scope of technologically relevant 2D materials. *J. Mater. Res.* **2021**, *36*, 1961–1979.

[29] Hamm, J. M.; Hess, O. Two two-dimensional materials are better than one. *Science* **2013**, *340*, 1298–1299.

[30] Leng, X. Y.; Chen, S. Y.; Yang, K.; Chen, M. S.; Shaker, M.; Vdovin, E. E.; Ge, Q.; Novoselov, K. S.; Andreeva, D. V. Introduction to two-dimensional materials. *Surf. Rev. Lett.* **2021**, *28*, 2140005.

[31] Marian, M.; Berman, D.; Nečas, D.; Emami, N.; Ruggiero, A.; Rosenkranz, A. Roadmap for 2D materials in biotribological/biomedical applications-a review. *Adv. Colloid Interface Scie.* **2022**, *307*, 102747.

[32] Tan, C. L.; Cao, X. H.; Wu, X. J.; He, Q. Y.; Yang, J.; Zhang, X.; Chen, J. Z.; Zhao, W.; Han, S. K.; Nam, G. H. et al. Recent advances in ultrathin two-dimensional nanomaterials. *Chem. Rev.* **2017**, *117*, 6225–6331.

[33] Novoselov, K. S.; Geim, A. K.; Morozov, S. V.; Jiang, D.; Zhang, Y.; Dubonos, S. V.; Grigorieva, I. V.; Firsov, A. A. Electric field effect in atomically thin carbon films. *Science* **2004**, *306*, 666–669.

[34] Huang, X. Q.; Tang, S. H.; Mu, X. L.; Dai, Y.; Chen, G. X.; Zhou, Z. Y.; Ruan, F. X.; Yang, Z. L.; Zheng, N. F. Freestanding palladium nanosheets with plasmonic and catalytic properties. *Nat. Nanotechnol.* **2011**, *6*, 28–32.

[35] Ma, R. Z.; Sasaki, T. Two-dimensional oxide and hydroxide nanosheets: Controllable high-quality exfoliation, molecular assembly, and exploration of functionality. *Acc. Chem. Res.* **2015**, *48*, 136–143.

[36] Wang, Q.; O'Hare, D. Recent advances in the synthesis and application of layered double hydroxide (LDH) nanosheets. *Chem. Rev.* **2012**, *112*, 4124–4155.

[37] Jin, H. Y.; Gu, Q. F.; Chen, B.; Tang, C.; Zheng, Y.; Zhang, H.; Jaroniec, M.; Qiao, S. Z. Molten salt-directed catalytic synthesis of 2D layered transition-metal nitrides for efficient hydrogen evolution. *Chem* **2020**, *6*, 2382–2394.

[38] Hu, Z. M.; Xiao, X.; Jin, H. Y.; Li, T. Q.; Chen, M.; Liang, Z.; Guo, Z. F.; Li, J.; Wan, J.; Huang, L. et al. Rapid mass production of two-dimensional metal oxides and hydroxides via the molten salts method. *Nat. Commun.* **2017**, *8*, 15630.

[39] Xiao, X.; Yu, H. M.; Jin, H. Y.; Wu, M. H.; Fang, Y. S.; Sun, J. Y.; Hu, Z. M.; Li, T. Q.; Wu, J. B.; Huang, L. et al. Salt-templated synthesis of 2D metallic MoN and other nitrides. *ACS Nano* **2017**, *11*, 2180–2186.

[40] Jin, H. Y.; Yu, H. M.; Li, H. B.; Davey, K.; Song, T.; Paik, U.; Qiao, S. Z. MXene analogue: A 2D nitridene solid solution for high-rate hydrogen production. *Angew. Chem., Int. Ed.* **2022**, *61*, e202203850.

[41] Jin, H. Y.; Liu, X.; Vasileff, A.; Jiao, Y.; Zhao, Y. Q.; Zheng, Y.; Qiao, S. Z. Single-crystal nitrogen-rich two-dimensional Mo_5N_6 nanosheets for efficient and stable seawater splitting. *ACS Nano* **2018**, *12*, 12761–12769.

[42] Liu, W. G.; Hu, W. J.; Yang, L. J.; Liu, J. Single cobalt atom anchored on carbon nitride with well-defined active sites for photo-enzyme catalysis. *Nano Energy* **2020**, *73*, 104750.

[43] Wang, X. Y.; Hu, W. C.; Xia, X. H.; Wang, C. Implanting of single zinc sites into 2D metal-organic framework nanozymes for boosted antibiofilm therapy. *Adv. Funct. Mater.* **2023**, *33*, 2212798.

[44] The rise and rise of graphene. *Nat. Nanotechnol.* **2010**, *5*, 755–755

[45] Novoselov, K. S.; Geim, A. K.; Morozov, S. V.; Jiang, D.; Katsnelson, M. I.; Grigorieva, I. V.; Dubonos, S. V.; Firsov, A. A. Two-dimensional gas of massless Dirac fermions in graphene. *Nature* **2005**, *438*, 197–200.

[46] Kane, R.; Ma, P. X. Mimicking the nanostructure of bone matrix to regenerate bone. *Mater. Today* **2013**, *16*, 418–423.

[47] Jiang, H. N.; Yang, W. W.; Xu, M. Q.; Wang, E. Q.; Wei, Y.; Liu, W.; Gu, X. K.; Liu, L. X.; Chen, Q.; Zhai, P. B. et al. Single atom catalysts in van der Waals gaps. *Nat. Commun.* **2022**, *13*, 6863.

[48] Zou, J. X.; Bao, L. S.; Sun, Q. F.; Bao, C. G.; Chen, H.; Liu, H. B. Oxygen reduction reaction catalysts for zinc-air batteries featuring single cobalt atoms in a nitrogen-doped 3D-interconnected porous graphene framework. *Small* **2025**, *21*, 2409506.

[49] Li, R. J.; Li, H. X.; Zhang, X. D.; Liu, B. W.; Wu, B. L.; Zhu, B. C.; Yu, J. G.; Liu, G.; Zheng, L. R.; Zeng, Q. D. S-scheme g-C_3N_4/CdS heterostructures grafting single Pd atoms for ultrafast charge transport and efficient visible-light-driven H_2 evolution. *Adv. Funct. Mater.* **2024**, *34*, 2402797.

[50] Zhang, B.; Fan, T.; Xie, N.; Nie, G.; Zhang, H. Versatile applications of metal single-atom @ 2D material nanoplatforms. *Adv. Sci.* **2019**, *6*, 1901787.

[51] Chen, J. X.; Ma, Q.; Li, M. H.; Chao, D. Y.; Huang, L.; Wu, W. W.; Fang, Y. X.; Dong, S. J. Glucose-oxidase like catalytic mechanism of noble metal nanozymes. *Nat. Commun.* **2021**, *12*, 3375.

[52] Mu, X. Q.; Liu, S. L.; Zhang, M. Y.; Zhuang, Z. C.; Chen, D.; Liao, Y. R.; Zhao, H. Y.; Mu, S. C.; Wang, D. S.; Dai, Z. H. Symmetry-broken Ru nanoparticles with parasitic Ru–Co dual-single atoms overcome the volmer step of alkaline hydrogen oxidation. *Angew. Chem., Int. Ed.* **2024**, *63*, e202319618.

[53] Chen, X. H.; Zhu, C. X.; Xu, Y.; Wang, K. Y.; Cao, X. W.; Shen, Y. F.; Liu, S. Q.; Zhang, Y. J. Quantitative evaluation of O_2 activation half-reaction for Fe–N–C in oxidase-like activity enhancement. *Catal. Sci. Technol.* **2021**, *11*, 7255–7259.

[54] Bu, Z. J.; Liu, J. J.; Tang, Z.; Liang, H.; Bai, Q. Q.; Liu, S. Q.; Niu, X. H. Unusual oxidase-mimetic catalytic performance surpassing peroxidase in amorphous CoO_x: Underlying mechanism and toward a novel H_2O_2-related detection paradigm. *Chem. Commun.* **2025**, *61*, 7672–7675.

[55] Li, S. F.; Wang, F. F.; Wang, C. H.; Hao, L.; Shang, N. Z.; Zhang, P. B.; Zhang, Y. W.; Xiao, N.; Kang, Y. A.; Liu, J. et al. B doped Zn single-atom nanozyme with enhanced oxidase-like activity combined CRISPR/Cas13a system for RNA sensing. *Adv. Funct. Mater.* **2025**, *35*, 2418523.

[56] Li, Y. D.; Sun, Y. J.; Wang, Q. Y.; Zhuang, Z. C.; Ma, Z. T.; Liu, L. M.; Wang, G. M.; Wang, D. S.; Zheng, X. S. Synergy of photogenerated electrons and holes toward efficient photocatalytic urea synthesis from CO_2 and N_2. *Angew. Chem., Int. Ed.* **2024**, *63*, e202405637.

[57] Yang, H. C.; Duan, P. F.; Zhuang, Z. C.; Luo, Y. W.; Shen, J.; Xiong, Y. L.; Liu, X. W.; Wang, D. S. Understanding the dynamic evolution of active sites among single atoms, clusters, and nanoparticles. *Adv. Mater.* **2025**, *37*, 2415265.

[58] Wang, Y. X.; Cui, X. Z.; Zhang, J. Q.; Qiao, J. L.; Huang, H. T.; Shi, J. L.; Wang, G. X. Advances of atomically dispersed catalysts from single-atom to clusters in energy storage and conversion applications. *Prog. Mater. Sci.* **2022**, *128*, 100964.

[59] Park, J. W.; Park, G.; Kim, M.; Han, M. S.; Jang, J.; Yamauchi, Y.; Yuliarto, B.; Krüger, P.; Kim, J.; Park, N. et al. Ni-single atom decorated mesoporous carbon electrocatalysts for hydrogen evolution reaction. *Chem. Eng. J.* **2023**, *468*, 143733.

[60] Yang, Y.; Zhang, W. J.; Wu, G. C.; Huang, Q.; Wen, J. H.; Wang, D. S.; Liu, M. Y. Electronic structure tuning in Cu–Co dual single atom catalysts for enhanced COOH* spillover and electrocalytic CO_2 reduction activity. *Angew. Chem., Int. Ed.* **2025**, *64*, e202504423.

[61] Lien, H. T.; Chang, S. T.; Chen, P. T.; Wong, D. P.; Chang, Y. C.; Lu, Y. R.; Dong, C. L.; Wang, C. H.; Chen, K. H.; Chen, L. C. Probing the active site in single-atom oxygen reduction catalysts via operando X-ray and electrochemical spectroscopy. *Nat. Commun.* **2020**, *11*, 4233.

[62] Chen, S. H.; Zheng, X. B.; Zhu, P.; Li, Y. P.; Zhuang, Z. C.; Wu, H. J.; Zhu, J. X.; Xiao, C. H.; Chen, M. Z.; Wang, P. S. et al. Copper atom pairs stabilize *OCCO dipole toward highly selective CO_2 electroreduction to C_2H_4. *Angew. Chem., Int. Ed.* **2024**, *63*, e202411591.

[63] Wu, J. M.; Shi, H. N.; Li, K. Y.; Guo, X. W. Advances and challenges of single-atom catalysts in environmental catalysis. *Curr. Opin. Chem. Eng.* **2023**, *40*, 100923.

[64] Ma, F. Y.; Zhang, P. F.; Zheng, X. B.; Chen, L.; Li, Y. R.; Zhuang, Z. C.; Fan, Y. M.; Jiang, P.; Zhao, H.; Zhang, J. W. et al. Steering the site distance of atomic Cu−Cu pairs by first-shell halogen coordination boosts CO_2-to-C_2 selectivity. *Angew. Chem., Int. Ed.* **2024**, *63*, e202412785.

[65] Zhu, Y. X.; Lei, L. L.; Zhang, Z. Q.; Chen, Z. X.; Lin, H.; Shi, J. L. Two-dimensional nanomaterials for inflammation-related disease treatments. *Innov. Mater.* **2025**, *3*, 100128.

[66] Zhang, P. P.; Zhao, F. L.; Long, P.; Wang, Y.; Yue, Y. C.; Liu, X. Y.; Feng, Y. Y.; Li, R. J.; Hu, W. P.; Li, Y. et al. Sonication-assisted liquid-phase exfoliated α-GeTe: A two-dimensional material with high Fe^{3+} sensitivity. *Nanoscale* **2018**, *10*, 15989–15997.

[67] Shen, J. F.; He, Y. M.; Wu, J. J.; Gao, C. T.; Keyshar, K.; Zhang, X.; Yang, Y. C.; Ye, M. X.; Vajtai, R.; Lou, J. et al. Liquid phase exfoliation of two-dimensional materials by directly probing and matching surface tension components. *Nano Lett.* **2015**, *15*, 5449–5454.

[68] Eng, A. Y. S.; Ambrosi, A.; Sofer, Z.; Šimek, P.; Pumera, M. Electrochemistry of transition metal dichalcogenides: Strong dependence on the metal-to-chalcogen composition and exfoliation method. *ACS Nano* **2014**, *8*, 12185–12198.

[69] Ambrosi, A.; Sofer, Z.; Pumera, M. Electrochemical exfoliation of layered black phosphorus into phosphorene. *Angew. Chem., Int. Ed.* **2017**, *56*, 10443–10445.

[70] Gao, E. L.; Lin, S. Z.; Qin, Z.; Buehler, M. J.; Feng, X. Q.; Xu, Z. P. Mechanical exfoliation of two-dimensional materials. *J. Mech. Phys. Solids* **2018**, *115*, 248–262.

[71] Gao, Y.; Yang, C. D.; Sun, F. L.; He, D. P.; Wang, X. Q.; Chen, J.; Zheng, X. B.; Liu, R. C.; Pan, H. G.; Wang, D. S. Ligand-tuning metallic sites in molecular complexes for efficient water oxidation. *Angew. Chem., Int. Ed.* **2025**, *64*, e202415755.

[72] Shen, J.; Chen, J.; Qian, Y. P.; Wang, X. Q.; Wang, D. S.; Pan, H. G.; Wang, Y. G. Atomic engineering of single-atom nanozymes for biomedical applications. *Adv. Mater.* **2024**, *36*, 2313406.

[73] Wang, Y. D.; Zulpya, M.; Zhang, X. Y.; Xu, S. H.; Sun, J.; Dong, B. Recent advances of metal-organic frameworks-based nanozymes for bio-applications. *Chem. Res. Chin. Univ.* **2022**, *38*, 1324–1343.

[74] Chen, L. L.; Yang, K.; Wang, C.; Han, D.; Wen, J. Next-generation of a Fe–Ce double variable-valence metals modulated high-efficiency nanozyme. *Chem. Eng. J.* **2024**, *495*, 153314.

[75] Yuan, Y.; Chen, B.; An, X. X.; Guo, Z. H.; Liu, X.; Lu, H.; Hu, F. X.; Chen, Z. G.; Guo, C. X.; Li, C. M. MOFs-based magnetic nanozyme to boost cascade ROS accumulation for augmented tumor ferroptosis. *Adv. Healthc. Mater.* **2024**, *13*, 2304591.

[76] Wang, X. Q.; Zhang, X. Y.; Jiao, M. G.; Ma, R. L.; Xie, F.; Wan, H.; Shen, X. J.; Zhang, L. L.; Ma, W.; Zhou, Z. The strong Pt–N_3O coordination in graphene nanosheets accelerates the $4e^-$ electrocatalytic oxygen reduction process. *Chin. J. Catal.* **2025**, *77*, 227–235.

[77] Zhang, X. D.; Chen, X. K.; Zhao, Y. L. Nanozymes: Versatile platforms for cancer diagnosis and therapy. *Nano-Micro Lett.* **2022**, *14*, 95.

[78] Zhu, P. A.; Liu, S.; Feng, L. J.; Zhang, X. F. Redox-mediated dsDNA-dye photooxidase mimic enable catalytic oxidation of 3, 3′, 5, 5′-tetramethylbenzidine by dissolved O_2 at neutral pH for improved biosensing. *Biosens. Bioelectron.* **2025**, *268*, 116865.

[79] Ma, R. Z.; Zhang, J.; Gong, J. X.; Lin, Y. X.; Zhang, J. L.; Huang, Z. Q.; Chang, C. R.; Liu, S. J.; Zhu, W.; Wang, Y. X. et al. The cooperative effects of the Rh-M dual-metal atomic pairs in formic acid oxidation. *Angew. Chem., Int. Ed.* **2025**, *64*, e202503095.

[80] Jiao, J. J.; Yang, H.; Zhou, X. M.; Huang, K. K.; Zhang, X.; Yang, H.; Gong, W.; Yang, S. P. Ultrathin 2D Cu-porphyrin MOF

nanosheet loaded Fe_3O_4 nanoparticles As a multifunctional nanoplatform for synergetic chemodynamic and photodynamic therapy independent of O_2. *ACS Appl. Mater. Interfaces* **2025**, *17*, 7438–7448.

[81] Alvarenga, G. M.; Villullas, H. M. Transition metal oxides in the electrocatalytic oxidation of methanol and ethanol on noble metal nanoparticles. *Curr. Opin. Electrochem.* **2017**, *4*, 39–44.

[82] Lv, L. Y.; Tan, H.; Kong, Y.; Tang, B.; Ji, Q. Q.; Liu, Y. Y.; Wang, C.; Zhuang, Z. C.; Wang, H. J.; Ge, M. et al. Breaking the scaling relationship in C−N coupling via the doping effects for efficient urea electrosynthesis. *Angew. Chem., Int. Ed.* **2024**, *63*, e202401943.

[83] Tang, M. H.; Shen, J.; Zhang, F. T.; Zhao, Y. F.; Gan, T.; Zeng, W.; Li, R. X.; Wang, D. S.; Han, B. X.; Liu, Z. M. Upcycling of polyamide wastes to tertiary amines using Mo single atoms and Rh nanoparticles. *Angew. Chem., Int. Ed.* **2025**, *64*, e202416436.

[84] Wei, X. Q.; Song, S. J.; Song, W. Y.; Wen, Y. T.; Xu, W. Q.; Chen, Y. F.; Wu, Z. C.; Qin, Y.; Jiao, L.; Wu, Y. et al. Tuning iron spin states in single-atom nanozymes enables efficient peroxidase mimicking. *Chem. Sci.* **2022**, *13*, 13574–13581.

[85] Guan, S. Y.; Yuan, Z. L.; Zhuang, Z. C.; Zhang, H. H.; Wen, H.; Fan, Y. P.; Li, B. J.; Wang, D. S.; Liu, B. Z. Why do single-atom alloys catalysts outperform both single-atom catalysts and nanocatalysts on MXene. *Angew. Chem., Int. Ed.* **2024**, *63*, e202316550.

[86] Liao, J. Y.; Pang, S. Y.; Hao, J. H. Multi-scale interface engineering of MXenes for multifunctional sensory systems. *Adv. Funct. Mater.* **2026**, *36*, e00047.

[87] Zou, Y. D.; Zhang, Y. D.; Zhang, J.; He, P.; Fan, Z. Y.; He, N. N.; Li, X. Z.; Li, Y.; Ma, L. J. Cooperative steric modulation of flexibility, disorder, and pore size in two-dimensional covalent organic framework membranes for enhanced selective ion sieving. *J. Am. Chem. Soc.* **2025**, *147*, 32580–32590.

[88] Pei, S. F.; Wei, Q. W.; Huang, K.; Cheng, H. M.; Ren, W. C. Green synthesis of graphene oxide by seconds timescale water electrolytic oxidation. *Nat. Commun.* **2018**, *9*, 145.

[89] Liu, L. L.; Chen, J.; Zhang, Y.; Yu, C. X.; Du, W.; Sun, X. Q.; Zhang, J. L.; Hu, F. L.; Mi, Y.; Ma, L. F. Fabrication of ultrathin single-layer 2D metal-organic framework nanosheets with excellent adsorption performance via a facile exfoliation approach. *J. Mater. Chem. A* **2021**, *9*, 546–555.

[90] Zhou, Y. N.; Yan, P. F.; Zhang, S. Y.; Zhang, Y. X.; Chang, H. W.; Zheng, X. L.; Jiang, J. Y.; Xu, Q. CO_2 coordination-driven top-down synthesis of a 2D non-layered metal-organic framework. *Fund. Res.* **2022**, *2*, 674–681.

[91] Nam, D. H.; Bushuyev, O. S.; Li, J.; De Luna, P.; Seifitokaldani, A.; Dinh, C. T.; García De Arquer, F. P.; Wang, Y. H.; Liang, Z. Q.; Proppe, A. H. et al. Metal-organic frameworks mediate Cu coordination for selective CO_2 electroreduction. *J. Am. Chem. Soc.* **2018**, *140*, 11378–11386.

[92] Zhuo, B. L.; Tan, A. D.; Xiang, Z. P.; Piao, J. H.; Zheng, W. H.; Wan, K.; Liang, Z. X.; Fu, Z. Y. Ozonolysis-oxidation-driven top-down strategy for the target preparation of ultrathin 2D metal-organic framework monolayers. *Ind. Chem. Mater.* **2024**, *2*, 110–117.

[93] Choi, E. Y.; Park, K.; Yang, C. M.; Kim, H.; Son, J. H.; Lee, S. W.; Lee, Y. H.; Min, D.; Kwon, Y. U. Benzene-templated hydrothermal synthesis of metal-organic frameworks with selective sorption properties. *Chem. -Eur. J.* **2004**, *10*, 5535–5540.

[94] Zhang, X. K.; Yuan, S. W.; Li, Y. Q.; Wang, Z. Y.; Feng, W. R. Efficient and green strategy of ultrasound-assisted liquid-phase exfoliation of MoS_2 nanosheets. *Langmuir* **2025**, *41*, 15788–15795.

[95] Jawaid, A.; Che, J.; Drummy, L. F.; Bultman, J.; Waite, A.; Hsiao, M. S.; Vaia, R. A. Redox exfoliation of layered transition metal dichalcogenides. *ACS Nano* **2017**, *11*, 635–646.

[96] Li, Q. H.; Liu, S. J.; Liu, J. C.; Li, Z.; Li, Y. D. Recycling sulfur-poisoned Pd catalysts via thermal atomization for semi-hydrogenation of acetylene. *J. Am. Chem. Soc.* **2025**, *147*, 5615–5623.

[97] Tian, L.; Gao, X. P.; Wang, S. C.; Chen, C.; Chen, M.; Guo, W. X.; Wang, Z.; Tai, X. L.; Han, X.; Xu, C. X. et al. Precise arrangement of metal atoms at the interface by a thermal printing strategy. *Proc. Natl. Acad. Sci. USA* **2023**, *120*, e2310916120.

[98] Li, R.; Yan, X. Y.; Liu, M.; Zhao, Q. K.; Du, J.; Tan, X. X.; Ba, J. W.; Zeng, R. G.; Luo, W. H.; Xu, J. S. Cathodic corrosion as a facile and universal method for scalable preparation of powdery single atom electrocatalysts. *Nano Res.* **2024**, *17*, 4943–4950.

[99] Li, R.; Xu, J. S.; Zhao, Q. K.; Ren, W. S.; Zeng, R. G.; Pan, Q. F.; Yan, X. Y.; Ba, J. W.; Tang, T.; Luo, W. H. Cathodic corrosion as a facile and universal method for the preparation of supported metal single atoms. *Nano Res.* **2022**, *15*, 1838–1844.

[100] Poerwoprajitno, A. R.; Gloag, L.; Watt, J.; Cheong, S.; Tan, X.; Lei, H.; Tahini, H. A.; Henson, A.; Subhash, B.; Bedford, N. M. et al. A single-Pt-atom-on-Ru-nanoparticle electrocatalyst for CO-resilient methanol oxidation. *Nat. Catal.* **2022**, *5*, 231–237.

[101] Li, Y. P.; Niu, S. W.; Liu, P. G.; Pan, R. R.; Zhang, H. K.; Ahmad, N.; Shi, Y.; Liang, X.; Cheng, M. Y.; Chen, S. H. et al. Ruthenium nanoclusters and single atoms on α-MoC/N-doped carbon achieves low-input/input-free hydrogen evolution via decoupled/coupled hydrazine oxidation. *Angew. Chem., Int. Ed.* **2024**, *63*, e202316755.

[102] Zhao, J.; Zhang, Y. X.; Zhuang, Z. C.; Deng, Y. T.; Gao, G.; Li, J. Y.; Meng, A. L.; Li, G. C.; Wang, L.; Li, Z. J. et al. Tailoring d-p orbital hybridization to decipher the essential effects of heteroatom substitution on redox kinetics. *Angew. Chem., Int. Ed.* **2024**, *63*, e202404968.

[103] Zhang, J. C.; Bai, Q.; Bi, X. L.; Zhang, C. H.; Shi, M. Y.; Yu, W. W.; Du, F. L.; Wang, L. N.; Wang, Z. B.; Zhu, Z. L. et al. Piezoelectric enhanced peroxidase-like activity of metal-free sulfur doped graphdiyne nanosheets for efficient water pollutant degradation and bacterial disinfection. *Nano Today* **2022**, *43*, 101429.

[104] Zhang, C.; Li, Q. R.; Shan, J.; Xing, J. H.; Liu, X. Y.; Ma, Y.; Qian, H. S.; Chen, X. L.; Wang, X. W.; Wu, L. M. et al. Multifunctional two-dimensional Bi_2Se_3 nanodiscs for anti-inflammatory therapy of inflammatory bowel diseases. *Acta Biomater.* **2023**, *160*, 252–264.

[105] Wu, J. H.; Lv, W. X.; Yang, Q. T.; Li, H. Y.; Li, F. Label-free homogeneous electrochemical detection of MicroRNA based on target-induced anti-shielding against the catalytic activity of two-dimension nanozyme. *Biosens. Bioelectron.* **2021**, *171*, 112707.

[106] Wu, F.; Wang, Y. R.; Li, Y. F.; Shi, L. Q.; Yuan, L.; Ren, Y. J.; Van Der Mei, H. C.; Liu, Y. Single-atom Cu anchored on carbon nitride as a bifunctional glucose oxidase and peroxidase nanozyme for antibacterial therapy. *ACS Nano* **2025**, *19*, 10816–10828.

[107] Duan, X. D.; Wang, C.; Shaw, J. C.; Cheng, R.; Chen, Y.; Li, H. L.; Wu, X. P.; Tang, Y.; Zhang, Q. L.; Pan, A. L. et al. Lateral epitaxial growth of two-dimensional layered semiconductor heterojunctions. *Nat. Nanotechnol.* **2014**, *9*, 1024–1030.

[108] Pei, J. Y.; Yang, F.; Zhao, H. Y. Plasma-induced enhancement of light-matter interaction on graphene-MoS_2 heterostructure for sensitive SERS sensing. *Nano Res.* **2025**, *18*, 94907376.

[109] Yang, J. R.; Zhu, C. X.; Wang, D. S. A simple organo-electrocatalysis system for the chlor-related industry. *Angew. Chem., Int. Ed.* **2024**, *63*, e202406883.

[110] Chang, W.; Qi, B.; Wang, R. Y.; Liu, H. J.; Chen, G. B.; Hu, G. C.; Li, Z. X.; Sun, J.; Peng, Y. K.; Li, G. C. et al. Atomically dispersed gold nanoclusters and single atoms coexisting chiral electrode for high-performance enantioselective electrosynthesis using H_2O as hydrogen source. *Adv. Funct. Mater.* **2024**, *34*, 2315675.

[111] Chang, J. W.; Jing, W.; Yong, X.; Cao, A.; Yu, J. K.; Wu, H.; Wan, C. Z.; Wang, S. Y.; Waterhouse, G. I. N.; Yang, B. et al. Synthesis of ultrahigh-metal-density single-atom catalysts via metal sulfide-mediated atomic trapping. *Nat. Synth.* **2024**, *3*, 1427–1438.

[112] Jiang, D.; Wan, G.; Halldin Stenlid, J.; García-Vargas, C. E.; Zhang,

J. H.; Sun, C. J.; Li, J. R.; Abild-Pedersen, F.; Tassone, C. J.; Wang, Y. Dynamic and reversible transformations of subnanometre-sized palladium on ceria for efficient methane removal. *Nat. Catal.* **2023**, *6*, 618–627.

[113] Tao, Y.; Guan, J. P.; Zhang, J.; Hu, S. Y.; Ma, R. Z.; Zheng, H. R.; Gong, J. X.; Zhuang, Z. C.; Liu, S. J.; Ou, H. H. et al. Ruthenium single atomic sites surrounding the support pit with exceptional photocatalytic activity. *Angew. Chem., Int. Ed.* **2024**, *63*, e202400625.

[114] Liu, G. Q.; Zhang, H.; Wang, P. F.; Gao, C.; Zhuang, Z. C.; Wang, D. S.; Zhan, S. H. Atomic-level design of acid-base pairs in oxides for selective catalytic reduction of nitrogen oxides with ammonia. *Angew. Chem., Int. Ed.* **2025**, *64*, e202509362.

[115] Jiang, Y. J.; Chen, Z. B.; Sui, N.; Zhu, Z. L. Data-driven evolutionary design of multienzyme-like nanozymes. *J. Am. Chem. Soc.* **2024**, *146*, 7565–7574.

[116] Chen, Z.; Yu, Y. X.; Gao, Y. H.; Zhu, Z. L. Rational design strategies for nanozymes. *ACS Nano* **2023**, *17*, 13062–13080.

[117] Liu, H.; Chen, Y. H.; Huang, Y. P.; Wei, L.; Ran, J. J.; Li, Q. W.; Tian, Y. R.; Luo, Z. L.; Yang, L. Y.; Liu, H. J. et al. Macrophage-derived mir-100-5p orchestrates synovial proliferation and inflammation in rheumatoid arthritis through mTOR signaling. *J. Nanobiotechnol.* **2024**, *22*, 197.

[118] Li, W.; Liu, C.; Gu, C. K.; Choi, J. H.; Wang, S.; Jiang, J. Interlayer charge transfer regulates single-atom catalytic activity on electride/graphene 2D heterojunctions. *J. Am. Chem. Soc.* **2023**, *145*, 4774–4783.

[119] Wei, S. J.; Sun, M. M.; Huang, J.; Chen, Z. B.; Wang, X. J.; Gao, L. Z.; Zhang, J. J. Axial chlorination engineering of single-atom nanozyme: Fe–N_4Cl catalytic sites for efficient peroxidase-mimicking. *J. Am. Chem. Soc.* **2024**, *146*, 33239–33248.

[120] Sun, Q. J.; Wu, M.; Niu, N.; Chen, L. G.; Liu, S.; Yu, J.; Wu, X. Z.; Bai, F. Q.; Yang, P. P. Regulating second coordination shell of Ce atom site and reshaping of carrier enable single-atom nanozyme to efficiently express oxidase-like activity. *Nano Lett.* **2024**, *24*, 8071–8079.

[121] Li, H. Y.; Zhang, Y. Y.; Zhao, Q.; Xu, R. S.; Yang, J.; Deng, K. Q.; Huang, H. W. Bioinspired protein-mineralized single-atom nanozymes for tumor-specific cascade therapy via self-amplifying catalytic synergy. *Small* **2025**, *21*, 2500846.

[122] Tang, B.; Ji, Q. Q.; Zhang, X. L.; Shi, R. C.; Ma, J.; Zhuang, Z. C.; Sun, M.; Wang, H. J.; Liu, R. Q.; Liu, H. J. et al. Symmetry breaking of FeN_4 moiety via edge defects for acidic oxygen reduction reaction. *Angew. Chem., Int. Ed.* **2025**, *64*, e202424135.

[123] Shen, J.; Tang, M. H.; Shi, Z. H.; Guan, S. Y.; Shi, Y. J.; Zhuang, Z. C.; Li, R. Z.; Yang, J. R.; He, D. P.; Liu, B. Z. et al. Efficient generation of negative hydrogen with bimetallic-ternary-structured catalysts for nitrobenzene hydrogenation. *Angew. Chem., Int. Ed.* **2025**, *64*, e202423626.

[124] Wang, X. Y.; Wei, W. J.; Zhou, S. Y.; Pan, Y. Z.; Yang, J. R.; Gan, T.; Zhuang, Z. C.; Li, W. H.; Zhang, X.; Pan, Y. M. et al. Phosphorus-doped single atom copper catalyst as a redox mediator in the cathodic reduction of quinazolinones. *Angew. Chem., Int. Ed.* **2025**, *64*, e202505085.

[125] Zhang, X. L.; Tao, C. Y.; Chu, S. S.; Liu, W. D.; Xia, M. Y.; Jiang, Y. Y.; Lu, Y. Z. Single cobalt sites on defective carbon nanosheets as efficient oxidase mimics for visual biosensing. *Nano Res.* **2025**, *18*, 94907336.

[126] Lu, J. J.; Yao, K. Q.; Xu, X. X.; Ou, J. Z.; Wang, Q. The construction of p-n heterojunction in nanozyme for improved peroxidase-like activity and "point-of-use" water disinfection. *Chem. Eng. J.* **2025**, *510*, 161757.

[127] Qiu, W. B.; Qin, S. M.; Li, Y. B.; Cao, N.; Cui, W. R.; Zhang, Z. D.; Zhuang, Z. C.; Wang, D. S.; Zhang, Y. Overcoming electrostatic interaction via pulsed electroreduction for boosting the electrocatalytic urea synthesis. *Angew. Chem., Int. Ed.* **2024**, *63*, e202402684.

[128] Sun, Q. J.; Xu, X. Y.; Liu, S.; Wu, X. Z.; Yin, C. H.; Wu, M.; Chen, Y. X.; Niu, N.; Chen, L. G.; Bai, F. Q. Mo single-atom nanozyme anchored to the 2D N-doped carbon film: Catalytic mechanism, visual monitoring of choline, and evaluation of intracellular ROS generation. *ACS Appl. Mater. Interfaces* **2023**, *15*, 36124–36134.

[129] Wu, Q. S.; Zheng, G. A.; Li, L. H.; Wang, L. Enhancing peroxidase-like activity and photothermal property of copper single-atom nanozyme via a cascade competition strategy. *Adv. Funct. Mater.* **2025**, *35*, 2422588.

[130] Xu, Y. X.; Li, P. P.; Hu, X. J.; Chen, H. Y.; Tang, Y.; Zhu, Y.; Zhu, X. H.; Zhang, Y. Y.; Liu, M. L.; Yao, S. Z. Polyoxometalate nanostructures decorated with CuO nanoparticles for sensing ascorbic acid and Fe^{2+} ions. *ACS Appl. Nano Mater.* **2021**, *4*, 8302–8313.

[131] Lu, M. J.; Wang, J. L.; Ren, G. Y.; Qin, F. J.; Zhao, Z. Q.; Li, K.; Chen, W. X.; Lin, Y. Q. Superoxide-like Cu/GO single-atom catalysts nanozyme with high specificity and activity for removing superoxide free radicals. *Nano Res.* **2022**, *15*, 8804–8809.

[132] Zhao, H. Q.; Zhang, R. F.; Yan, X. Y.; Fan, K. L. Superoxide dismutase nanozymes: An emerging star for anti-oxidation. *J. Mater. Chem. B* **2021**, *9*, 6939–6957.

[133] Liu, Y.; Liu, Y.; Shi, P. M.; Hu, X. P.; Fan, X. W.; Wu, Y. L.; Pan, J. P.; Bai, Q.; Li, Q. Single-atom nanozyme liposome-integrated microneedles for *in situ* drug delivery and anti-inflammatory therapy in Parkinson's disease. *J. Nanobiotechnol.* **2024**, *22*, 643.

[134] Brigelius-Flohé, R.; Maiorino, M. Glutathione peroxidases. *Biochim. Biophys. Acta (BBA) - Gen. Subjects* **2013**, *1830*, 3289–3303.

[135] Lei, X. G.; Evenson, J. K.; Thompson, K. M.; Sunde, R. A. Glutathione peroxidase and phospholipid hydroperoxide glutathione peroxidase are differentially regulated in rats by dietary selenium. *J. Nutr.* **1995**, *125*, 1438–1446.

[136] Seufferheld, M.; Vieira, M. C. F.; Ruiz, F. A.; Rodrigues, C. O.; Moreno, S. N. J.; Docampo, R. Identification of organelles in bacteria similar to acidocalcisomes of unicellular eukaryotes. *J. Biol. Chem.* **2003**, *278*, 29971–29978.

[137] Xu, C. X.; Sun, S. G.; Johnson, T.; Qi, R.; Zhang, S. Y.; Zhang, J.; Yang, K. The glutathione peroxidase Gpx4 prevents lipid peroxidation and ferroptosis to sustain Treg cell activation and suppression of antitumor immunity. *Cell Rep.* **2021**, *35*, 109235.

[138] Carmagnol, F.; Sinet, P. M.; Jerome, H. Selenium-dependent and non-selenium-dependent glutathione peroxidases in human tissue extracts. *Biochim. Biophys. Acta (BBA) - Gen. Subjects* **1983**, *759*, 49–57.

[139] Lapenna, D. Glutathione and glutathione-dependent enzymes: From biochemistry to gerontology and successful aging. *Ageing Res. Rev.* **2023**, *92*, 102066.

[140] Zhang, L.; Dong, Q.; Hao, Y. M.; Wang, Z. H.; Dong, W. J.; Liu, Y.; Dong, Y. P.; Wu, H. P.; Shuang, S. M.; Dong, C. et al. Drug-primed self-assembly of platinum-single-atom nanozyme to regulate cellular redox homeostasis against cancer. *Adv. Sci.* **2023**, *10*, 2302703.

[141] Jeong, H.; Shin, S.; Lee, H. Heterogeneous atomic catalysts overcoming the limitations of single-atom catalysts. *ACS Nano* **2020**, *14*, 14355–14374.

[142] Zhang, R. F.; Jiang, B.; Fan, K. L.; Gao, L. Z.; Yan, X. Y. Designing nanozymes for *in vivo* applications. *Nat. Rev. Bioeng.* **2024**, *2*, 849–868.

[143] Zhang, H.; Zhang, L.; Cao, Z. B.; Cheong, S.; Boyer, C.; Wang, Z. G.; Yun, S. L. J.; Amal, R.; Gu, Z. Two-dimensional ultra-thin nanosheets with extraordinarily high drug loading and long blood circulation for cancer therapy. *Small* **2022**, *18*, 2200299.

[144] Bastianini, M.; Sisani, M.; Petracci, A.; Di Guida, I.; Faffa, C.; Cardellini, F. Caffeine vehiculation into alpha-zirconium phosphate: A multifunctional intercalation product and its application for modified topical release. *Mater. Adv.* **2021**, *2*, 1313–1319.

[145] Jin, L. G.; Hu, P.; Wang, Y. Y.; Wu, L. J.; Qin, K.; Cheng, H. X.;

Wang, S. H.; Pan, B. X.; Xin, H. B.; Zhang, W. H. et al. Fast-acting black-phosphorus-assisted depression therapy with low toxicity. *Adv. Mater.* **2020**, *32*, 1906050.

[146] Ji, X. Y.; Kong, N.; Wang, J. Q.; Li, W. L.; Xiao, Y. L.; Gan, S. T.; Zhang, Y.; Li, Y. J.; Song, X. R.; Xiong, Q. Q. et al. A novel top-down synthesis of ultrathin 2D boron nanosheets for multimodal imaging-guided cancer therapy. *Adv. Mater.* **2018**, *30*, 1803031.

[147] Yu, W. X.; Jin, D.; Zhang, Y. J.; Wang, S. H.; Yu, J. J.; Liu, M. M.; Dai, Y.; Yin, Y. C.; Cheng, J. J.; Liu, Y. Z. Provoking tumor disulfidptosis by single-atom nanozyme via regulating cellular energy supply and reducing power. *Nat. Commun.* **2025**, *16*, 4877.

[148] Wang, X. W.; Shi, Q. Q.; Zha, Z.; Zhu, D. D.; Zheng, L. R.; Shi, L. X.; Wei, X. W.; Lian, L.; Wu, K. L.; Cheng, L. Copper single-atom catalysts with photothermal performance and enhanced nanozyme activity for bacteria-infected wound therapy. *Bioact. Mater.* **2021**, *6*, 4389–4401.

[149] He, H.; Fei, Z. Y.; Guo, T. L.; Hou, Y.; Li, D.; Wang, K. F.; Ren, F. Z.; Fan, K. L.; Zhou, D. J.; Xie, C. M. et al. Bioadhesive injectable hydrogel with phenolic carbon quantum dot supported Pd single atom nanozymes as a localized immunomodulation niche for cancer catalytic immunotherapy. *Biomaterials* **2022**, *280*, 121272.

[150] Han, Y.; Ge, K.; Zhao, Y.; Bottini, M.; Fan, D. H.; Wu, W. C.; Li, L. W.; Liu, F. S.; Gao, S. T.; Liang, X. J. et al. Modulating the coordination environment of carbon-dot-supported Fe single-atom nanozymes for enhanced tumor therapy. *Small* **2024**, *20*, 2306656.

[151] Song, W. T.; Musetti, S. N.; Huang, L. Nanomaterials for cancer immunotherapy. *Biomaterials* **2017**, *148*, 16–30.

[152] Riley, R. S.; June, C. H.; Langer, R.; Mitchell, M. J. Delivery technologies for cancer immunotherapy. *Nat. Rev. Drug Discov.* **2019**, *18*, 175–196.

[153] Jin, P. W.; Wang, D. D.; Lu, Y. J.; Qian, Y.; Fang, C. Y.; Zhang, X. X.; Qian, J. C.; Qu, S. N.; Wang, H. Low-coordination configuration single-atom manganese nanozymes for NIR-imaging-oriented efficient catalytic oncotherapy. *Adv. Sci.* **2025**, *12*, 2502664.

[154] Cheng, L.; Wang, X. W.; Gong, F.; Liu, T.; Liu, Z. 2D nanomaterials for cancer theranostic applications. *Adv. Mater.* **2020**, *32*, 1902333.

[155] Sang, W.; Zhang, Z.; Dai, Y. L.; Chen, X. Y. Recent advances in nanomaterial-based synergistic combination cancer immunotherapy. *Chem. Soc. Rev.* **2019**, *48*, 3771–3810.

[156] Nam, J.; Son, S.; Park, K. S.; Zou, W. P.; Shea, L. D.; Moon, J. J. Cancer nanomedicine for combination cancer immunotherapy. *Nat. Rev. Mater.* **2019**, *4*, 398–414.

[157] Li, Z. Y.; Ding, B. B.; Li, J.; Chen, H.; Zhang, J. S.; Tan, J.; Ma, X. Y.; Han, D.; Ma, P. A.; Lin, J. Multi-enzyme mimetic MoCu dual-atom nanozyme triggering oxidative stress cascade amplification for high-efficiency synergistic cancer therapy. *Angew. Chem., Int. Ed.* **2025**, *64*, e202413661.

[158] Shao, F.; Jiang, R. T.; Li, L. H.; Lu, Y. X.; Chen, M. Y.; Li, J. H.; Liu, B.; Li, M. Near-infrared-II plasmonic multi-enzyme nanocapsules for hyperthermia-augmented cascade catalytic oncotherapy. *Adv. Funct. Mater.* **2025**, *35*, e11582.

[159] Fu, Q. R.; Wei, C.; Wang, M. Z. Transition-metal-based nanozymes: Synthesis, mechanisms of therapeutic action, and applications in cancer treatment. *ACS Nano* **2024**, *18*, 12049–12095.

[160] Liu, Y.; Niu, R.; Wang, Y. H.; Zhang, H. J.; Zhao, Y. L. Preparation and biomedical applications of single-metal atom catalysts. *Nat. Protoc.* **2026**, *21*, 775–807.

[161] Huo, M. F.; Wang, L. Y.; Wang, Y. W.; Chen, Y.; Shi, J. L. Nanocatalytic tumor therapy by single-atom catalysts. *ACS Nano* **2019**, *13*, 2643–2653.

[162] Zhang, M. Y.; Zhu, W.; Liu, Z. Y.; Chen, S. R.; Zhou, D. Y.; Mu, X. Q.; Zhuang, Z. C.; Wang, S. C.; Yang, J. R.; Du, Y. P. et al. Selective sieving effect of multi-atomic bismuth interfaces for efficient formate electrosynthesis and evolution at industrial current density. *Angew. Chem., Int. Ed.* **2025**, *64*, e202510206.

[163] Nan, F. C.; Wei, Q. L.; Kou, T. T.; Zhao, Y. X.; Shen, L. B.; Li, D. W.; Chang, T.; Wang, L. Y.; Lang, F. F.; Yu, W. W. Accurate regulation of carbon skeletons bonded to Fe–N_4 single atom nanozymes for efficient generation of reactive oxygen species. *Sci. China Chem.* **2025**, *68*, 1067–1077.

[164] Wang, X. Y.; Pan, Y. Z.; Yang, J. R.; Li, W. H.; Gan, T.; Pan, Y. M.; Tang, H. T.; Wang, D. S. Single-atom iron catalyst as an advanced redox mediator for anodic oxidation of organic electrosynthesis. *Angew. Chem., Int. Ed.* **2024**, *63*, e202404295.

[165] Li, T. S.; Chen, L.; Fu, X.; Liu, Z. H.; Zhu, S. L.; Chen, Y. Q.; Zhang, J. Iron single-atom nanocatalysts in response to tumor microenvironment for highly efficient Chemo-chemodynamic therapy. *J. Ind. Eng. Chem.* **2022**, *112*, 210–217.

[166] Su, Y. T.; Wu, F.; Song, Q. X.; Wu, M. J.; Mohammadniaei, M.; Zhang, T. W.; Liu, B. L.; Wu, S. S.; Zhang, M.; Li, A. et al. Dual enzyme-mimic nanozyme based on single-atom construction strategy for photothermal-augmented nanocatalytic therapy in the second near-infrared biowindow. *Biomaterials* **2022**, *281*, 121325.

[167] Zhao, R. X.; Zhu, Y. L.; Feng, L. L.; Liu, B.; Hu, Y. Y.; Zhu, H. X.; Zhao, Z. Y.; Ding, H.; Gai, S. L.; Yang, P. P. Architecture of vanadium-based MXene dysregulating tumor redox homeostasis for amplified nanozyme catalytic/photothermal therapy. *Adv. Mater.* **2024**, *36*, 2307115.

[168] Guan, S. Y.; Liu, Y. Y.; Liu, S. L.; Zhuang, Z. C.; Shen, R. F.; Zhang, H. H.; Liang, E. J.; Fan, Y. P.; Jiang, J. C.; Liu, B. Z. et al. MXene-supported Ru–Ni: A common active site for hydrolysis, hydrogen oxidation, and hydrogenation. *Angew. Chem., Int. Ed.* **2025**, *64*, e202506869.

[169] Lin, Y. F.; Zhou, C.; Lu, Y. J.; Yang, Y.; Bi, C. Y.; Lai, X.; Wang, D. D.; Qian, J. C.; Qu, S. N.; Wang, H. Enhanced catalytic therapy by modulating substrate adsorption and local electron density through coordinatively unsaturated Cu–N_2 single-atom sites on carbon dots. *Adv. Funct. Mater.* **2026**, *36*, e75092.

[170] He, J. H.; Du, M. X.; Makvandi, P.; Xu, Y.; He, X. J.; Jin, X. R. NIR-II-enhanced Pt–MoS_2 nanozymes for synergistic photothermal and chemodynamic therapy against methicillin-resistant *Staphylococcus aureus* to promote wound healing. *Nano Res.* **2025**, *18*, 94907538.

[171] Wang, L. J.; Zheng, S. J.; Lin, X. X.; Chen, Y. X.; Li, J. R.; Liu, X. Y.; Wang, F.; Li, C. L. A RuNPs-based multifunctional nanoplatform with excellent dual enzyme-mimic activities for diabetes diagnosis, cancer cell elimination, and *in vitro* antibacterial. *Talanta* **2025**, *283*, 127121.

[172] Li, Z.; Fan, X. W.; Liu, Y.; Yue, M. X.; Wu, T. T.; Wang, X.; Jiang, W.; Fan, K. Engineering mild-photothermal responsive and NO donor prussian blue nanozymes using mild synthesis for inflammation regulation and bacterial eradication in periodontal disease. *Adv. Mater.* **2025**, *37*, 2409840.

[173] Gao, F.; Shao, T. Y.; Yu, Y. P.; Xiong, Y. J.; Yang, L. H. Surface-bound reactive oxygen species generating nanozymes for selective antibacterial action. *Nat. Commun.* **2021**, *12*, 745.

[174] Liu, Y. H.; Xu, B. L.; Lu, M. Z.; Li, S. S.; Guo, J.; Chen, F. Z.; Xiong, X. L.; Yin, Z.; Liu, H. Y.; Zhou, D. S. Ultrasmall Fe-doped carbon dots nanozymes for photoenhanced antibacterial therapy and wound healing. *Bioact. Mater.* **2022**, *12*, 246–256.

[175] Huang, L. J.; Pu, H. B.; Sun, D. W. Spatiotemporally guided single-atom bionanozyme for targeted antibiofilm treatment. *Small* **2024**, *20*, 2407747.

[176] Jiang, Y. X.; Rong, H. T.; Wang, Y. F.; Liu, S. G.; Xu, P.; Luo, Z.; Guo, L. M.; Zhu, T.; Rong, H. P.; Wang, D. S. et al. Single-atom cobalt nanozymes promote spinal cord injury recovery by anti-oxidation and neuroprotection. *Nano Res.* **2023**, *16*, 9752–9759.

[177] Wang, X.; Qin, X. D.; Liu, Y.; Fang, Y. T.; Meng, H.; Shen, M. L.; Liu, L. L.; Huan, W. W.; Tian, J.; Yang, Y. W. Plasmonic supramolecular nanozyme-based bio-cockleburs for synergistic therapy of infected diabetic wounds. *Adv. Mater.* **2024**, *36*, 2411194.

[178] Feng, Y. C.; Shi, Y. X.; Zhao, Q.; Gao, G. Y.; Wang, Z. Q.; Zhi, J. F. Onion-like carbon based single-atom iron nanozyme for

photothermal and catalytic synergistic antibacterial application. *J. Colloid Interface Sci.* **2025**, *681*, 205–214.
[179] Han, J. Y.; Guan, J. Q. Applications of single-site iron nanozymes in biomedicine. *Coord. Chem. Rev.* **2023**, *490*, 215209.
[180] Ou, H. H.; Qian, Y. P.; Yuan, L. T.; Li, H.; Zhang, L. D.; Chen, S. H.; Zhou, M.; Yang, G. D.; Wang, D. S.; Wang, Y. G. Spatial position regulation of Cu single atom site realizes efficient nanozyme photocatalytic bactericidal activity. *Adv. Mater.* **2023**, *35*, 2305077.
[181] Xie, Z. J.; Wang, D.; Fan, T. J.; Xing, C. Y.; Li, Z. J.; Tao, W.; Liu, L. P.; Bao, S. Y.; Fan, D. Y.; Zhang, H. Black phosphorus analogue tin sulfide nanosheets: Synthesis and application as near-infrared photothermal agents and drug delivery platforms for cancer therapy. *J. Mater. Chem. B* **2018**, *6*, 4747–4755.
[182] Xie, Z. J.; Xing, C. Y.; Huang, W. C.; Fan, T. J.; Li, Z. J.; Zhao, J. L.; Xiang, Y. J.; Guo, Z. N.; Li, J. Q.; Yang, Z. G. et al. Ultrathin 2D nonlayered tellurium nanosheets: Facile liquid-phase exfoliation, characterization, and photoresponse with high performance and enhanced stability. *Adv. Funct. Mater.* **2018**, *28*, 1705833.
[183] Luo, M. M.; Fan, T. J.; Zhou, Y.; Zhang, H.; Mei, L. 2D black phosphorus-based biomedical applications. *Adv. Funct. Mater.* **2019**, *29*, 1808306.
[184] Qiu, M.; Ren, W. X.; Jeong, T.; Won, M.; Park, G. Y.; Sang, D. K.; Liu, L. P.; Zhang, H.; Kim, J. S. Omnipotent phosphorene: A next-generation, two-dimensional nanoplatform for multidisciplinary biomedical applications. *Chem. Soc. Rev.* **2018**, *47*, 5588–5601.
[185] Murali, A.; Lokhande, G.; Deo, K. A.; Brokesh, A.; Gaharwar, A. K. Emerging 2D nanomaterials for biomedical applications. *Mater. Today* **2021**, *50*, 276–302.
[186] Ye, J.; Hu, M. H.; Chen, Q. Q.; Huang, P. C.; Wu, F. Y.; Mao, J. J. Microwave-assisted rapid synthesis of near-infrared light-responsive Pd single-atom nanozymes for colorimetric detection of acetylcholinesterase activity. *Anal. Chem.* **2025**, *97*, 12455–12464.
[187] Shen, L. H.; Khan, M. A.; Wu, X. Y.; Cai, J.; Lu, T.; Ning, T.; Liu, Z. M.; Lu, W. C.; Ye, D. X.; Zhao, H. B. et al. Fe–N–C single-atom nanozymes based sensor array for dual signal selective determination of antioxidants. *Biosens. Bioelectron.* **2022**, *205*, 114097.
[188] Xia, J. N.; Fu, R. X.; Li, Z.; Ding, Y. P.; Zhao, H. B.; Ye, D. X. Graphyne-supported manganese single-atom nanozyme sensor array for bisphenol identification. *Talanta* **2025**, *285*, 127326.
[189] Li, J.; Wu, C.; Yuan, C. S.; Shi, Z. Z.; Zhang, K. Y.; Zou, Z.; Xiong, L. L.; Chen, J.; Jiang, Y. L.; Sun, W. et al. Single-atom iron anchored on 2-D graphene carbon to realize bridge-adsorption of O–O as biomimetic enzyme for remarkably sensitive electrochemical detection of H_2O_2. *Anal. Chem.* **2022**, *94*, 14109–14117.
[190] Liu, M.; Xu, W.; Tang, Y.; Wu, Y.; Gu, W.; Du, D.; Lin, Y.; Zhu, C. Tuning atomically dispersed metal sites in nanozymes for sensing applications. *Angew. Chem., Int. Ed.* **2025**, *64*, e202424070.
[191] Xia, J. K.; Xu, J. W.; Yu, B.; Liang, X.; Qiu, Z.; Li, H.; Feng, H. J.; Li, Y. F.; Cai, Y. J.; Wei, H. Y.; Li, H. T.; Xiang, H.; Zhuang, Z. C.; Wang, D. S. A metal-sulfur-carbon catalyst mimicking the two-component architecture of nitrogenase. *Angew. Chem., Int. Ed.* **2024**, *63*, e202412740.
[192] Sun, J. H.; Yan, M. J.; Tao, G. D.; Su, R. B.; Xiao, X. M.; Wu, Q. S.; Chen, F.; Wu, X. L.; Lin, H. J. A single-atom manganese nanozyme mediated membrane reactor for water decontamination. *Water Res.* **2025**, *268*, 122627.
[193] Zhong, K. Q.; Yu, F. Y.; Zhang, D.; Li, Z. H.; Xie, D. H.; Li, T. T.; Zhang, Y.; Yuan, L.; Li, H.; Wu, Z. Y. et al. Data-driven accelerated discovery coupled with precise synthesis of single-atom catalysts for robust and efficient water purification. *Angew. Chem., Int. Ed.* **2025**, *64*, e202500004.
[194] Xu, L.; Wu, C. X.; Chai, C.; Cao, S. Y.; Bai, X.; Ma, K. Y.; Jin, X.; Shi, X.; Jin, P. K. Adsorption of micropollutants from wastewater using iron and nitrogen co-doped biochar: Performance, kinetics and mechanism studies. *J. Hazard. Mater.* **2022**, *424*, 127606.
[195] Lu, J. N.; Qi, W. H.; Gu, S. N.; Wang, Y. N.; Yu, J. G.; Zhou, G. W. Dual metal-bridged 2D COF for high performance of H_2O_2 photosynthesis across wide pH range activated by dual route linkage. *Angew. Chem., Int. Ed.* **2026**, *65*, e9931408.
[196] Wang, Y.; Ma, F. Y.; Zhang, G. Q.; Zhang, J. W.; Zhao, H.; Dong, Y. M.; Wang, D. S. Precise synthesis of dual atom sites for electrocatalysis. *Nano Res.* **2024**, *17*, 9397–9427.

This is an open access article under the terms of the Creative Commons Attribution 4.0 International License (CC BY 4.0, https://creativecommons.org/licenses/by/4.0/).

© The Author(s) 2026. Published by Tsinghua University Press.